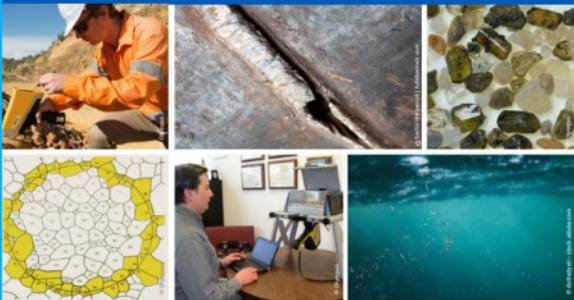




2nd Advanced Optical Metrology Compendium

Advanced Optical Metrology

Geoscience | Corrosion | Particles | Additive Manufacturing: Metallurgy, Cut Analysis & Porosity



EVIDENT
OLYMPUS

WILEY

The latest eBook from **Advanced Optical Metrology**.
Download for free.

This compendium includes a collection of optical metrology papers, a repository of teaching materials, and instructions on how to publish scientific achievements.

With the aim of improving communication between fundamental research and industrial applications in the field of optical metrology we have collected and organized existing information and made it more accessible and useful for researchers and practitioners.

EVIDENT
OLYMPUS

WILEY

2D Metal–Organic Frameworks as Competent Electrocatalysts for Water Splitting

Chao-Peng Wang, Yu-Xuan Lin, Lei Cui, Jian Zhu,* and Xian-He Bu*

Hydrogen, a clean and flexible energy carrier, can be efficiently produced by electrocatalytic water splitting. To accelerate the sluggish hydrogen evolution reaction and oxygen evolution reaction kinetics in the splitting process, highly active electrocatalysts are essential for lowering the energy barriers, thereby improving the efficiency of overall water splitting. Combining the distinctive advantages of metal–organic frameworks (MOFs) with the physicochemical properties of 2D materials such as large surface area, tunable structure, accessible active sites, and enhanced conductivity, 2D MOFs have attracted intensive attention in the field of electrocatalysis. Different strategies, such as improving the conductivities of MOFs, reducing the thicknesses of MOF nanosheets, and integrating MOFs with conductive particles or substrates, are developed to promote the catalytic performances of pristine MOFs. This review summarizes the recent advances of pristine 2D MOF-based electrocatalysts for water electrolysis. In particular, their intrinsic electrocatalytic properties are detailedly analyzed to reveal important roles of inherent MOF active centers, or other in situ generated active phases from MOFs responsible for the catalytic reactions. Finally, the challenges and development prospects of pristine 2D MOFs for the future applications in overall water splitting are discussed.

water splitting ($2\text{H}_2\text{O} \rightarrow 2\text{H}_2 + \text{O}_2$) comprises two half-reactions: hydrogen evolution reaction (HER) and oxygen evolution reaction (OER). Theoretically, the decomposition voltage of water splitting is 1.23 V.^[4] Nevertheless, the actual voltage is greater than the theoretical voltage of water dissociation due to the large activation energy.^[5] To accelerate the sluggish HER and OER kinetics, efficient electrocatalysts are required to reduce kinetic energy barriers. Currently, the most efficient electrocatalysts toward water splitting are precious metal-based catalysts such as Pt/C for HER and RuO₂ or IrO₂ for OER.^[6] Unfortunately, the large-scale application is hindered by the high price and scarcity of noble metals. Therefore, it is urgent to seek highly active and inexpensive electrocatalysts.

Metal–organic frameworks (MOFs) are an emerging class of porous crystalline materials constructed by metal ions or clusters and organic ligands.^[7–9] Due to their unique merits of large porosities,

1. Introduction


The continuous rise of energy demand and the rapid depletion of fossil fuels calls for the search of renewable energy resources to meet the growing needs.^[1,2] Among the various energy alternatives, hydrogen has been considered as a promising renewable fuel owing to its high gravimetric energy density and clean combustion product.^[3] Driven by the abundance and availability of water resources on the earth, it is sustainable to produce hydrogen by water electrolysis. Electrochemical

diversified structures, and designable compositions, MOFs have gained extensive attention in various applications, such as chemical sensors,^[10] gas absorption,^[11] and energy conversion/storage.^[12–16] From an electrochemical perspective, MOFs can be perceived as a spatial architecture, where discrete functional units can be designed to lie in close proximity to facilitate bond breaking/forming reactions.^[17] Generally, active sites and conductivity are considered as the key factors affecting the electrochemical performance of HER and OER catalysts. Despite abundant intrinsic molecular metal sites, large size and poor conductivity (10^{-10} S cm⁻¹) of bulk MOFs restrict the full use of their distinct advantages and lead to poor electrochemical performance.^[18] To improve electrocatalytic activity of MOFs, they can be used as sacrificial precursors or templates to fabricate various conductive carbides,^[19] oxides/hydroxides,^[20] phosphides,^[21] chalcogenides,^[22] single-atom catalysts^[23] or pure carbon materials with rich morphologies and sizes.^[24,25] However, the high temperatures calcination inevitably leads to the loss of intrinsic active sites and long-range orders in MOFs. Therefore, improving the catalytic properties of pristine MOFs for highly efficient electrocatalysts is quite appealing.

Compared with bulk MOFs, 2D MOFs emerge as a category of promising electrocatalysts toward HER or OER due to their unique characteristics, including enlarged surface areas, rapid mass transport, and enhanced conductivities (Figure 1).^[26,27]

C.-P. Wang, Y.-X. Lin, L. Cui, J. Zhu, X.-H. Bu
School of Materials Science and Engineering
National Institute for Advanced Materials
Nankai University
Tianjin 300350, P. R. China
E-mail: zj@nankai.edu.cn; buxh@nankai.edu.cn

J. Zhu, X.-H. Bu
Smart Sensing Interdisciplinary Science Center
Tianjin Key Laboratory of Metal and Molecule-Based Material Chemistry
Nankai University
Tianjin 300350, P. R. China

 The ORCID identification number(s) for the author(s) of this article can be found under <https://doi.org/10.1002/smll.202207342>.

DOI: 10.1002/smll.202207342

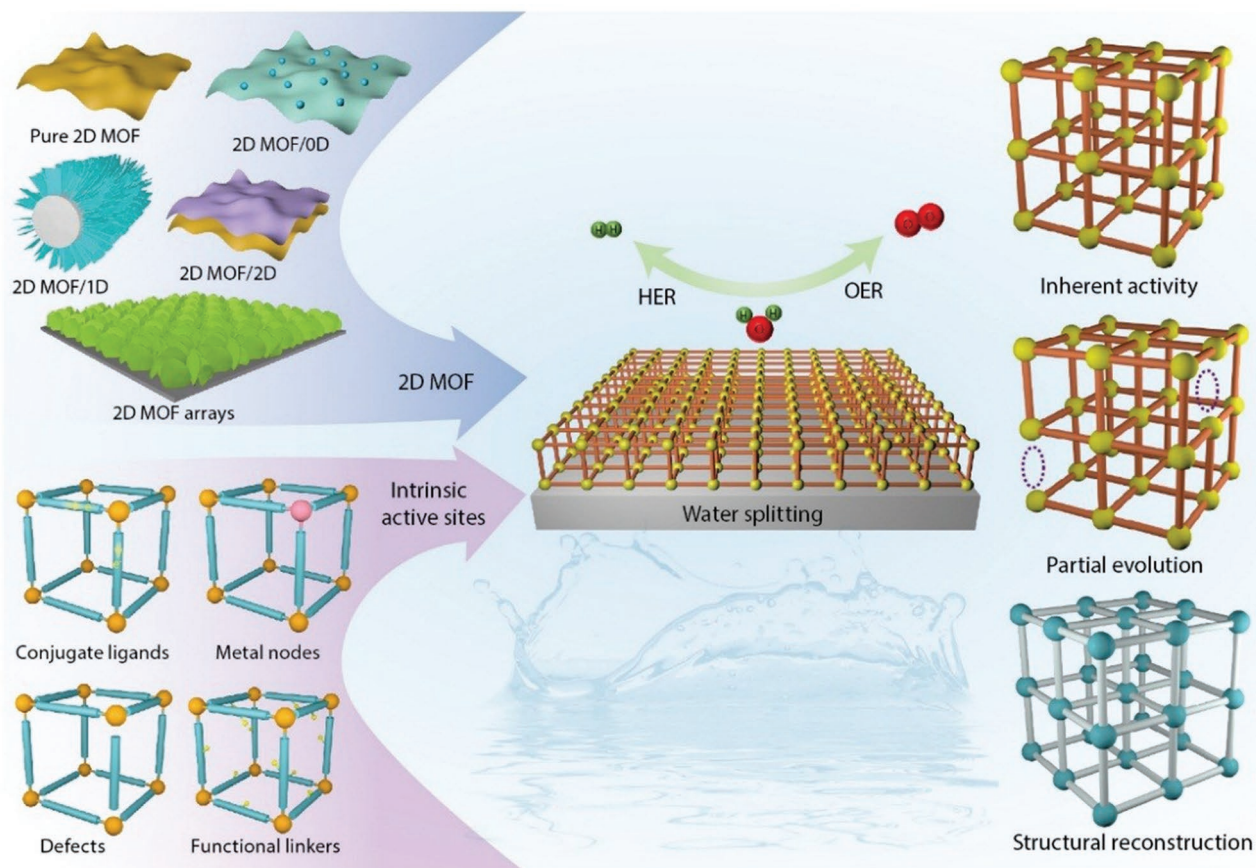


Figure 1. Modulation strategies and intrinsic active sites of pristine 2D MOF-based catalysts for electrochemical water splitting.

2D MOFs constructed from single or a few layers of atoms, allowing the formation of lamellar materials with 2D morphologies and high lateral to thickness aspect ratios. Since the electrocatalytic process occurs on the surface/interface,^[28] the presence of defects or coordinatively unsaturated sites on the 2D MOFs can promote catalytic activity. Moreover, the distinct periodicity in the surface structures provide an ideal platform to explore the precise structure–performance relationships for rational catalyst design at the atomic level.^[29] To enhance the electrocatalytic activity of the original 2D MOFs, various strategies have been proposed: 1) improving conductivities of 2D MOFs by enabling orbital overlap from building blocks for efficient electron/hole charge hopping;^[30] 2) reducing the thicknesses of 2D MOF nanosheets for easily accessible electrochemically active sites;^[31] 3) compositing 2D MOFs with other nanomaterials for synergistic enhancements of activity;^[32] 4) growing 2D MOF arrays on conductive substrates for better electron and ion transfer.^[33]

The 2D MOFs for electrochemical water splitting are currently at a stage of rapid development. **Figure 2** displays the timeline and main progress of pristine 2D MOF-based electrocatalysts in water electrolysis. In 2014, 2D conductive cobalt dithiolene MOFs were used as efficient HER electrocatalysts, showing remarkable stability in an acidic solution.^[34] Subsequently, different 2D conductive MOFs based on specific π -conjugated or redox-active organic ligands have been

proposed, such as single-layer 2D conductive nickel dithiolene MOF nanosheets (0.7–0.9 nm).^[35] Recently, enormous efforts have been devoted to the design and preparation of intrinsically insulating yet electrochemically active 2D MOF nanosheets by reducing the thicknesses to one or several monolayers. Encouragingly, ultrathin NiCo bimetal–organic framework nanosheets (3.1 nm) were first fabricated by Tang’s group, and displayed remarkable intrinsic OER performance.^[36] After that, various strategies, such as regulating metal ions and ligands of MOF nanosheets, or integrating MOFs with conductive particles or substrates, have been explored to optimize the catalytic performances of pristine MOFs. For example, Prussian blue analogues nanosheet (5 nm) arrays were employed as outstanding self-supporting bifunctional electrocatalyst.^[37] Very recently, Su and co-workers proposed a single-atom strategy to fabricate NiRu_{0.13}-BDC nanosheet arrays with remarkable HER activities by introducing atomically dispersed Ru.^[38] Recent progress also investigates the structural stability of 2D MOFs under the specific conditions of HER and OER, as well as illustrates the distinct mechanism in the catalytic process of 2D MOFs. Although a number of reviews related to water-splitting applications of MOF-based materials have been published,^[39–43] few of them give a full analysis on the approaches toward active sites engineering, as well as the corresponding intrinsic catalytic performance of 2D MOFs. Therefore, a comprehensive review concerning the design strategies for high-performance 2D

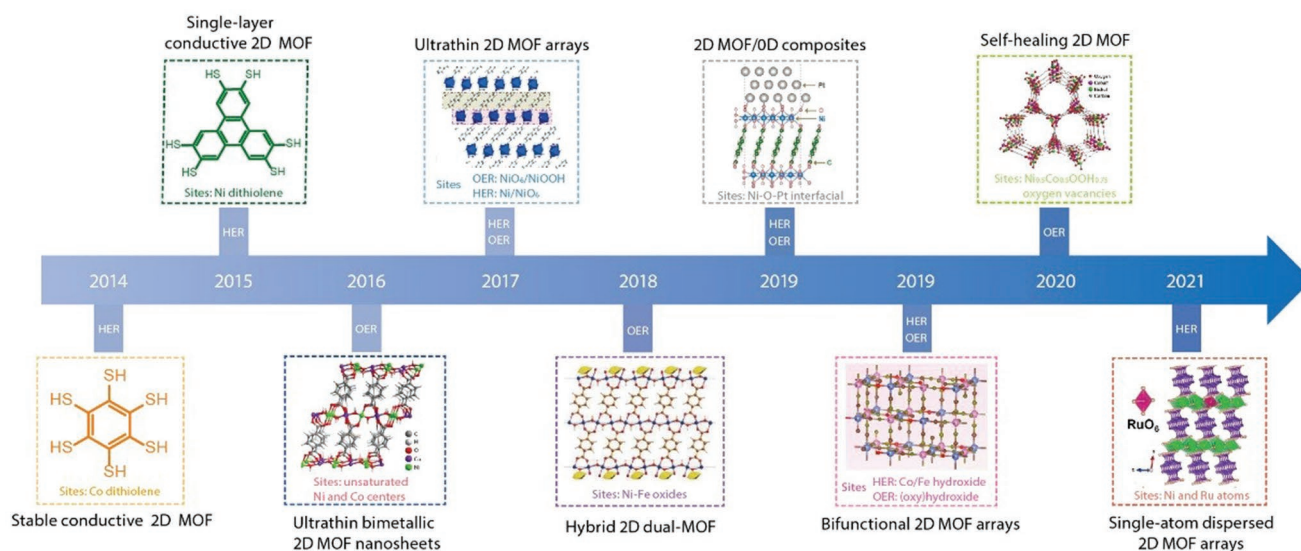


Figure 2. Timelines and main progress of the pristine 2D MOF-based electrocatalysts for water electrolysis.

MOFs electrocatalysts, specially concentrating on their intrinsic activity toward water dissociation, is highly demanded.

In this review, we summarize and analyze the recently reported 2D MOF-based electrocatalysts with high activities for water electrolysis. The introduction of overall water splitting mechanism and electrochemical stability of MOFs will be introduced in the first part. Then, different synthetic strategies of directly utilizing 2D MOFs as HER and OER electrocatalysts are included. Particularly, the intrinsic electrocatalysis properties are detailedly presented to illustrate the roles of active sites in the catalytic reactions. Finally, we conclude the current states and provide development prospects of pristine 2D MOFs for the future applications in overall water splitting.

2. General Mechanism of Water Electrolysis

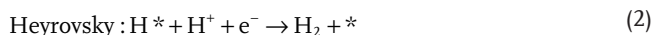
Electrochemical water splitting comprises cathodic HER and anodic OER two half reactions, which can be carried out in acidic or alkaline electrolyte (Figure 3a). The water electrolysis process is a thermodynamically uphill reaction, which requires about 237.2 kJ mol⁻¹ thermodynamics Gibbs free energy corresponding to an equilibrium cell voltage of 1.23 V at 25 °C.^[40,44] Nevertheless, the pH of electrolyte could affect the equilibrium voltage of cathode and anode. In acidic solution (pH = 0), the cathode potential for HER (2H⁺ + 2e⁻ → H₂) can be 0 V, while the anode potential for OER (H₂O → 1/2O₂ + 2H⁺ + 2e⁻) can be 1.23 V.^[45] According to Nernst equation, ≈59 mV of reaction potential can be shifted for each pH unit.^[46] In alkaline solution (pH = 14), the cathode potential for HER (2H₂O + 2e⁻ → H₂ + 2OH⁻) can be -0.83 V, while the anode potential for OER (2OH⁻ → 1/2O₂ + H₂O + 2e⁻) can be 0.40 V. In practice, the water-splitting electrolyzers require an input voltage in excess of 1.23 V due to the high overpotential of HER and OER. The overpotential is generally considered a kinetic phenomenon and splits into various contributions such as ohmic voltage loss or mass-transport limitations during the flow of charge. In the

context of electrocatalysis, overpotential relates to a kinetic hindrance of individual elementary reaction steps because of the activation barriers.

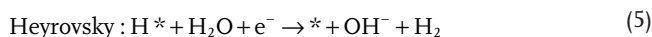
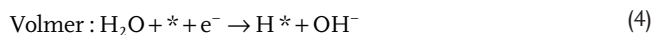
2.1. Hydrogen Evolution Reaction

Whether in acidic or alkaline electrolyte, it is generally believed that HER is a two-electron transfer process involving multiple steps. The mechanisms of HER reaction are listed as follows (Equations (1)–(6)), and * and H* represent catalytic sites and the adsorbed hydrogen on the catalyst surface.^[47,48]

In an acidic medium



In an alkaline or neutral medium



Considering the aforementioned elementary steps, there are two different reaction processes leading to HER, namely, the Volmer–Heyrovsky or Volmer–Tafel mechanisms. In both cases, a proton or water molecule is first adsorbed on catalytic sites to generate the intermediates of adsorbed hydrogen atoms. Subsequently, in alkaline or neutral electrolyte, H* would incline to couple with a water molecule and an electron to produce H₂ via Heyrovsky steps in the case of low coverage of H* on the electrocatalyst surface. When the H* coverage is high,

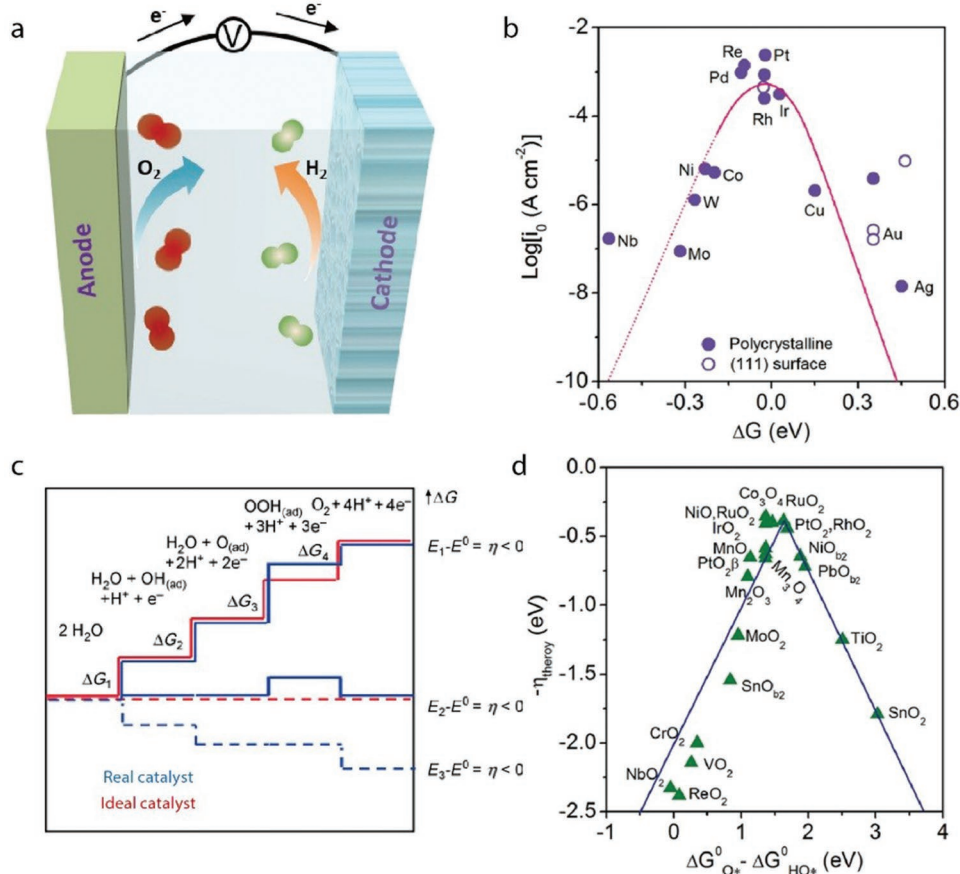


Figure 3. a) Schematic illustration of a water-splitting electrolyzer. b) HER volcano plot between exchange current density and hydrogen adsorption free energy at $U = 0$ V for various metals. The open circles and filled circles represent experimental (111) single-crystal and polycrystalline surfaces data, respectively. Reproduced with permission.^[53] Copyright 2019, Wiley-VCH. c) Plot of Gibbs free energy of reactive species and intermediates (horizontal lines) of OER versus the reaction coordinate for ideal (red lines) and actual (blue lines) catalysts. Dashed lines indicate the energetics at the electrode potential where all the thermochemical barriers disappear. Reproduced with permission.^[60] Copyright 2010, Wiley-VCH. d) The volcano plot for OER of theoretical overpotential against the standard free energy of $\Delta G_{\text{O}^*} - \Delta G_{\text{HO}^*}$. Reproduced with permission.^[61] Copyright 2011, Wiley-VCH.

two adjacent H^* atoms would bind to form H_2 through Tafel routes. Analogously, under acidic condition, HER reactions undergo the similar pathways. HER activities for most catalysts in nonacidic medium are two orders of magnitude lower than in acid solutions due to the sluggish Volmer step.^[49] According to the Sabatier principle, the optimal catalytic activity can be achieved on a catalyst surface with the appropriate binding strength for reactive intermediates.^[50] With respect to the elementary steps of HER, H^* appears to be the only reaction intermediate, whose adsorption strength has long been established as the controlling factor.^[51] The hydrogen adsorption free energy (ΔG_{H^*}) is used to quantitatively describe the interaction strength of H^* intermediates with the catalysts surface.^[52] Too weak ΔG_{H^*} would lead to a slow Volmer step (adsorption process) and restrict the whole reaction rates. Conversely, too strong ΔG_{H^*} makes Volmer step easy, while limits the subsequent Tafel or Heyrovsky steps (desorption process). Thus, regulating the value of ΔG_{H^*} for controlling the reaction rates of HER is essential. As shown in Figure 3b, the ΔG_{H^*} values and the experimentally obtained exchange current densities have a volcano relationship for some representative metal catalysts.^[53]

To achieve an ideal catalytic performance, the optimal ΔG_{H^*} should be close to zero.^[54]

2.2. Oxygen Evolution Reaction

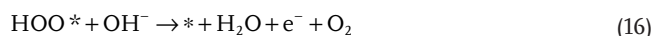
Compared with HER mechanisms, OER is more kinetically sluggish. OER involves the difficult O–H bond cleavage and O–O bond formation steps, which are associated with complex multistep four-electron transfer processes, and these steps greatly hinder the efficiency of water electrolysis.^[55] The well-accepted mechanisms of OER could be varied depending on the pH of solutions, as displayed in Equations (7)–(16), where * stands for the catalytic site on the electrocatalyst surface.^[56,57]

In an acidic solution





In an alkaline solution



In an acidic or alkaline solution, an adsorbed water molecule or hydroxyl ion is gradually transformed into the intermediates of HO*, O*, and HOO* via proton-coupled electron-transfer steps.^[58] It is noted that O* intermediates may experience two different pathways to generate oxygen.^[59] One route is through the direct combination of two O* to form oxygen, and the other one involves the formation of HOO* species which subsequently transition into oxygen. Regardless of which route, the overall OER involves the adsorption interactions between the surfaces of electrocatalysts and the intermediates of HO*, O*, and HOO*. An ideal OER catalyst requires all the four elemental steps with the reaction free energies of the same magnitude (Figure 3c), but this ideal situation is almost impossible to achieve because of the linearly correlated adsorption energies of these oxygen-containing intermediates.^[60] The corresponding rate-determining step is known as the reaction pathway with the highest free energy, which determines the catalytic performance. To further precisely reflect the nature of the reaction mechanism, a new descriptor of $\Delta G_{\text{O}^*}^0 - \Delta G_{\text{HO}^*}^0$ was proposed by Rossmeis and co-workers.^[61] The relationship between theoretical overpotential and $\Delta G_{\text{O}^*}^0 - \Delta G_{\text{HO}^*}^0$ was calculated and plotted in Figure 3d, indicating the OER activity of catalysts also comply with the Sabatier principle. The adsorption strength of the reaction intermediates to the catalytic sites must not be too strong (the left side of the volcano) or too weak (the right side of the volcano) to guarantee a delicate balance between the adsorption and desorption processes. The binding energy for various intermediates is highly correlated with the electronic and geometric structure of catalysts surface, which can guide us to effectively seek and predict effective MOF-based OER catalysts.

3. Factors Affecting the Performance of MOFs for Water Electrolysis

The performance of water electrolysis is related to many factors, such as catalyst morphology, surface structure, and interface effect. These factors affect the number of active sites, coordination environment, and electronic structure of MOF electrocatalysts.

MOFs can be classified into 0D (e.g., nanoparticles), 1D (e.g., nanowires), 2D (e.g., nanoflakes), and 3D (e.g., nanocubes) according to their specific geometrical dimensions.^[39] Although 0D nanostructures provide large surface areas for water splitting, they suffer from poor conductivities due to the shortened depletion width and numerous grain boundaries where holes and electrons get recombined easily.^[62] In general, 1D, 2D or 3D nanocatalysts display better catalytic performance than 0D nanostructures. 1D nanomaterials are usually featured with homogeneous structural formation and unidirectional flow of electrons.^[63] For example, the OER activities of 1D CoNi-ZIF nanofibers were superior to the annealed samples, which tend to destroy the 1D morphology during thermal annealing processes.^[64] 2D catalysts possess large surface-to-volume ratio, hierarchical porosity, and high exposure of active sites, which are conducive to enhancing catalytic performance.^[39] ZIF-67-derived 2D nanosheets displayed high electrochemical active areas and open channels to release bubble during HER/OER processes.^[65] Despite decreased surface areas, 3D nanostructures can effectively hinder aggregation and offer superior pathways for electron transfer.^[66]

Since water electrolysis occurs on the surface of catalysts, the surface state would significantly affect the interaction between catalyst and reactants/intermediates, which then determines the catalytic performance. Therefore, the appropriate surface regulation is pivotal for the design of electrocatalysts. Generally, materials with smooth surfaces exhibit poor catalytic activity as compared to rough surfaces due to the exposure of limited active centers as well as the weak electronic effect.^[67] For instance, Yamauchi and co-workers constructed 2D mesoporous nanosheets with a high surface area and thermal stability, displaying excellent OER performance.^[68] Other than creating a porous surface, enhancing the length/diameter ratio of 1D nanostructures and lowering the thickness of 2D nanostructures are also effective strategies for the improvement of electrochemical activity. In addition, rationally adjusting the surface valence states of metal center is another effective method to regulate the electrocatalytic performance. For example, Wang's group demonstrated that various metal valences in MOFs play a significant role in tuning their intrinsic electronic configuration.^[69] The low valence (Fe²⁺) state of Fe-MOF-74 exhibited better OER activity due to the improved conductivity and adsorption ability.

Apart from the structural design and surface regulation, interface engineering also has been an advanced strategy to promote the intrinsic catalytic activity and stability of electrocatalysts.^[70] Compared to single phase counterpart, heterostructures with high-quality interfaces possess higher activity due to the unique interaction effect between two various components. The superior electrochemical performance for overall water splitting can be achieved by fabricating a heterostructure with one part active for HER and the other for OER. For instance, Li and co-workers reported that NiFe-metal sulfide (MS)/MOF could act as a highly efficient bifunctional electrocatalyst for overall water splitting.^[71] The significant improvement in catalytic performance was ascribed to the strong electronic interaction, which could effectively boost electron transfer and optimize the adsorption energy of reaction intermediates.

4. Characteristics of MOFs

MOFs are a class of porous materials formed by interconnected single-metal nodes (e.g., Zn²⁺ in ZIF-8) or polynuclear clusters (known commonly as secondary building units (SBUs), e.g., Zr₆O₄(OH)₄ in UiO-66) with organic ligands.^[72] Compared to single-metal nodes, the SBUs are thermodynamically stabilized via strong bonds, and further impart architectural and mechanical stability. By judiciously assembling suitable metal nodes and various linkers, MOFs with uniformly distributed active centers can be tailor-made as matrixes with controlled pore sizes, morphologies and functionalities. For example, Yaghi and co-workers illustrated that the pore size of MOFs could be readily regulated by using elongated organic ligands.^[73] This allowed the synthesis of various isorecticular MOFs, in which the functionalities could be tuned and the pore size could be varied.

The network connectivity of building blocks largely determines the topologies and properties of MOFs.^[74] For instance, a Co²⁺ ion can have either four (tetrahedral) or six (octahedral) coordination number and geometry, which may rely on the bulkiness of the binding linkers.^[75] Furthermore, the coordination geometry of building blocks is an important parameters in controlling the dimensionality of MOFs.^[76] For 1D structures, the bonding between the building blocks is spread over the structure along one direction, thereby leading to the chain structures. For 2D structures, the building blocks are bonded along horizontal and vertical directions, which result in a layered structure. These layers can stack each other via weak interactions, consequently generating a multilayer structure. The 3D structure can be obtained by engaging the building blocks that bond in all directions.

Compared with traditional bulk MOFs, 2D MOFs exhibit considerable merits for overall water splitting due to the specific features. First, the increased surface area and the rich accessible unsaturated metal sites can promote the interaction with the reactive substrates.^[77] Second, the nanometer thickness enables to shorten diffusion distance and facilitates mass transfer during electrocatalytic process, thus increasing the reaction rates.^[78] Third, bulk MOFs generally suffer from poor conductivity, which severely hinders their potential application in electrochemical areas. In comparison, 2D MOF allows for the formation of vacancies, which act as shallow donors to increase the carrier concentration in 2D MOF, resulting in enhanced charge transfer.^[79] Lastly, some defects may be achieved during the preparation of 2D MOFs, which are conducive to enhancing the intrinsic catalytic performance.

5. Electrochemical Stability and Active Centers of 2D MOFs

The variety of organic linkers and metallic building blocks in MOFs offers tailorable spaces for the design of proper electrocatalysts. Before we dive into the discussion of electrochemical properties of MOFs, we will first deliberate the chemical stability of MOFs, which is a fundamental parameter to reveal the intrinsic catalytic sites of MOFs with respect to the electrochemical reactions. Here, the chemical stability of MOFs has

been defined as the resistance of MOF structure to the degradation upon exposures to the operating environment.^[80]

The metal–ligand coordination bond strength affects the chemical stability of MOFs under various test conditions. In acids, the degradation of MOFs is mainly caused by the competition of protons and metal ions for the ligands. In bases, the chemical attack of hydroxide ions on the ligands leads to the decomposition of MOFs. Thus, the direct means to improve MOF stability is to enhance the robustness of coordination bonds. Since it is not always easy to quantify the bond strength, the chemical stability of MOF can be roughly evaluated according to the Pearson's hard/soft acid/base principle.^[81] On the one hand, carboxylate-based ligands can be regarded as hard bases, which form stable MOFs when they are combined with high-valency metal ions, such as MIL-53 and MIL-101. On the other hand, stable MOFs, such as zeolitic imidazole frameworks (ZIFs), can also be assembled by soft azolate ligands and soft low valence metal ions. Besides, the high connectivity of metal nodes and ligands, the hydrophobic properties of MOF surfaces, and the rigidity of linkers are also the crucial factors for the construction of robust MOFs.^[82] The prominent linkers for stable MOFs in the literature are usually carboxylate-based, and these MOFs can directly be used as highly active electrocatalysts for HER and OER, such as Fe-, Co-, and Ni-based MOFs constructed from terephthalic acid (H₂BDC) or functionalized H₂BDC organic ligands.^[83,84] Therefore, it is significant to rationally select metal and ligand species for stable active sites capable of driving desired electrocatalytic reactions.^[85–87]

HERs or OERs often occur in severe acidic or basic conditions. Therefore, MOF surfaces are either negatively (HER) or positively (OER) charged, and can therefore attract ions of the opposite charges when a voltage bias is applied, which may lead to the complete or partial destruction of MOF structures.^[88,89] In addition, metal sites would be reduced or oxidized when a specific potential is reached. Such changes of metal valence can influence the hardness and coordination conditions of metal nodes. Thus, the structural integrity and the actual active sites of MOF electrocatalysts during the reaction are worthy of consideration to better understand the catalytic mechanism or develop more effective catalysts. In electrochemical operating conditions for water splitting, MOFs can maintain the structural integrity, partially transform into new active phases, or undergo full degradation.

5.1. Intact MOFs

Some MOFs are highly stable in the water splitting conditions, and can retain the same crystal structures, components, and morphologies before and after catalytic reactions. Therefore, the metal sites in these 2D MOFs are usually regarded as active centers. Wang and co-workers reported highly efficient and robust NiRu-MOF nanosheet arrays toward electrochemical HER based on H₂BDC ligands.^[90] After this MOFs nanoarray being used in 1.0 M KOH electrolyte at –30 mA cm^{–2} for 24 h, the retention of surface composition and electronic configuration of this NiRu-MOF array were confirmed by scanning electron microscopy (SEM), transmission electron microscopy (TEM), high-angle annular dark-field scanning transmission

electron microscopy (HAADF-STEM), and X-ray photoelectron spectroscopy (XPS) analysis (Figure 4a–c). The active centers were confirmed to be Ni and Ru cations.

The ligands of H₂BDC and its derivatives with various functional groups (e.g., –OH, –NH₂) have been introduced to create 2D MOFs that are stable in the basic OER conditions. For instance, 2,5-dihydroxyterephthalic acid (H₄dobdc) was selected to convert 2D bimetallic FeCo oxides into ultrathin MOF-74 nanosheets (Figure 4d).^[91] After stability test for 10 000 s at the overpotential of 300 mV in 0.1 M KOH, its crystal structure and morphology could be maintained, as revealed by TEM (Figure 4e) and X-ray diffraction (XRD) (Figure 4f). The

mechanism research clarified that the excellent OER activity was attributed to the abundant coordinatively unsaturated Fe and Co sites. Recently, 2-aminoterephthalic acid (NH₂-BDC) was chosen as the organic ligand to construct water-stable 2D NH₂-MIL-88B(Fe₂Ni) MOF nanosheets, which exhibited highly efficient performance for overall water splitting with ultrastability.^[92] XPS spectra, SEM images, and XRD patterns (Figure 4g) jointly identified the structural integrity of MOFs after 30 h continuous operations at high current densities of 500 mA cm⁻² in 1.0 M KOH. Fe₂Ni(μ₃-O) and M/MO₆ clusters in NH₂-MIL-88B(Fe₂Ni) acted as the main active centers for OER and HER, respectively.

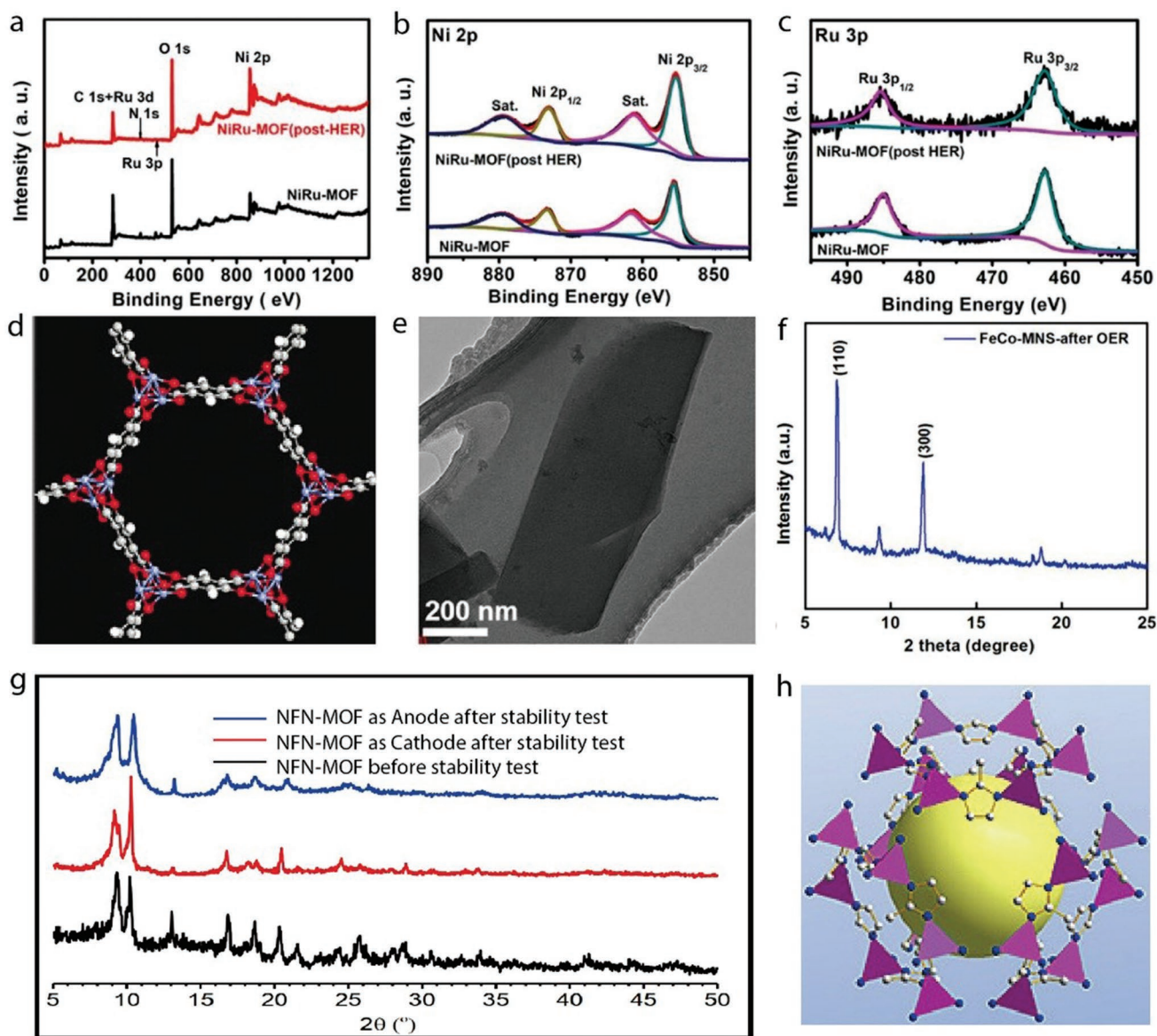


Figure 4. a) Survey XPS spectra for pristine and post-HER NiRu-MOF samples. High-resolution XPS spectra of b) Ni 2p and c) Ru 3p for NiRu-MOF before and after HER operations. a–c) Reproduced with permission.^[90] Copyright 2020, American Chemical Society. d) The model of secondary building units for MOF-74 nanosheets. e) TEM image and f) XRD pattern of FeCo MOF-74 after OER stability test. d–f) Reproduced with permission.^[91] Copyright 2019, Wiley-VCH. g) XRD patterns of NH₂-MIL-88B(Fe₂Ni) before and after chronoamperometric test toward water electrolysis at 500 mA cm⁻² for 30 h. g) Reproduced with permission.^[92] Copyright 2018, Wiley-VCH. h) The crystal structure of 2D ZIF-67. h) Reproduced with permission.^[95] Copyright 2019, Elsevier.

ZIFs are another significant subgroup of chemically robust MOFs, especially in alkaline environment, which can be directly used as OER electrocatalysts.^[93] The high affinity of nitrogen in 2-methylimidazole to the transition metal ions may greatly promote the interfacial electron transfer.^[94] Li and co-workers developed a facile route for integrating 2D ZIF-67 (Figure 4h) nanosheet arrays on the surface of CoNiAl-layered double hydroxide (LDH) nanoplatelets by an in situ crystallization–dissolution–recrystallization mechanism.^[95] The synthesized 3D hierarchical ZIF-67/CoNiAl-LDH showed highly efficient catalytic activity toward OER in 1.0 M KOH. SEM characterization of ZIF-67/CoNiAl-LDH after durability test at 50 mA cm⁻² displayed no conspicuous changes in structures or surface morphologies, confirming the structural stability. Based on the same ligand, Wang’s team successfully synthesized ordered trimetallic ZIF nanosheets (0.6 nm) by one-step hydrothermal reaction for the first time.^[96] This ultrathin 2D MOF structure afforded more active sites and better ion transfer pathway, while the addition of Fe and Co ions regulated the electronic configuration of Ni centers. When NiFe_{0.2}Co_{0.3}-ZIF electrode was tested at a constant current for 20 h in 1.0 M KOH, the sheet morphology was well preserved. Furthermore, XRD and XPS results displayed that the structure or chemical composition were consistent with the original ones. The exposed unsaturated active metal centers were responsible for the enhanced OER performance.

5.2. Partially Transformed

Other than maintaining intact crystal structure, 2D MOFs may go through significant changes of physicochemical properties under harsh operating conditions in water splitting, thereby leading to the formation of reconstructed surfaces or structures, which would contribute to the real mechanisms of OER and HER.^[97] A thorough analysis of the surfaces or structures of 2D MOFs in the reaction have revealed the proper structure–performance relationship. Diverse analytic strategies including electrochemical methods, microstructure, and spectroscopy characterizations can be conducted before and after electrocatalytic reactions to understand this reconstruction phenomenon, and identify the actual active species.^[98]

2D MOFs may be partially converted to other active phases whereas their overall structure can be retained. For example, Zhao and co-workers showed that NiO₆ units inside ultrathin NiFe-MOF (Figure 5a) nanosheets using 2,6-naphthalenedicarboxylic acid dipotassium as organic linkers were partially oxidized into NiO₆/NiOOH species during OER, and were partially reduced to form Ni/NiO₆ interface during HER.^[99] The durability of the NiFe-MOF structure after water electrolysis tests at 1.5 V in 0.1 M KOH for 20 h was further supported using XRD (Figure 5b) and SEM analysis. Liu and co-workers also found that NiFc-MOF (Fc: ferrocene) crystalline structure was partially converted to Fe₂O₂CO₃ and Ni(OH)₂/NiOOH phase after 40 h OER stability operation in 1.0 M KOH, which was demonstrated by XRD, XPS, and in situ Raman spectra.^[100] Apart from the postmortem analysis, comprehensive operando measurements were employed to probe the structural transformation occurring at the metal nodes of MOF. Tang’s group thoroughly studied the

OER catalytic mechanisms of 2D NiCo-MOF-74 (Figure 5c) in O₂-saturated 1.0 M KOH solution.^[101] As uncovered by HRTEM and in situ X-ray absorption spectra (XAS), NiCo-MOF-74 underwent a dynamical two-step reconstruction process with the corresponding metal hydroxide and oxyhydroxide species generating at relatively low (1.2–1.35 V) and high (1.35–1.5 V) applied potentials (Figure 5d,e). Despite drastic local structural changes during OER, NiCo-MOF-74 retained the original crystal structure (Figure 5f), displaying robustness and reversibility. The in situ formed Ni_{0.5}Co_{0.5}OOH_{0.75} with affluent oxygen vacancies and high metal oxidation states were responsible for the extraordinary OER performance. These recent studies indicated that the surfaces of MOFs may be transformed into new species in electrocatalysis, thereby the analysis of catalytic mechanism for MOFs should always consider whether such reconstruction exists during test conditions.

Partial valence transformation of 2D MOFs in the electrocatalytic process can also lead to the performance enhancement. Our group introduced a type of structurally stable 2D FeNi-MOF (ligand: thiophenedicarboxylate acid) nanobelt arrays with the tunable Fe/Ni ratios (Figure 5g).^[102] Interestingly, this FeNi-MOF exhibited a dynamic self-optimized phenomenon, while maintained a stable crystal structure during OER for a long period of time, as verified via XRD, selected area electron diffraction (SAED), Raman (Figure 5h), and Fourier-transform infrared (FT-IR) spectra. Systematic postmortem investigations conjectured that the gradual valence increments of Fe ions in bimetallic FeNi-MOF triggered the continuous activity improvement before reaching an optimal steady state (Figure 5i). This FeNi-MOF at stable conditions exhibited superb catalytic performance with a low overpotential of 308 mV at 200 mA cm⁻², a high turnover frequency (TOF) value of 0.261 s⁻¹ at an overpotential of 270 mV as well as outstanding long-term durability with large current tolerance. Theoretical calculations further revealed that Fe atoms were more active for OER and the transformation of Fe²⁺ to Fe³⁺ could accelerate the proton–electron transfers.

5.3. Fully Transformed

Different from the reaction mechanism in the abovementioned research, some pristine MOFs can be completely transformed into new oxides or (oxy)hydroxides, serving as the veritable active phases for water electrolysis. The reconstructed species can inherit the unique characteristics of original MOFs, accompanied by abundant vacancies, defects or coordination unsaturated metal sites, which are favorable for reaction processes.

As reported by Dou’s group, 2D Ni-MOF@Fe-MOF (ligand: H₂BDC) (Figure 6a) hybrid nanosheets displayed a dramatic enhancement of the catalytic activity toward water oxidation, and the post-OER catalysts were characterized with a series of techniques.^[103] Despite the morphologies of nanosheets could still be maintained, the complete transformation of Ni-MOF@Fe-MOF into Ni–Fe oxides nanoparticles after 50 cycles in 1.0 M KOH were demonstrated by HRTEM, XPS, and Raman spectroscopy (Figure 6b,c). In situ generated Ni–Fe oxides were regarded as the real active species of the hybrid catalysts during OER. Similarly, 2D bimetal MOF-Fe/Co nanosheets

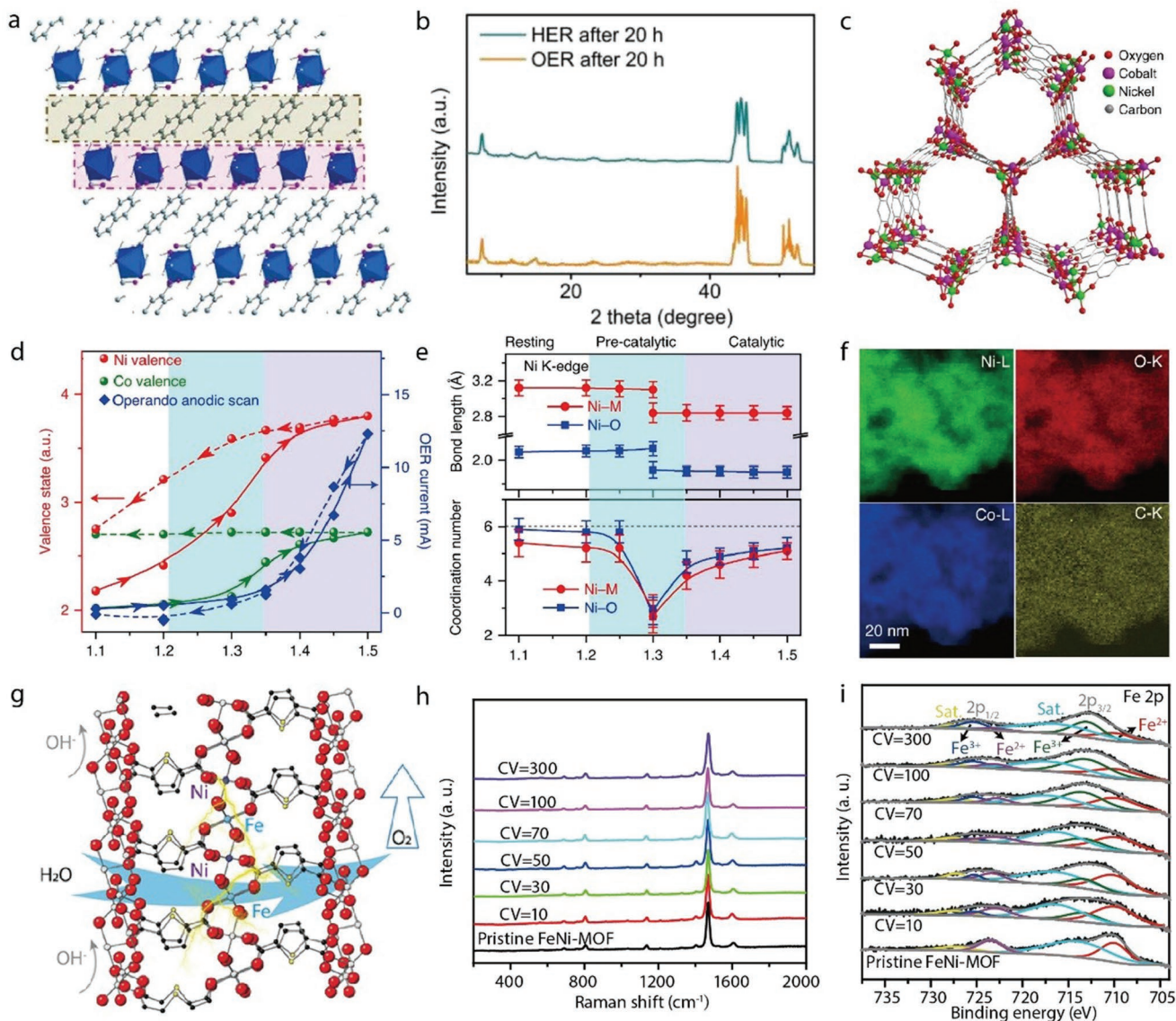


Figure 5. a) Crystal structure of NiFe-MOF. b) XRD profiles of NiFe-MOF after water electrolysis tests in 0.1 M KOH electrolyte. a, b) Reproduced with permission.^[99] Copyright 2017, Springer Nature. c) Crystal structure of $\text{Ni}_{0.5}\text{Co}_{0.5}\text{-MOF-74}$. d) The change of valence states and OER current for Ni and Co along with the applied potential. e) The change of bond length and coordination number for Ni–O and Ni–M. f) The EDS elemental mapping images of $\text{Ni}_{0.5}\text{Co}_{0.5}\text{-MOF-74}$ after OER process. c–f) Reproduced with permission.^[101] Copyright 2020, Springer Nature. g) Crystal structure of FeNi-MOF nanobelt. h) XRD patterns and i) high-resolution Fe 2p XPS spectra of FeNi-MOF after different CV cycles. g–i) Reproduced with permission.^[102] Copyright 2021, American Chemical Society.

using H_2BDC ligands were entirely transformed into CoO and FeO after 30 cyclic voltammetry (CV) cycles for OER in 1.0 M KOH.^[104] Based on the experimental and theoretical results, the 2D morphology and codoping of Fe/Co contributed to the superior OER performance. As to trimetallic 2D MOFs, the same reconstitution phenomenon occurs for water oxidation in alkaline condition. For instance, Zhang and co-workers observed the disappearance of characteristic structure of NiCoFe-based trimetallic MOFs (ligand: H_2BDC) (Figure 6d) along with CV cycles in 1.0 M KOH.^[105] By means of XRD, XPS, Raman, FT-IR, and X-ray absorption near edge structure (XANES) spectra (Figure 6e,f), it was confirmed that the metal hydroxide and oxyhydroxide evolved from pristine MOF acted as the real active species.

Recently, we designed and synthesized an ultralong quasi-2D Co-MOF (ligand: thiophenedicarboxylate acid) nanoarray that achieved superior electrocatalytic activity toward OER in 1.0 M KOH.^[106] Combining the pieces of evidence from SEM, HRTEM, XRD, and UV–vis reflectance spectra, the morphologies and structures of the Co-MOF after 30 h of OER at 20 mA cm^{-2} were changed. It was revealed that the higher performance was deciphered to stem from the hierarchical porous structure comprising in situ formed CoOOH nanosheets. In addition to these carboxylate-based ligands mentioned above, Prussian blue analogues (PBAs) linkers have been adopted to build 2D MOFs. For example, Wu and co-workers synthesized Co–Fe bimetallic PBA (Figure 6g) nanosheet arrays, which could effectively

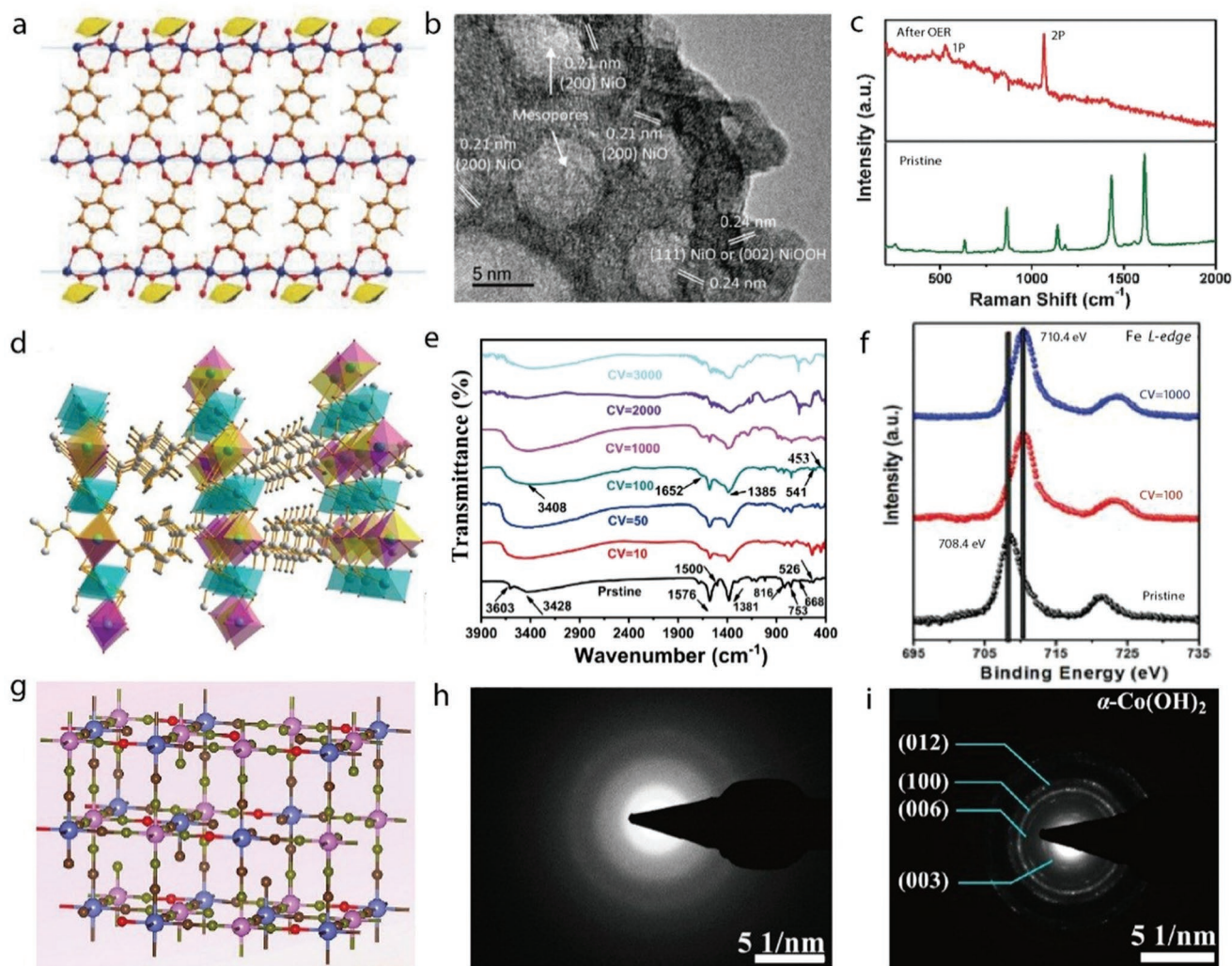


Figure 6. a) Crystal structure of Ni-MOF@Fe-MOF hybrid. b) HRTEM image and c) Raman spectra of Ni-MOF@Fe-MOF hybrid after OER testing. a–c) Reproduced with permission.^[103] Copyright 2018, Wiley-VCH. d) Crystal model of NiCoFe-MOF. e) FT-IR spectra and f) XANES of Fe L_{3,2}-edge for (Ni₂Co)_{0.925}Fe_{0.075}-MOF after various CV test. d–f) Reproduced with permission.^[105] Copyright 2019, Wiley-VCH. g) Crystal structure of CoFe-PBA. SAED patterns of CoFe-PBA nanosheets after long-term stability test for h) OER and i) HER. g–i) Reproduced with permission.^[37] Copyright 2020, Elsevier.

catalyze both OER and HER in 1.0 M KOH.^[37] With the help of XRD, FT-IR, XPS, Raman, TEM, and SAED characterizations (Figure 6h), it was identified that crystalline CoFe-PBA was decomposed to amorphous or low crystallinity metal oxyhydroxides during OER cycle for 24 h at 100 mA cm⁻². Nevertheless, SEM images suggested that the nanosheet morphology could be well inherited after cycling. Similar to the OER case, the in situ formed Co/Fe hydroxides function as active species for HER (Figure 6i).

6. Enhancing Intrinsic Electrocatalytic Properties of 2D MOFs

6.1. Intrinsically Conductive 2D MOFs

The poor charge transport of conventional MOFs, typically insulating, often restrains their effectiveness as direct

electrocatalysts for water splitting. Alternatively, intrinsically conductive 2D MOFs are considered to be the promising electroactive materials to facilitate the charge transport in water electrolysis. Conductive 2D MOFs usually have narrow bandgaps to promote effective charge transport.

For electrochemical applications, the linkers for fabricating conductive 2D MOFs usually have highly planar and conjugated structures containing orthosubstituted functional groups (e.g., OH, -NH₂, -SH), while the chelating metal centers are transition metals (e.g., Fe, Co, Ni) possessing unpaired electrons.^[107] According to hard-soft acid-base theory, the linkers with harder atoms such as O atom coordinating to comparatively soft metal ions generate large energy gaps or trapped valence states that impede conductivity.^[108] Incorporating softer atoms (e.g., N, S) result in more covalent binding, which can enhance MOFs conductivity, and thus promoting charge transfer during electrocatalytic process. In addition, the ligands size can affect the structural features of conductive MOFs, such as layer distance

and porous structure, and further influence the inherent catalytic properties.^[109] For example, Huang et al. showed that the larger linker endowed the conductive MOF with a favorable in-plane mesoporous structure for mass transport.^[110] Besides, they demonstrated that bidentate metal sites (M1-N₂) displayed higher activity for HER than M-N₄ linkage. The precise regulation of pore sizes and coordination environment of active centers affect the catalytic ability of conductive MOFs toward water splitting. On the other hand, the stability in acidic and alkaline solutions to avoid framework collapse needs to be considered when selecting ligands for the synthesis of conductive 2D MOFs.

Various preparation approaches may have a great impact on the morphology and functionality, and further influence the catalytic properties of conductive MOFs. For instance, Cu-BHT thin films were obtained via a liquid–liquid interface reaction, while Cu-BHT nanocrystals and amorphous Cu-BHT nanoparticles were synthesized through the homogeneous reactions.^[111] Although these three conductive MOFs prepared by different strategies possessed similar composition and electric conductivity (10³ S cm⁻¹), Cu-BHT nanoparticles with small size exhibited the best HER activities due to the large specific surface area and abundant exposed active sites. Therefore, by selecting the suitable conjugated organic ligands to reduce the size or thickness of conductive 2D MOFs can enhance their intrinsic electrochemical performance. The ligand structures and electrocatalytic HER and OER performance of representative conductive 2D MOFs are summarized in **Table 1**.

6.1.1. Design and Synthesis Strategies of Conductive 2D MOFs

The conduction mechanisms of intrinsically conductive MOFs are consistent with those of organic and inorganic semiconductors.^[112,113] From chemical perspectives, the possible charge transport in conductive MOFs can be through bonds or through space. The through-bond conduction relies on the charge transport via continuous coordination or covalent bonds, which are strongly influenced by the orbital symmetry, and energy level matching between metal moieties and organic ligands.^[113] The through-space conduction depends on the transport of charge carriers between the donor and acceptor units. For example, π – π interactions can provide spatial and orbital overlaps for charge transport through space.^[107] In conductive 2D MOFs, both metal centers and organic ligands can serve as the source of charge carriers.^[114] Based on the two conduction mechanisms, there are generally two strategies for the design of conductive MOFs. One pathway is to realize efficient charge transfer in MOF via the continuous coordination/covalent linkages, such as utilizing sulfur or nitrogen atoms coordinating to metal ions.^[115] For example, Dinca and co-workers proved the electrical conductivity of Mn₂(DSBDC) (DSBDC: 2,5-disulphydrylbenzene-1,4-dicarboxylic acid) was about one order of magnitude higher than that of Mn₂(DOBDC) (DOBDC: 2,5-dihydroxybenzene-1,4-dicarboxylic acid), indicating that Mn–S chains were more effective than Mn–O in terms of charge transfer.^[116] Another means for constructing conductive MOF is to take advantage of the high propensity of planar conjugated organic ligands to form frameworks containing π – π stacking.^[117] For instance,

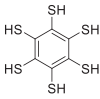
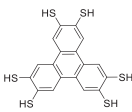
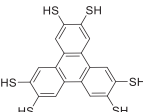
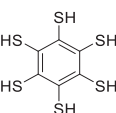
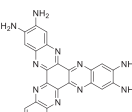
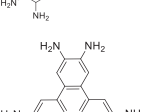
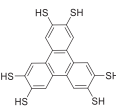
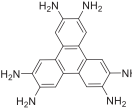
Park et al. fabricated a series of isostructural M₂(TTFTB) (M: Mn, Co, Zn, and Cd) based on tetrathiafulvalene tetrabenzoate (H₄TTFTB) ligand, which contained π – π stacked helical TTF and displayed high electrical conductivities range from 10⁻⁶ to 10⁻⁴ S cm⁻¹.^[118] Owing to the unique construction features, pristine 2D conductive MOFs have been explored directly as electrocatalysts.^[119]

At present, several strategies have been developed to construct 2D conductive MOFs by selecting appropriate metal ions and organic linkers. Hydro/solvothermal reaction and interface-assisted synthesis are the most commonly employed methods. Hydro/solvothermal synthesis is a liquid-phase chemical reaction in a sealed pressure vessel with water or other solvents under certain conditions.^[120] Controlling the reaction conditions, such as the solvent, temperature, and volume, can adjust the morphology and crystal structure of conductive MOFs. Interface-assisted synthetic routes, including liquid–liquid, liquid–solid, and gas–liquid interfacial approaches.^[121] Compared with hydro/solvothermal reaction, interface-assisted method is suitable for constructing single-layer or multilayer 2D MOFs and the thickness can be precisely controlled. In addition, the ball-milling method^[122] and electrochemical synthesis^[123] are also used to prepare conductive 2D MOFs.

6.1.2. Conductive 2D MOFs for HER

High electronic conductivity of metal dithiolene-based coordination frameworks makes them attractive candidates for electrocatalysis. Marinescu and co-workers successfully synthesized 2D conductive cobalt dithiolene MOFs of Co-BHT (BHT: benzenehexathiol) (**Figure 7a**) and Co-THT (THT: triphenylene-2,3,6,7,10,11-hexathiolate) with intrinsic electrocatalytic activity for HER.^[34] In acidic solution (pH = 1.3), Co-BHT and Co-THT showed low overpotentials of 340 and 530 mV at 10 mA cm⁻² and moderate durability for HER (**Figure 7b**). After the reaction, XPS displayed similar Co, Na, and S peaks with those observed before electrolysis, and inductively couple plasma mass spectrometry analysis of the resultant electrolysis solutions revealed no solubilized cobalt. These results indicated that the integration of cobalt dithiolene catalytic units into MOFs could afford high stability under reductive and acidic conditions. Overall, this intrinsic electrocatalytic performance was ascribed to the stable MOF structure and efficient cobalt dithiolene active species involving protonation of the sulfur sites on the dithiolene ligands after the initial reduction of Co³⁺/Co²⁺. In order to improve the HER performance of 2D MOFs, an ultrathin 2D Ni-THT single-layer nanosheet with a thickness of 0.7–0.9 nm was prepared by Langmuir–Blodgett method (**Figure 7c**).^[35] When used as HER electrocatalysts, these MOF nanosheets exhibited an overpotential of 333 mV at 10 mA cm⁻² (**Figure 7d**), much lower than that in a previous report where the same organic ligand was used.^[34] In addition, these Ni-THT nanosheets can function as HER catalysts over a wide pH range due to the robust coupling of THT monomers. The enhanced electrocatalytic performance of 2D Ni-THT nanosheets is attributed to their ultrathin monolayer feature, which facilitates the exposure of well-positioned active sites.

Table 1. Electrocatalytic HER and OER performance of electrically conducting 2D MOFs.

Ligands	Catalysts	Electrolyte	Overpotential [mV]	Tafel slope [mV dec ⁻¹]	Active sites	Refs.
HER						
	Co-BHT	pH = 1.3	η_{10} : 340	108	CoS ₄	[34]
	Co-THT	H ₂ SO ₄	η_{10} : 530	161		
	Ni-THT	0.5 M H ₂ SO ₄	η_{10} : 333	80.5	NiS ₄	[35]
	Co-BHT	pH = 1.3	η_{10} : 185	88	FeS ₄	[125]
	Ni-BHT	H ₂ SO ₄	η_{10} : 331	67		
	Fe-BHT		η_{10} : 405	119		
	Ni ₃ (Ni ₃ ·HAHATN) ₂	0.1 M KOH	η_{10} : 115	45.6	Unsaturated Ni-N ₂ sites	[110]
	Ni ₃ (HITP) ₂		η_{10} : 176	94.2		
	Co-THTA	0.5 M H ₂ SO ₄	η_{10} : 332	87	CoS ₂ N ₂ molecular	[126]
	NiAT	pH = 1.3 H ₂ SO ₄	η_{10} : 370	128	Ni complex unit	[127]
OER						
	NiPc-MOF	1.0 M KOH	η_{onset} : 250	74	NiN ₄	[128]
	Co ₃ (HHTP) ₂	0.1 M KOH	η_{10} : 490	83	Co atoms	[129]

The versatile metal atoms act as an essential part in chemical properties of MOFs and have been verified to be the active centers in many catalytic processes. Due to the distinct electron configurations and d-band centers, various metal ions can influence the electrochemical behavior of 2D MOFs, which was confirmed by density functional theory (DFT) calculations.^[124] The effect of different coordinated metal ions of conductive BHT-based 2D MOFs on HER has been assessed by Marinescu and co-workers (Figure 8a).^[125] As illustrated in Figure 8b, Co-BHT films with a thickness of 244 nm exhibited the lowest overpotential of 185 mV at 10 mA cm⁻² in comparison to that of Ni-BHT (331 mV) and Fe-BHT (405 mV) in acidic environment (pH = 1.3). The superior HER activity of Co-BHT was related to a higher electrochemically accessible surface area and lower charge transfer resistance compared to Ni-BHT and Fe-BHT. Recently, Chen and co-workers confirmed that the high unsaturation degree of metal atoms resulted in a stronger

ability to donate electrons for enhanced catalytic activity. The unsaturated metal sites could serve as highly active centers to improve the performance of traditional conductive MOFs toward electrocatalysis.^[110] In this work, hexaiminohexaazatriphenylene (HAHATN) was employed as a conjugated ligand to construct bimetallic sited conductive M₂(M₁·HAHATN)₂ MOF nanosheets (1.6 nm) with in-plane mesoporous structures (Figure 8c). Compared with Ni₃(HITP)₂ (HITP: hexaiminotriphenylene), Ni₃(Ni₃·HAHATN)₂ contained extra unsaturated Ni-N₂ moieties in addition to the same Ni-N₄ structures, and they also have high electrical conductivity (2 S cm⁻²) in favor of rapid electron transfer during electrocatalytic reaction. In 0.1 M KOH solution, linear sweep voltammetry (LSV) curves displayed that the optimal Ni₃(Ni₃·HAHATN)₂ has an overpotential of 115 mV at 10 mA cm⁻² for HER, much smaller than that of Ni₃(HITP)₂ (176 mV) (Figure 8d). The experimental results demonstrated that the Ni-N₂ moieties with higher

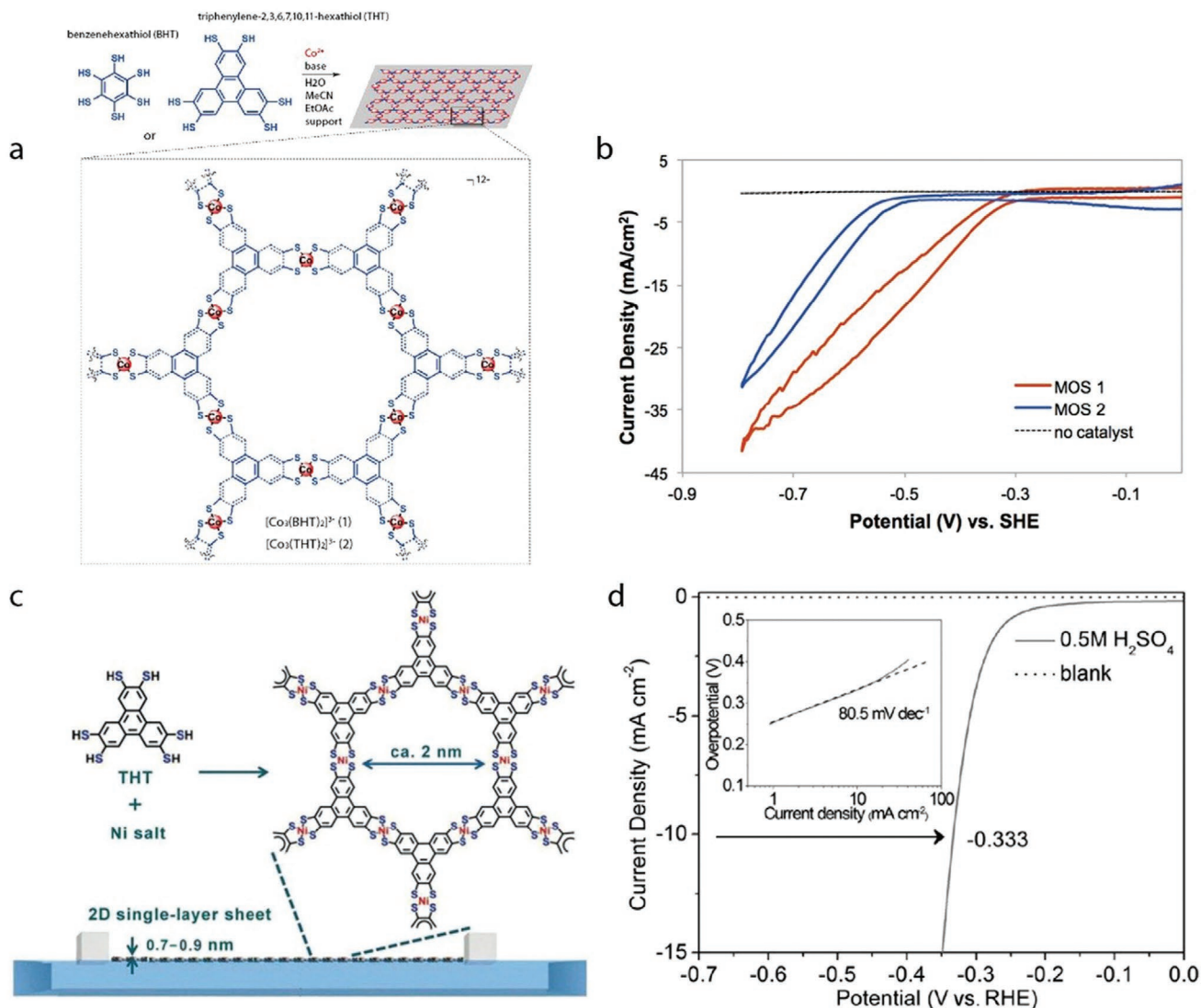


Figure 7. a) Fabrication of Co-BHT and Co-THT via a liquid–liquid interfacial approach. b) LSV of Co-BHT (MOS-1) and Co-THT (MOS-2) in H₂SO₄ solution (pH = 1.3). a,b) Reproduced with permission.^[34] Copyright 2015, American Chemical Society. c) Synthesis of 2D single-layer nanosheets of Ni-THT by using the Langmuir–Blodgett method. d) HER polarization plots of 2D Ni-THT MOFs and the blank glassy carbon electrode. Inset: the corresponding Tafel plot. c,d) Reproduced with permission.^[35] Copyright 2015, Wiley-VCH.

unsaturation degree have better HER activity than that of Ni-N₄ linkage. By regulating metal species, various HER activities of M₂(M₁₃·HAHATN)₂ (M₁:Co or Cu, M₂:Ni or Cu) further confirmed that the unsaturated M₁-N₂ site served as highly active center. DFT calculations revealed that Ni-N₂ moieties have stronger absorption and bonding capacity for proton, and therefore also reflected that the major catalytic active site was unsaturated M₁-N₂ moiety rather than M₂-N₄ linkage (Figure 8e,f). After electrochemical test, different characterizations proved the stability of initial MOF structures. Both experimental and theoretical results indicated the outstanding intrinsic catalytic activity of 2D Ni₃(Ni₃·HAHATN)₂ nanosheets for HER.

Other than inherently metal active sites, organic linkers composed of N, O, and S atom in 2D conductive MOFs also play an important role for electrocatalytic HER process. Feng and co-workers compared the HER activity of 2D conductive MOFs

synthesized from THT, THA (2,3,6,7,10,11-triphenylenehexamine) or their mixture ligands (THTA), and different metals (Figure 9a).^[126] The HER performances of these 2D MOFs with catalytic active centers of CoS₂N₂, CoS₄, and CoN₄ were evaluated in N₂-saturated 0.5 M H₂SO₄ solution. The optimized 2D Co-THTA MOF powders (single-layer Co-THTA: 0.87 nm) demonstrated an overpotential of 332 mV at 10 mA cm⁻², smaller than that of THT-Co (495 mV) and THA-Co (382 mV), indicating the order of catalytic activity follows CoS₂N₂ > CoN₄ > CoS₄ (Figure 9b). The definite active sites and the respective roles of Co, S, and N were uncovered by DFT calculations (Figure 9c,d), which suggested that Co–N units were the preferential sites for protonation in comparison with other possible active sites (N–N, N–S, –Co, Co–S, and S–S), while the coordination with S improved the hydrogen adsorption ability of atomic Co, resulting in an enhanced HER catalytic activity

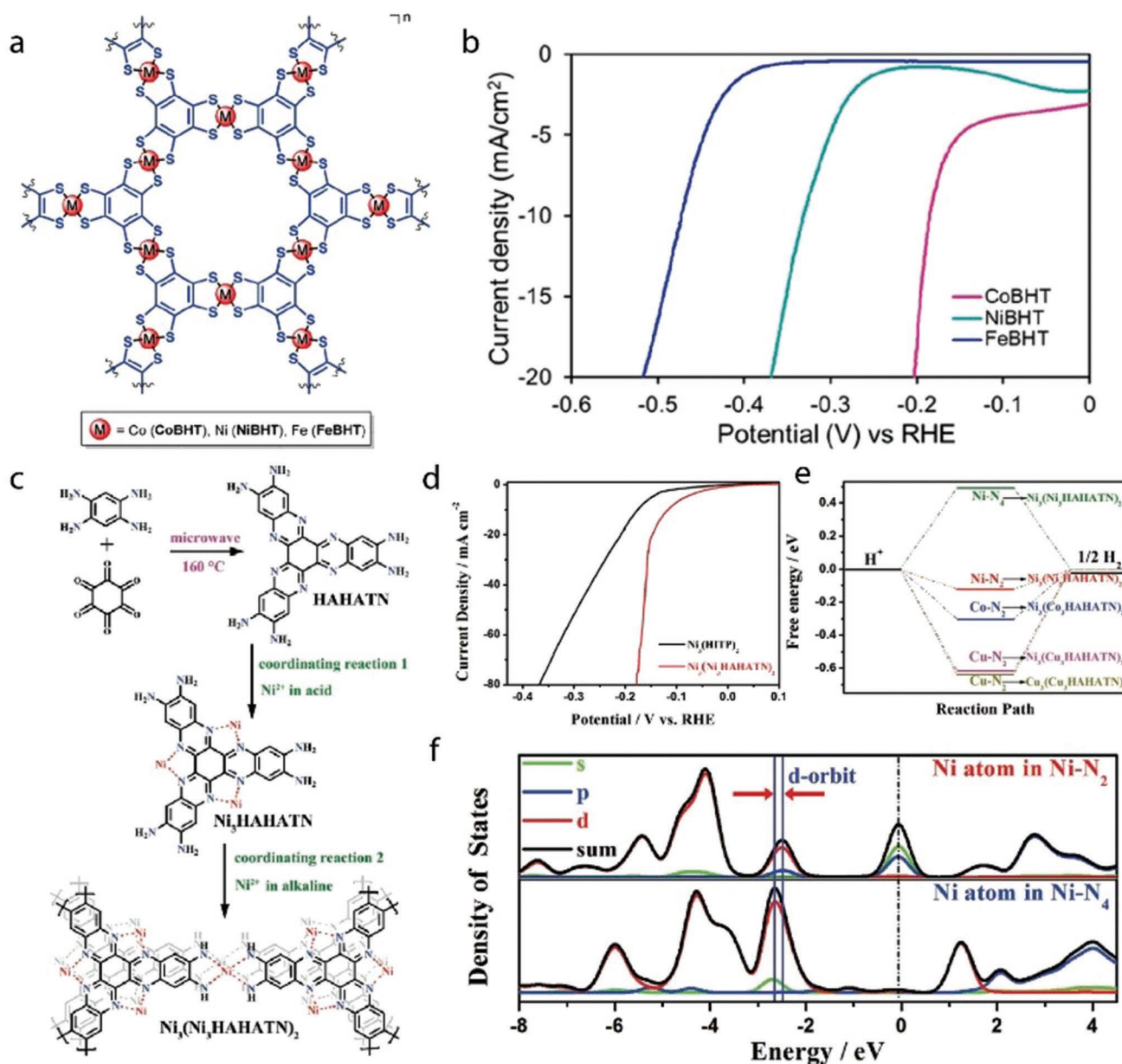


Figure 8. a) Structure of Co-BHT, Ni-BHT, and Fe-BHT coordination frameworks. b) LSV of HER for Co-BHT, Ni-BHT, and Fe-BHT. a,b) Reproduced with permission.^[125] Copyright 2018, American Chemical Society. c) Synthetic diagram of conductive $\text{Ni}_3(\text{Ni}_3\text{-HAHATN})_2$ MOFs with optimal HER activity. d) HER polarization curves of $\text{Ni}_3(\text{HITP})_2$ and $\text{Ni}_3(\text{Ni}_3\text{-HAHATN})_2$ samples. e) Free-energy profiles toward HER at various electrocatalytic sites. f) PDOS of Ni atom in Ni-N_2 and Ni-N_4 of the optimal $\text{Ni}_3(\text{Ni}_3\text{-HAHATN})_2$. c-f) Reproduced with permission.^[110] Copyright 2020, Wiley-VCH.

of CoS_2N_2 than CoN_4 and CoS_4 . Nishihara and co-workers synthesized an active Ni_xS_y moieties-containing single layer (0.6 nm) bis(aminothiolato)nickel (NiAT) nanosheets from Ni ion and 1,3,5-triaminobenzene-2,4,6-trithiol ligand.^[127] NiAT underwent a reversible interconversion to the electroconductive bis(iminothiolato)nickel (NiIT) nanosheets through $2\text{H}^+ - 2\text{e}^-$ reaction, causing large changes in band structures with a drastic enhancement of electrical conductivity (from 3×10^{-6} to $1 \times 10^{-1} \text{ S cm}^{-1}$). As a result, NiAT could serve as an efficient HER electrocatalyst with an operating overpotential of -370 mV at 10 mA cm^{-2} and strong durability in acids. The complete exposure of effective molecular catalytic sites

and excellent stability are responsible for their outstanding activity.

6.1.3. Conductive 2D MOFs for OER

In addition to HER, 2D conductive MOFs have been successfully designed for OER, which can be realized by selecting appropriate active metal nodes and linkers. In 2018, Du and co-workers first prepared a novel large π -conjugated 2D conductive nickel phthalocyanine-based MOF (NiPc-MOF) (Figure 10a) with high electrical conductivity of 0.2 S cm^{-1} via

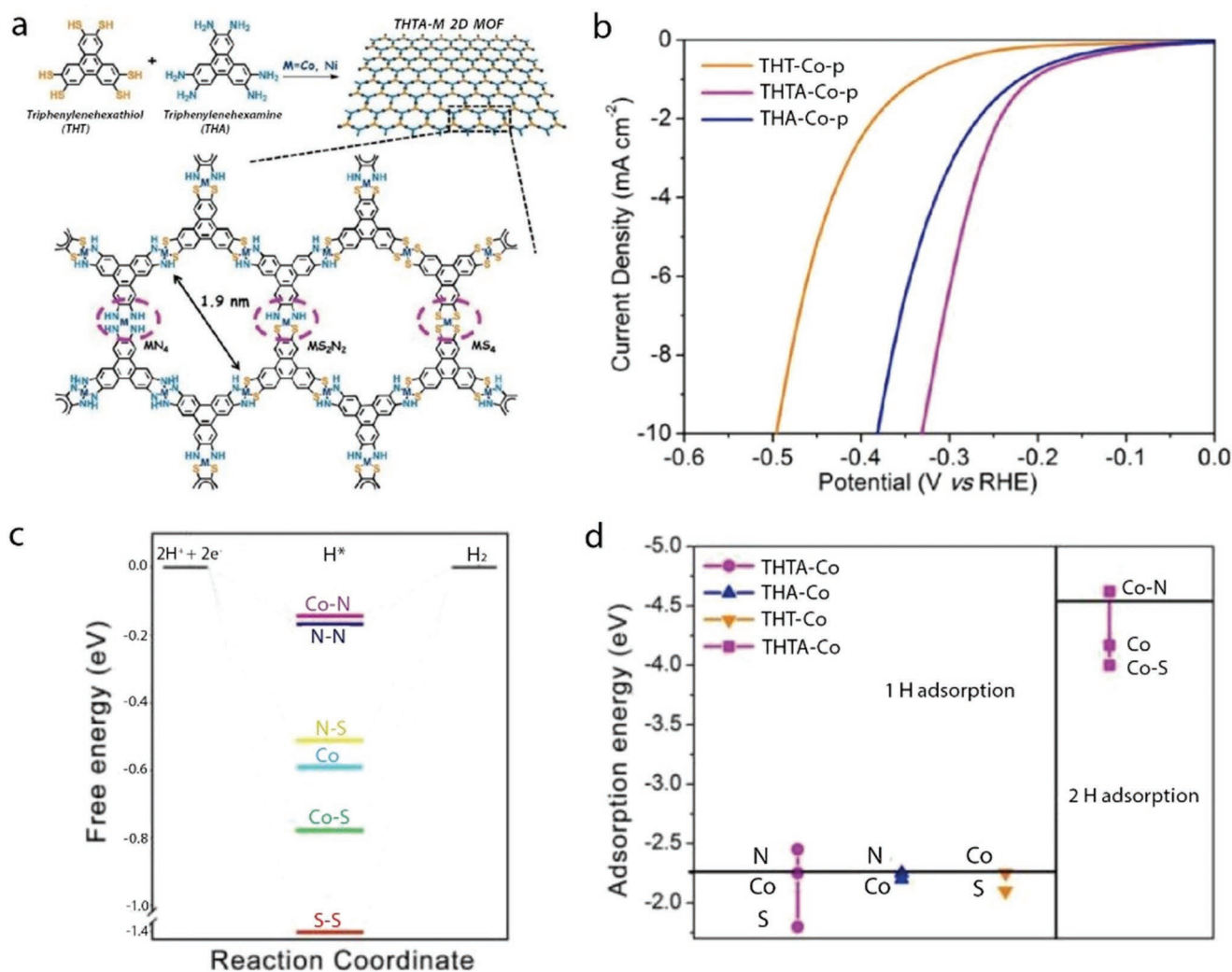


Figure 9. a) Synthesis and structure of 2D M-THTA (M: Co or Ni) MOFs. b) HER polarization plots of three types of 2D MOF powders. c) The adsorption energy of one H and two H radicals bonding to the proposed active sites on the surface of 2D MOFs. d) Free energy diagram of HER at equilibrium potential for possible active sites in 2D Co-THTA MOFs. a–d) Reproduced with permission.^[126] Copyright 2017, Wiley-VCH.

a bottom-up approach.^[128] The NiPc motif not only acted as the connecting unit but also served as an electrocatalytically active site for catalysis. Under alkaline conditions, NiPc-MOF films (300 nm) deposited on FTO has an ultralow onset overpotential (250 mV), high TOF values (2.5 s^{-1}), and excellent catalytic durability for OER (Figure 10b). Control experiments using organic monomers displayed current onset for OER at 420 mV, which was much more positive than that of NiPc-MOF. The superior OER performance of NiPc-MOF resulted from the unique conductive π -conjugated 2D MOF structure, which favored good conductivity and easy accessibility. After electrochemical measurements, the morphology and structure of the NiPc-MOF did not exhibit significant difference, as proved by the comparison of SEM images and Raman spectra. However, XPS showed that the shift of binding energy after OER resulted in a minor structural rearrangement, which was important to produce the key reaction intermediates and thereafter enhance OER activity. In the same year, Cao and co-workers also reported a fewer-layer π -conjugated conductive 2D

MOF based on 2,3,6,7,10,11-hexahydroxytriphenylene (HHTP) and Co^{2+} ions (Figure 10c).^[129] In 0.1 M KOH solution, the 4-layer $[\text{Co}_3(\text{HHTP})_2]_n$ nanosheets (2.85 nm) with the best performance produced ultrahigh mass activity of 64.63 A mg^{-1} under 1.7 V (vs RHE) and demonstrated long-term stability (Figure 10d). Furthermore, DFT calculation exhibited that the elementary reaction energy from OH^- to OH^* was consistent with the experimental results, confirming that Co atoms were the main active sites.

6.2. Ultrathin 2D MOF Nanosheets

Although intrinsically conductive 2D MOFs display outstanding electrocatalytic performance for HER and OER, their linker types are usually limited. In recent years, intrinsically insulating yet electrochemically active 2D MOF nanosheets have shown improved catalytic performance when their thicknesses are reduced to one or several monolayers. In this way,

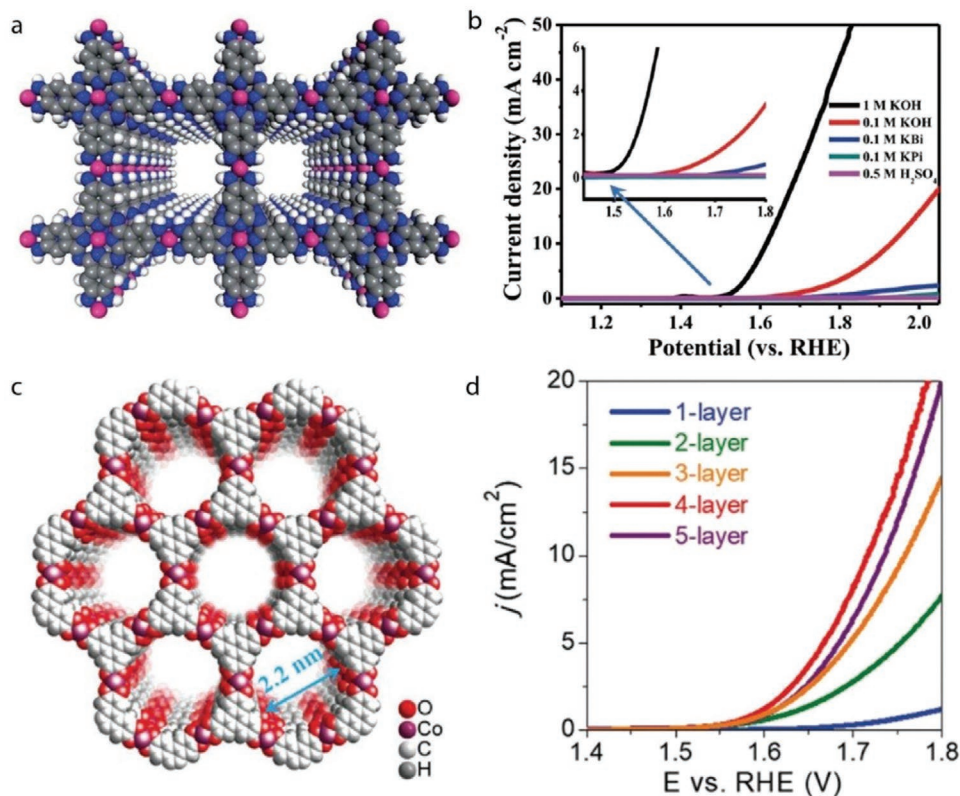


Figure 10. a) Chemical structure of NiPc-MOF. b) LSV curves of NiPc-MOF catalyst for OER in different solutions. a,b) Reproduced with permission.^[128] Copyright 2018, Royal Society of Chemistry. c) Packing model of π -conjugated $[\text{Co}_3(\text{HHTP})_2]_n$ nanosheets along the channels. d) OER polarization curves of $[\text{Co}_3(\text{HHTP})_2]_n$ with different layer numbers. c,d) Reproduced with permission.^[129] Copyright 2018, Royal Society of Chemistry.

high-density accessible active sites are exposed. Table 2 shows a summary of various nonconducting 2D MOF nanosheets that have been reported as OER and HER electrocatalysts. The metal sites in these 2D MOF nanosheets usually have a relatively high oxidation state, and often display significant catalytic activities in electrochemical oxidation reactions.^[130] Additionally, the ultrathin nature of these 2D MOF nanosheets not only enables the rapid mass transport of reactants and products, but also allows for the formation of vacancies, which act as shallow donors to increase the carrier concentration in 2D MOF, resulting in enhanced charge transfer.^[79,99]

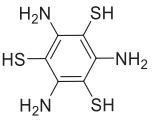
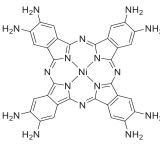
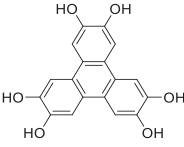
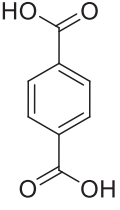
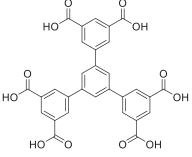
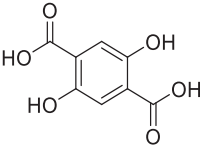
The approaches to the fabrication of 2D MOF nanosheets are mainly classified into two categories, including top-down (e.g., exfoliation by sonication) and bottom-up (e.g., direct solvothermal synthesis) methods.^[131,132] Top-down methods involve the exfoliation of bulk layered MOFs by breaking weak interplanar interactions, such as van der Waals forces and hydrogen bonding, into nanosheets. These nanosheets may be aggregated unless they have suitable mechanical and chemical stability.^[133] In comparison, the bottom-up approaches aim to directly prepare 2D MOF nanosheets from metal ions and organic ligands under appropriate synthesis conditions, in which the growth directions of MOF are limited.^[134,135] In comparison with the top-down means, the bottom-up methods can form sheet-like structures from nonlayered MOFs with uniform morphologies and thicknesses.^[77,136,137]

6.2.1. Ultrathin Monometallic MOF Nanosheets for OER

The activities of pristine 2D MOFs nanosheets for water electrolysis mainly originate from their open metal nodes.^[138,139] The exposure degree and the accessibility of these active sites affect catalytic efficiency of 2D MOFs.

In recent years, carboxylate-based 2D MOFs are constructed for electrocatalysis and demonstrate superb intrinsic catalytic performance. For example, Pang and co-workers synthesized ultrathin 2D Co-MOF nanosheets (≈ 2 nm) via a simple surfactant-assisted hydrothermal method using a mixed solution of Co^{2+} and H_2BDC .^[140] On the surface of Co-MOF nanosheets, the unsaturated tetragonal pyramidal metal centers were formed on account of the edge growth constraints. The ultrathin 2D Co-MOF electrode delivered a low overpotential of 263 mV at 10 mA cm⁻² and a Tafel slope of 74 mV dec⁻¹ in alkaline electrolyte. Interestingly, the ultrathin 2D Co-MOF nanosheets structure remained intact after short time (12 000 s) stability test, but completely collapsed to form amorphous materials after 20 h, indicating the electrocatalytic OER activity derived from their intrinsic framework structure. The superior electrocatalytic performance was ascribed to the exposed unsaturated metal active sites and the partial oxidation of Co^{II} to a higher valence state. Using the same ligand, Liu's group prepared Co-MOF nanosheets with a thickness of about 1 nm by the top-down strategy. The more preponderant exposed (110) and (31-1) lattice planes after ultrasound treatment could

Table 2. Recent achievements of pristine ultrathin 2D MOFs for OER.

Ligands	Catalysts	Electrolyte	Overpotential [mV]	Tafel slope (mV dec ⁻¹)	Active sites	Refs.
	Co-MOF	1.0 M KOH	η_{10} : 263	74	Unsaturated Co sites	[140]
	NiCo-MOF	1.0 M KOH	η_{10} : 250	42	Unsaturated Ni and Co centers	[36]
	NiFe-UMNs	1.0 M KOH	η_{10} : 260	30	Open Ni and Co sites	[144]
	Ni-Fe-MOF	1.0 M KOH	η_{10} : 221	56	Fe atoms	[145]
	HE-MOF-RT	1.0 M KOH	η_{10} : 245	54	Mn, Fe, Co, Ni, and Cu ions	[149]
	CoFe MOFs	1.0 M KOH	η_{10} : 274	46.7	Co and Fe sites	[151]
	NiFe-MOFs	1.0 M KOH	η_{10} : 230	86.6	Ni ³⁺ / ⁴⁺ sites	[156]
	Ni-MOF@Fe-MOF	1.0 M KOH	η_{10} : 265	82	Ni-Fe oxides	[103]
	MOF-Fe/Co	1.0 M KOH	η_{10} : 238	52	Co-O and Fe-O species	[104]
	CoNi ₂ -MOF	0.1 M KOH	η_{10} : 240	58	Co sites, hierarchical architecture	[146]
	FeCo MOF-74	0.1 M KOH	η_{10} : 298	21.6	Unsaturated Co and Fe atoms	[91]
	FeCo ₂ Ni-MOF-74	0.1 M KOH	η_{10} : 254	21.4	Fe, Ni, and Co sites, oxygen vacancies	[157]
	Ni _{0.5} Co _{0.5} -MOF-74	1.0 M KOH	η_{10} : 198	49	Ni _{0.5} Co _{0.5} OOH _{0.75} , oxygen vacancies	[101]
	Co-ZIF-9	1.0 M KOH	η_{10} : 380	55	N ₄ CoOOH	[141]
	2D-Co-NS	0.1 M KOH	η_{10} : 310	N/A	Exposed Co sites	[154]
	2D-CoNi	0.2 M PBS	η_1 : 344	171	Open Co and Ni sites	[155]

provide plentiful active sites and promote ions transport. As a result, the optimized Co-MOF afforded 10 mA cm⁻² with a low overpotential of 309 mV accompanied by small Tafel slope of 75.71 mV dec⁻¹. SEM and XPS analysis verified that the nanosheets structure, surface composition, and valence states of Co-MOF were the same as those of the original sample. The inherent 2D porous structure and abundant accessible Co

active centers were responsible for the enhanced electrocatalytic activities.

Because of the exceptional flexibility in structural/morphological engineering and composition control, ultrathin ZIFs also have been explored for water splitting.^[39] Fischer and co-workers obtained 2D Co-ZIF-9 (ligand: benzimidazole) nanosheets with thicknesses of 2–4 nm by liquid exfoliation of

the corresponding bulk phase.^[144] The 2D nanosheets required an overpotential of 380 mV to drive 10 mA cm⁻², smaller than that of bulk Co-ZIF-9. The surface species of catalysts during OER process were probed by operando Raman spectroscopy, revealing the formation of molecular N₄CoOOH under the influence of the applied potential. However, various oxygen species coordinated to the Co^{3+/4+} sites could not significantly alter the intrinsic and the overall crystallographic features of Co-ZIF-9. Post-OER characterizations further confirmed that the structure of catalyst remained intact after electrocatalytic measurements. Therefore, the exposed high-density active sites, the regulated electronic properties of Co sites by the coordinated N atoms together with fast mass transport lead to the exceptionally high OER activity.

6.2.2. Ultrathin Heterometallic MOF Nanosheets for OER

Due to the similar coordination mode between organic ligand and several metal nodes in the same MOF structure, metal centers can be readily substituted by various metal ions.^[142] Therefore, it is an effective way to attain heterometallic MOFs with well-preserved initial topology via the partial replacement of metal atoms. Compared to monometallic MOF, the controllable introduction of multiple metal centers enables the creation of more active sites and the regulation of the electronic environment of metal ions, which may result in a decrease of energy barrier to achieve an enhanced electrocatalytic activity. Furthermore, the coupling effect between various metal centers will also significantly improve the inherent catalytic activity. In particular, the inclusion of Ni–Co, Ni–Fe, and Co–Fe atomic pairs in heterometallic MOFs have displayed performance comparable or superior to that of noble metal catalyst.^[40,143]

Sonication synthesis method utilizing a mixed solution of Ni²⁺, Co²⁺, and BDC was proposed by Tang's group to fabricate ultrathin NiCo bimetal–organic framework nanosheets (NiCo-UMOFNs) with a thickness of ≈3.1 nm.^[36] The crystal structure of NiCo-UMOFNs in **Figure 11a** showed that each Co or Ni atom was octahedrally coordinated by six O atoms, and these pseudo-octahedra were further edge/corner connected with each other to generate 2D bimetal layers, separated by BDC molecules. Coordinatively unsaturated metal sites were formed on the exposed surface of 2D MOF nanosheets due to the partial termination of BDC ligands, which was further verified by XAS analysis and DFT calculations. In 1.0 M KOH solution, 2D ultrathin NiCo-UMOFNs exhibited excellent OER performance with an overpotential of 250 mV at 10 mA cm⁻², much smaller than that of Ni-UMOFNs (321 mV), Co-UMOFNs (371 mV), bulk NiCo-MOFs (317 mV), and commercial RuO₂ (279 mV) (**Figure 11b**). Importantly, post-OER characterizations confirmed the integrity of structure and morphology after a long-term durability test (**Figure 11c**). The theoretical results revealed that the unfilled e_g states of unsaturated metals were much less than those of fully-coordinated metals and a partial electron was transferred from Ni²⁺ to Co²⁺ through the O atom of ligands (**Figure 11d**), both of which were conducive to the improvement of OER electrocatalytic performance. Besides, Ni atoms had fewer unfilled 3d e_g states compared with Co, suggesting that Ni sites were more active in interacting with OER intermediates. Collectively,

the experimental and theoretical analysis clearly demonstrated that the coordinatively unsaturated metal atoms were the dominating active centers, and the coupling effect between Ni and Co could enhance OER activity. Similarly, NiFe bimetal 2D ultrathin MOF nanosheets (NiFe-UMNs) with a uniform thickness of ≈10 nm were fabricated, which were isostructural to NiCo-UMOFNs reported by Tang's groups (**Figure 11e,f**).^[144] As used as OER electrocatalysts, NiFe-UMNs possessed a lower overpotential of 260 mV at 10 mA cm⁻² compared to other comparative materials (**Figure 11g**). Meanwhile, the Tafel slope (30 mV dec⁻¹) of NiFe-UMNs was the lowest for OER reported to date, further demonstrating the outstanding reaction kinetics (**Figure 11h**). The morphology and matrix after durability test did not show noticeable changes with respect to the original NiFe-UMNs nanosheets, substantiating the excellent robustness. XPS spectra indicated that the addition of Fe can enhance Ni valence, and the higher valence Ni ions could accelerate OER process. DFT calculations also proved the bimetal coupling effect would significantly reduce the energy barrier, boosting OER activity (**Figure 11i**). Compared to CoFe-UMNs, the much higher activity of NiFe-UMNs should be assigned to the inherent preferable performance of Ni centers. Therefore, the surface exposed coordinatively unsaturated active metal sites and the positive synergistic interactions between Ni and Fe in NiFe-UMNs were responsible for the superior intrinsic performance.

Bottom-up solvothermal method has been proved as an effective method for the large-scale synthesis of a series of ultrathin 2D Ni-M-MOF (M: Fe, Al, Co, Mn, Zn, and Cd. ligand: H₂BDC) nanosheets with a thickness of several atomic layers (1.67–2.58 nm) (**Figure 12a**).^[45] In the preparation process, water molecule could limit the growth of coordination polymers by occupying metal coordination sites on the surface of each layer and acted as a good stripping agent at high temperature solvothermal reaction to form 2D nanosheets. As shown in **Figure 12b**, the edges of Ni-Fe-MOF tend to spontaneously curl due to their ultrathin nature. The HRTEM and SAED analysis further identified that the Ni-Fe-MOF nanosheets were highly crystalline (**Figure 12c**). The optimized Ni-Fe-MOF nanosheets exhibited remarkable OER performance with an overpotential of 221 mV at 10 mA cm⁻², far less than that of Ni-MOF (386 mV) and commercial Ir/C (311 mV). The morphology of Ni-Fe-MOF nanosheets was retained after 1000 CV cycles. From a structural point of view, these MOF nanosheets with coordinated H₂O and bridging μ-OH ligands might directly participate in the OER and improve the inherent activity. On the basis of characterization analysis and DFT calculations, it was concluded that there existed a strong interaction between two types of metal sites, in which Fe atoms acted as the main active sites for the outstanding catalytic activity.

By controlling the molar ratio of metal ions in solvothermal synthesis (ligand: hexacarboxylic acid 4,4',4''-benzene-1,3,5-triyl-hexabenzic acid), Bu's group constructed the novel isostructural 2D MOFs with hierarchical nanostructure (CTGU-10a2-d2) based on the corresponding single crystals (CTGU-10a1-d1) (**Figure 12d**).^[146] In particular, these unique bimetallic MOFs displayed excellent stability in alkaline conditions. At a Co/Ni molar ratio of 1:2, CTGU-10c2 formed hierarchical nanobelts constructed from nanosheets (**Figure 12e**) with a thickness

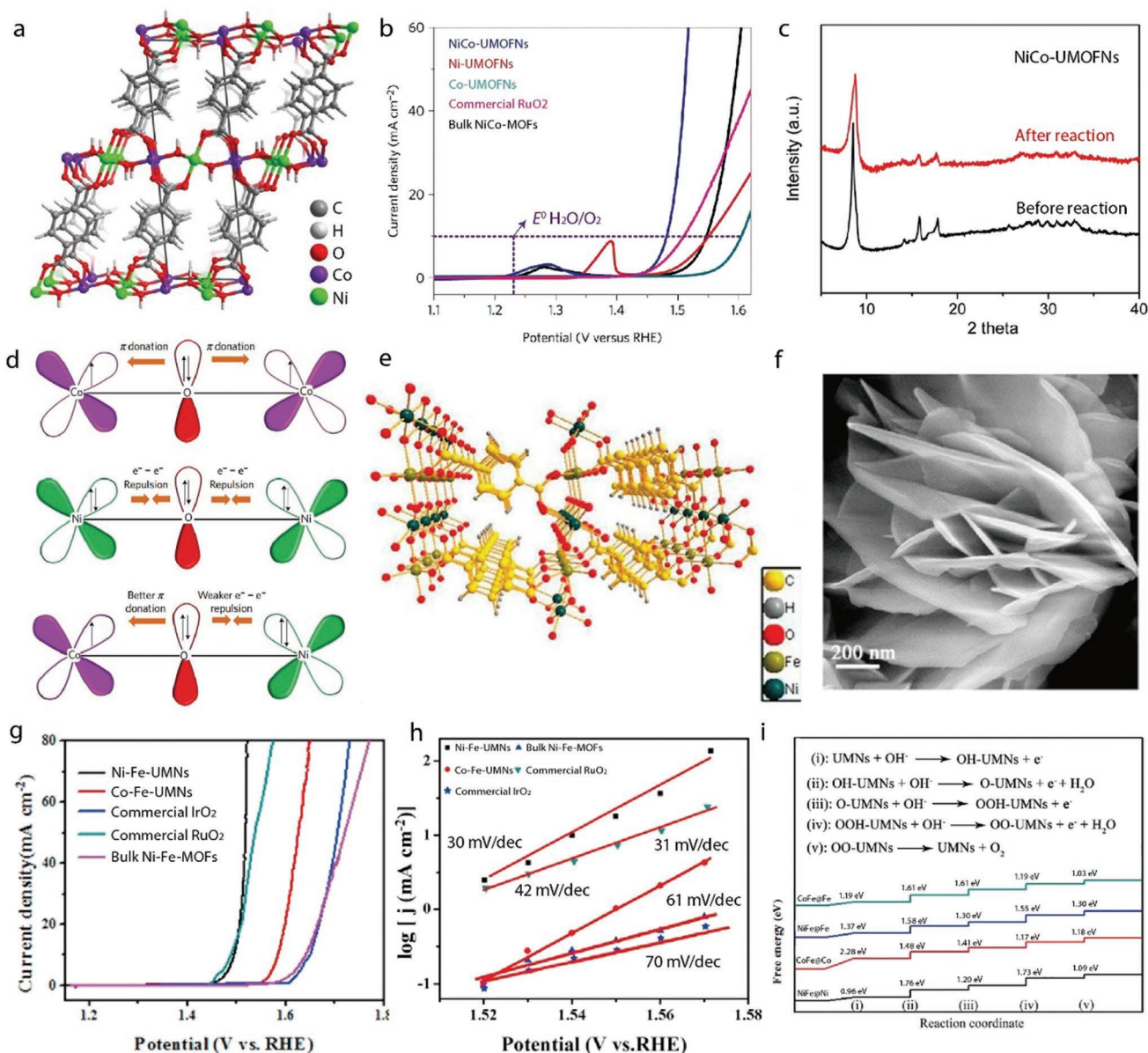


Figure 11. a) Crystal structure of NiCo-UMOFNs. b) OER polarization curves of NiCo-UMOFNs, Ni-UMOFNs, Co-UMOFNs, commercial RuO₂, and bulk NiCo-MOFs performed in 1.0 m KOH solution. c) PXRD patterns of NiCo-UMOFNs before and after OER reaction. d) Schematic representation of the electronic coupling between Co and Ni in NiCo-UMOFNs. a–d) Reproduced with permission.^[36] Copyright 2016, Springer Nature. e) Crystal structure and f) SEM image of NiFe-UMNs. g) LSV curves toward OER and h) the corresponding Tafel plots of NiFe-UMNs, CoFe-UMNs, bulk NiFe-MOFs, commercial RuO₂ and IrO₂ in 1.0 m KOH solution. i) Primitive steps and standard free energy diagram of OER process on NiFe-UMNs and CoFe-UMNs surfaces. e–i) Reproduced with permission.^[44] Copyright 2018, Elsevier.

of ≈1.03 nm. As exhibited in Figure 12f, CTGU-10c2 possessed the lowest OER onset potential of 140 mV, distinctly better than that of other as-prepared materials. Furthermore, a higher TOF value (0.05378 s⁻¹) of CTGU-10c2 than other hierarchical 2D MOFs, indicating the superior intrinsic activity. After OER test, XPS results proved the existence of electron transfer between Co²⁺ and Ni²⁺ through the oxygen of ligands. According to DFT calculations, Co atom was still the active center in case of the CoNi₂ structure, but the incorporated Ni atom would lead to distortion, thus improving the catalytic activity of the Co center. Both experiments and DFT simulation indicated that

the outstanding OER performance derived from the presence of unsaturated metal sites, a unique hierarchical architecture and the bimetal coupling effect.

High entropy materials involves the introduction of five or more metal elements into single-phase crystal structures, thereby tuning the adsorption energy of reacting species on the catalyst surface.^[147,148] Recently, Mu and co-workers introduced the concept of high entropy into MOFs (Figure 13a).^[149] They synthesized an ultrathin high entropy MOF (HE-MOF-RT) with a thickness range of 3.5–4.0 nm from a mixed solution of five metal species (Mn²⁺, Fe³⁺, Co²⁺, Ni²⁺, and Cu²⁺) and

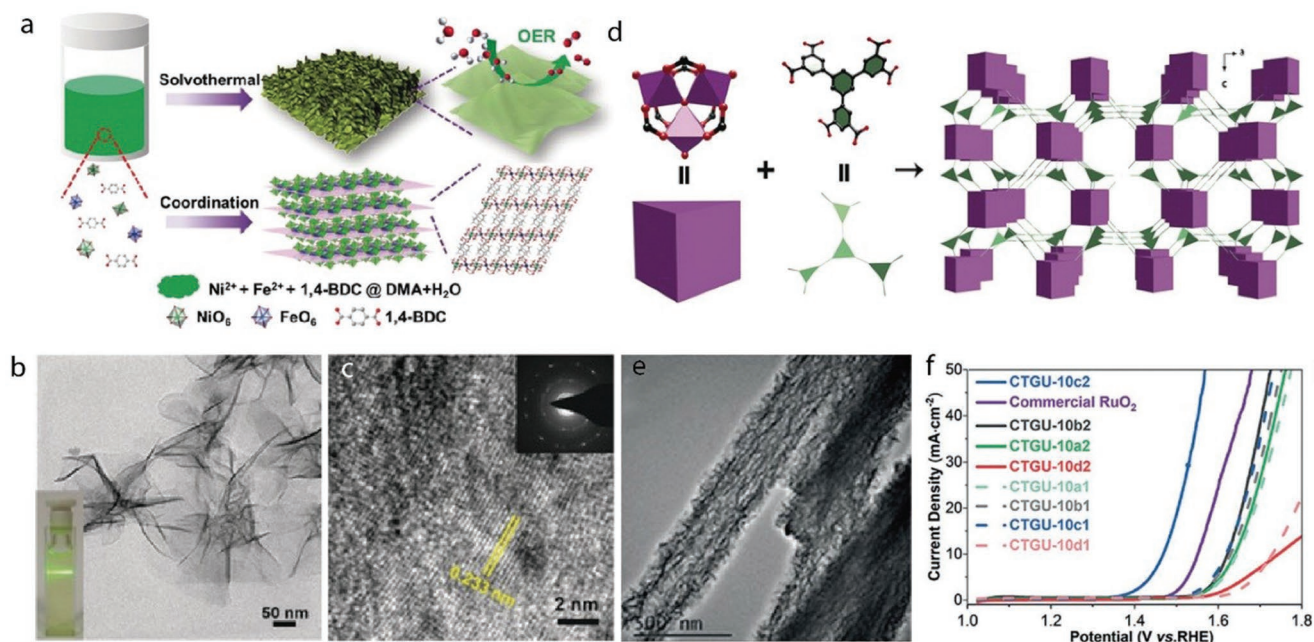


Figure 12. a) Synthetic procedure of ultrathin Ni-Fe-MOF nanosheets. b) TEM image of Ni-Fe-MOF nanosheets. Inset: tyndall effect of the transparent colloid suspension. c) HRTEM image of Ni-Fe-MOF nanosheets. Inset: selected area electron diffraction analysis. a–c) Reproduced with permission.^[145] Copyright 2019, Wiley-VCH. d) Schematic of the fabrication of 2D hierarchical MOFs. e) HRTEM image of CTGU-10c2. f) Polarization curves of commercial RuO₂ and the CTGU electrocatalysts for OER in 0.1 M KOH. d–f) Reproduced with permission.^[146] Copyright 2019, Wiley-VCH.

BDC ligands by a solution phase method under ambient temperature. This solution phase strategy could hold better mass transfer and homogeneous thermal distribution compared to solvothermal reaction, thereby producing the 2D nanosheet on a large scale. In the resulting HE-MOF-RT, five metal elements were near-equimolar uniformly distribution. HE-MOF-RT showed the efficient OER performance with an overpotential of 245 mV at 10 mA cm⁻², much lower than those of HE-MOF-ST (293 mV) and commercial RuO₂ (346 mV) in alkaline systems (Figure 13b). As shown in Figure 13c–e, the crystal structure and sheet-like morphology of HE-MOF-RT were completely maintained after 48 h electrolysis, manifesting the excellently stability. Despite the electrochemical formation of metal oxides and (oxy)hydroxides during OER, the chemical environment of Ni/Co-based active centers barely changed owing to the remained bonded to six O atoms in NiO/CoO. Compared with HE-MOF-ST (ST: solvothermal reaction), the higher intrinsic activity of HE-MOF-RT may originated from the ultrathin structure, the large surface area and the synergistic effect of five metal ions.

Ultrathin heterometallic MOF nanosheets can also be synthesized by a template method to attain large specific surface area and more coordinatively unsaturated metal sites, greatly improving the electrocatalytic properties.^[150] For instance, Zhu and co-workers used the amorphous metal oxide nanosheets (M-ONS) as sacrifice templates to form MOF-74 nanosheets (M-MNS) by confined 2,5-dihydroxyterephthalic acid coordination (Figure 14a).^[91] As presented in Figure 14b, FeCo-MNS exhibited an ultrathin nanosheet morphology with the thickness of merely 2.6 nm, which could not be obtained through the delamination of their bulk counterparts or the traditional solvothermal method. This strategy could avoid the structure damage

via top-down ultrasonication or active site blockage by alien compounds during the bottom-up synthesis. The controllable leaching of metal ions from M-ONS by acidic ligand solutions leads to the enrichment of metal ions neighboring to M-ONS surface, further resulting in the confined growth of MOFs into 2D nanostructure. The successful preparation of BTC (trimesic acid) MOF nanosheets with the thickness of 1.5 nm also confirmed the generality of this approach. In 0.1 M KOH electrolyte, the optimized FeCo-MNS-1.0 has the lowest OER overpotential of 298 mV at 10 mA cm⁻² (Figure 14c), outperforming the state-of-the-art NiCo-BDC nanosheets. After OER operation, the similar diffraction peaks and morphology verified the stable structure, whereas the decreased XRD peak intensity indicated the partial transformation of FeCo-MNS-1.0 into amorphous species. Compared to bulk MOF-74, the coordination numbers of Co-ligand and Fe-ligand in FeCo-MNS-1.0 decreased to 4.5 and 4.0, indicative of the creation of extra coordinatively unsaturated metal sites (Figure 14d). The EXAFS conclusions confirmed that the plentiful coordinatively unsaturated metal sites of FeCo-MNS-1.0 contributed to its superior OER activity than FeCo-MB. In addition, DFT calculations verified that the heteroatom synergy between Co and Fe can successfully tune the OH* adsorption energy barrier to an appropriate value, leading to the enhanced OER performance.

Using the similar synthetic strategy, Li's group developed ultrathin 2D CoFe MOF (ligand: H₂BDC) nanosheet (4.84–7.39 nm) derived from 2D LDHs (Figure 14e).^[151] This ligand-assisted transformation underwent an obvious crystal dissociation, recrystallization, and irregular growth process. As displayed in Figure 14f,g, Co, Fe, and O elements were uniform distribution throughout the obtained 2D MOF nanosheets. Interestingly, weakly crystallinity 2D CoFe MOFs has an

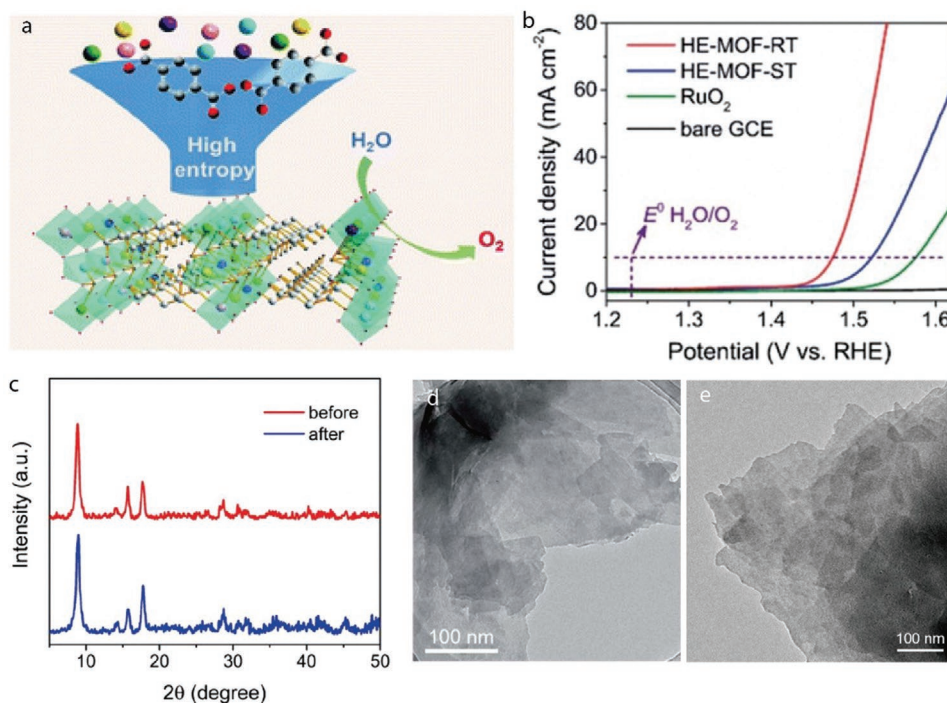


Figure 13. a) Schematic diagram of crystal structure and water oxidation of HE-MOF-RT. b) LSV curves of HE-MOF-RT, HE-MOF-ST, and commercial RuO₂. c) XRD pattern, and d,e) TEM images of HE-MOF-RT nanosheets before and after stability test, respectively. a–e) Reproduced with permission.^[149] Copyright 2019, Royal Society of Chemistry.

overpotential of 274 mV at 10 mA cm⁻², lower than that of CoFe MOFs (300 mV) with better crystallinity and high specific surface. XANES spectra demonstrated that the more unsaturated metal sites and local structural distortion on weakly crystallinity 2D CoFe MOFs surfaces lead to the accelerated OER process. After the continuous 70 h measurement, the morphology and structure of 2D MOF were consistent with the observation before pre-reaction. In general, although the coupling effect between Co and Fe could promote OER activity, the superior catalytic capability mainly originated from the unique 2D characteristics, which enabled more exposed active sites and facilitated electron transfer and ion diffusion.

2D MOF heterometallic nanosheets with high yield and uniform thickness can also be produced by a wet chemistry method to eliminate regulators or surfactants. A facile synthetic approach was provided to construct bimetal MOF-Fe/Co (ligand: H₂BDC) nanosheets (2.2 nm) at a large scale via simple stirring (Figure 15a).^[104] During the preparation process, H₂O and TEA stabilized the edges of 2D MOF layers and prevented 3D aggregation. The MOF-Fe/Co (1:2) delivered a small overpotential of 238 mV at 10 mA cm⁻², which was much lower than that of bulk MOF-Fe/Co (427 mV) and 3D MOF-Fe/Co (1:2) (311 mV). Based on XPS and Raman spectra (Figure 15b), MOF-Fe/Co completely transformed into Co–O and Fe–O structures in electrocatalysis immediately and these Co–O and Fe–O species exhibited superior stability. Theoretical analysis indicated that the introduction of Fe atoms could modify the electronic state of Co centers, which regulated the adsorption energy of rate-determining step, thereby promoting the OER catalytic activity. Zhang and co-workers put forward a mild ambient

temperature solution phase strategy to prepare the hierarchical NiCoFe-based trimetallic MOFs (ligand: H₂BDC) (Figure 15c), which delivered a low OER overpotential of 257 mV to produce 10 mA cm⁻² and a negligible stability attenuation.^[105] To decipher the possible origins of the remarkable OER performance, the structural, chemical, and electronic evolution processes of intermediates after various CV cycles were investigated. As reflected by XRD, FT-IR, XPS, and Raman spectra, MOFs structure completely disappeared, forming the pure hydroxide and oxyhydroxide species after 100 CV cycles. Importantly, the compositions, electronic structure, and morphology of the intermediates after 1000, 2000, and 3000 cycles remained consistent, indicating that the metal hydroxide and oxyhydroxide evolved from the pristine MOFs were the real active species.

6.2.3. Defect Engineering of Ultrathin MOF Nanosheets for OER

Most of the pillared-layer type MOFs are stable enough under various reaction conditions.^[152] Unfortunately, in most cases, the metal centers of MOFs are almost fully occupied by organic linkers, consequently leading to weak catalytic activity. Defect engineering has been evidenced as a highly effective approach, which can result in a missing occupation of linkers at metal nodes, thus greatly enhancing the catalytic activity of inactive MOFs.^[153] Nevertheless, selective breaking of coordination bonds between the layers to create more unsaturated metal sites or defect remain to be solved.

Recently, the electrochemically/chemically oxidative strategy was employed to exfoliate the pillared-layer MOFs by Zhang

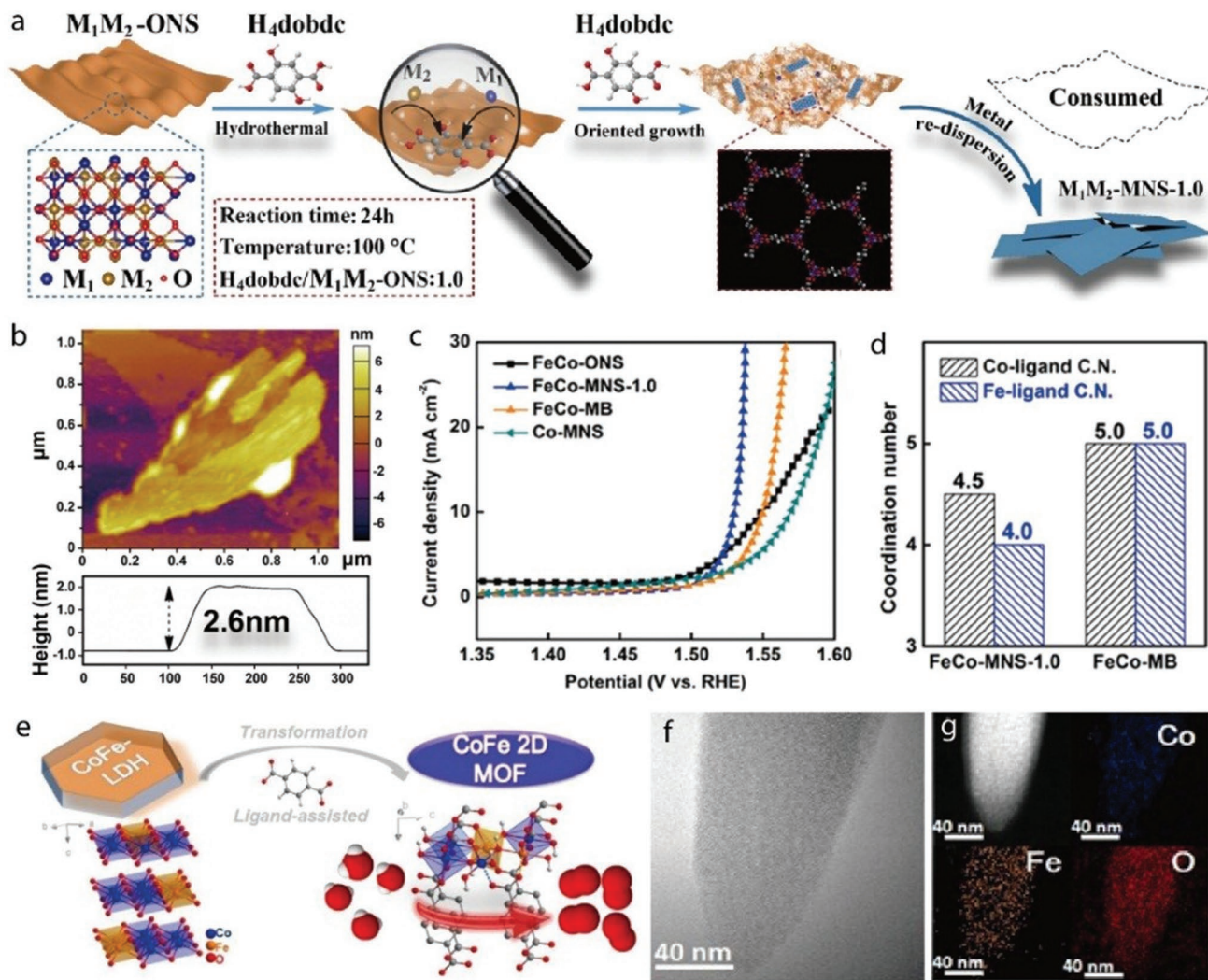


Figure 14. a) Schematic illustration of the synthesis of MOF-74 nanosheets through 2D oxide sacrifice approach. b) AFM image and the corresponding height curves of FeCo-MNS-1.0. c) OER polarization curves of FeCo-ONS, FeCo-MNS-1.0, FeCo-MB, and Co-MNS in 0.1 M KOH. d) The coordination numbers for Co–ligand and Fe–ligand of FeCo-MNS-1.0 and FeCo-MB. a–d) Reproduced with permission.^[91] Copyright 2019, Wiley-VCH. e) Schematic illustration for the ligand-assisted transformation from 2D LDHs to 2D MOFs. f) High-angle annular dark field scanning TEM image, and g) energy dispersive spectroscopy elemental mapping images of LM-160-12 for Co, Fe, and O atoms. e–g) Reproduced with permission.^[151] Copyright 2020, Royal Society of Chemistry.

and co-workers (Figure 16a).^[154] They used redox active pillar ligand to construct 3D pillared-layer MOFs, in which the backbone could be oxidized to lower their coordination ability and subsequently be selectively removed, while the ultrathin 2D MOF nanosheets layers maintained intact and exposed more open metal sites as catalytically active centers. In detail, they first synthesized 3D-Co MOFs by treating the cobalt acetate tetrahydrate and 2,3-dihydroxy-1,4-benzenedicarboxylic acid (H_4dhdhc) mixed solution at 140 °C. Then, the electrochemical exfoliation in the process of OER removed the pillar ligands in 3D-Co MOFs and in situ obtained the 2D nanosheets (2D-Co-NS) with a thickness of 2 nm. Figure 16b–d displayed the corresponding morphology evolution from the 3D-Co to 2D-Co-NS. This conversion process was also achieved slowly by immersing 3D-Co in an O_2 saturated electrolyte and ultrasonic treatment. As shown in Figure 16e, with the generation of 2D-Co-NS

during the electrochemical exfoliation process, the overpotential of OER at 10 mA cm^{-2} was gradually reduced from the initial 429 mV and finally stabilized at 310 mV. Compared with 3D-Co, the ultrathin 2D-Co-NS possessed exceptionally high activity due to their unique defect structure. In addition, the highly crystalline 3D-Co was transformed to an amorphous phase rather than CoO_x after the stabilization of OER performance. Similarly, Huang and co-workers proposed a novel method for the preparation of single layer metal–organic nanosheets from 3D pillared-layer MOFs (ligand: 1,4-benzenedicarboxylic acid and 1,4-diazabicyclo-[2.2.2]octane) based on the anisotropy of coordination bonds (Figure 16f).^[155] They used rectangular pillared-layer 3D-Zn MOF (Figure 16g) as the precursor in which the pillars could be completely eliminated by substitution with terminal capping solvent molecules, thus affording isostructural layered 2D-Zn MOFs (Figure 16h). Meanwhile, the

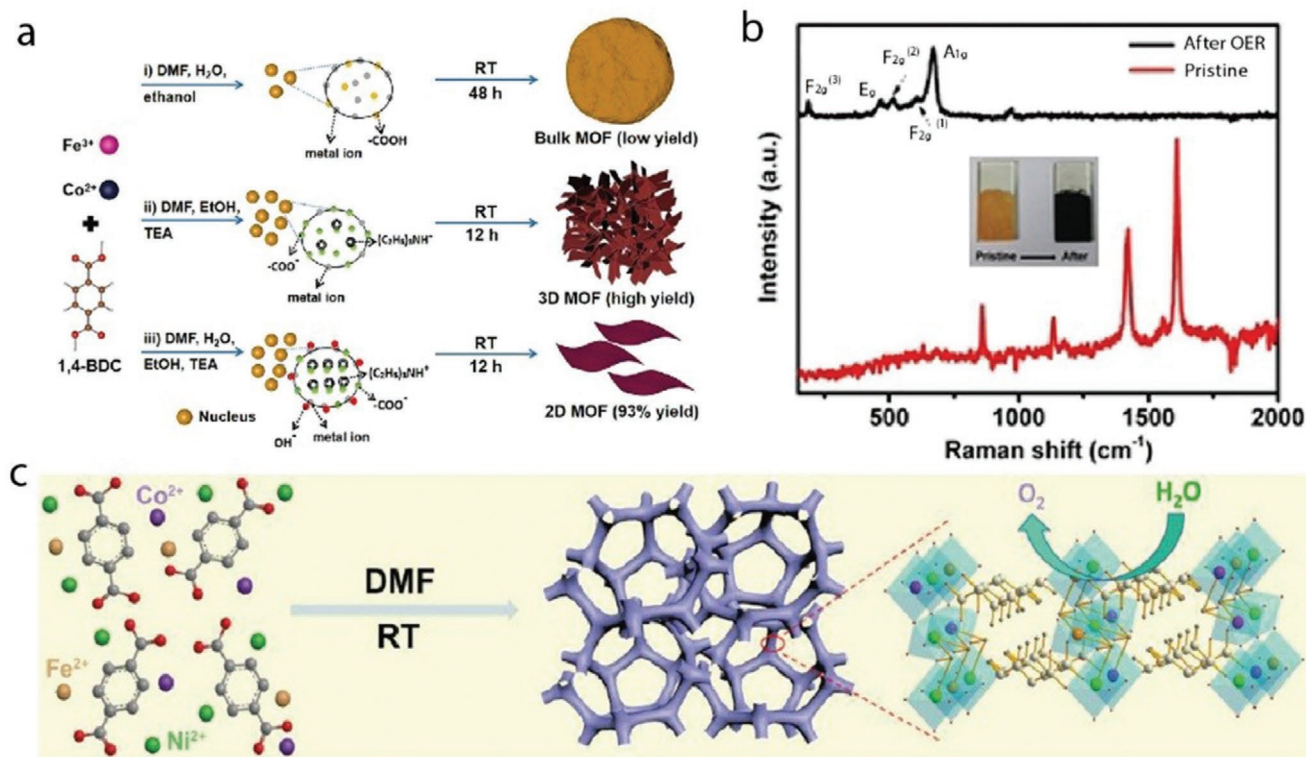


Figure 15. a) Illustration of the preparation of bulk, 3D, and 2D MOFs. b) Raman spectra for the 2D MOF-Fe/Co before and after OER operation. a, b) Reproduced with permission.^[104] Copyright 2021, Wiley-VCH. c) The fabrication process of hierarchical $(\text{Ni}_2\text{Co})_{1-x}\text{Fe}_x\text{-MOF}$ nanofoam at ambient temperature. c) Reproduced with permission.^[105] Copyright 2019, Wiley-VCH.

synchronously external forces prevented the reaggregation of the generated layer-like nanosheets, resulting in the single layer 2D-Zn MOF nanosheets (Figure 16i) with ultrathin thicknesses (≈ 0.9 nm). As demonstrated in Figure 16j, single-layer 2D MOF nanosheets composed of redox-active metals (Co, Ni) exhibited superior electrocatalytic OER performance in 0.2 M phosphate buffered saline (PBS) solution. Notably, 2D-CoNi-single-layer has the lowest overpotential of 344 mV at 1 mA cm^{-2} owing to the synergistic effect of active metal sites. After OER, the results of TEM and Raman spectra indicated that the morphology and composition remained constant, manifesting good electrochemical stability of 2D single-layer MOF nanosheets.

Strain regulation is a powerful approach to alter the inherent interatomic distance in MOFs, and thus the geometrical and electronic structure around metal centers could be modified to optimize the electrocatalytic performance. Yan and co-workers reported a rational linker scission strategy to induce lattice strain in 2D NiFe-MOFs by partially replacing BDC linkers with monocarboxylic acid ligands.^[156] After the introduction of nonbridging linkers, interlayer spacing was enlarged and the diffraction peak shifted significantly. The overpotential of lattice strained NiFe-MOFs with 6% lattice expansion was reduced to 230 mV from 320 mV for the pristine NiFe-MOFs at 10 mA cm^{-2} . According to XAS, XPS spectra, and theoretical calculations, $\text{Ni}^{3+}/^{4+}$ sites were the active centers, and the improved OER activity was ascribed to the optimized Ni 3d e_g -orbital, thus facilitating the rate-determining step to form $^*\text{OOH}$ intermediates. After 20 000 s of operation, the metal

atom arrangement and the chemical states kept unchanged, indicating the excellent structural stability of the strained NiFe-MOFs.

The creation of oxygen vacancies in MOF catalysts is an efficient strategy to expose more active sites and regulate the charge density for accelerating catalytic process. Recently, Mu et al. constructed the ultrathin 2D FeCoNi-MOF (ligand: 2,5-dihydroxyterephthalic acid) nanosheets with 1.5 nm thickness and abundant oxygen vacancies.^[157] In 0.1 M KOH, the formed defect-rich $\text{FeCo}_2\text{Ni-MOF-74}$ displayed a low overpotential of 254 mV at 10 mA cm^{-2} and outstanding stability for over 100 h. After a long-term OER test, the shape, atom arrangement, and XRD pattern were well maintained, indicating a stable structure of MOF-74. The electrochemical results suggested that Fe doping and oxygen vacancies can substantially improve the electron-transfer efficiency. DFT calculations further demonstrated that the coupling effect between Fe, Ni, and Co, as well as the addition of oxygen vacancies could move down the Fermi level and reduce the adsorption energy of intermediates, thus facilitating OER kinetics.

7. 2D MOF-Based Composites for Electrocatalytic Water Splitting

Integrating pristine MOF with other active species or conductive materials to form composites is regarded as a promising strategy to enhance their intrinsic electrocatalytic performance.

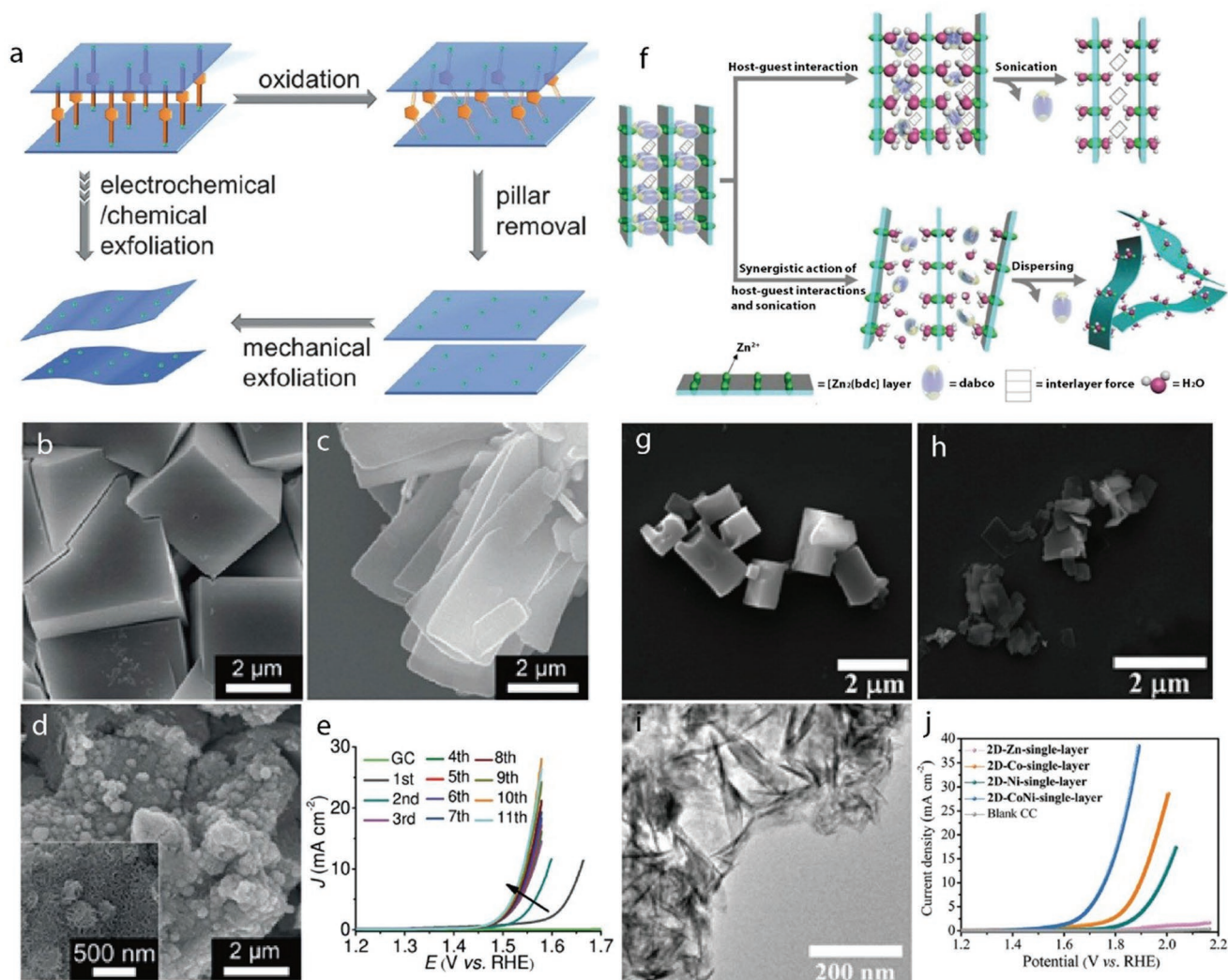


Figure 16. a) Illustration of the synthesis of 2D MOF nanosheets by using the electrochemical/chemical exfoliation method. SEM images of b) 3D-Co, c) 2D-Co, and d) 2D-Co-NS. e) Consecutive LSV of 3D-Co for OER in 0.1 M KOH solution. a–e) Reproduced with permission.^[154] Copyright 2018, Wiley-VCH. f) Schematic of the proposed mechanisms for the transformation of 3D pillared-layer MOFs to ultrathin 2D MOF nanosheets. SEM images of g) 3D-Zn, h) 2D-Zn-few-layer. i) TEM image of the 2D-Zn-single-layer. j) LSV polarization curves of 2D Zn/Co/Ni/CoNi-single-layer and blank CC in 0.2 M PB electrolyte. f–j) Reproduced with permission.^[155] Copyright 2020, Royal Society of Chemistry.

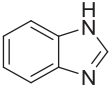
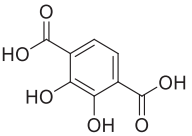
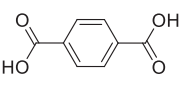
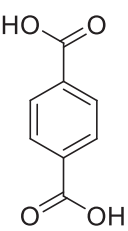
2D MOF-based hybrid materials not only take advantages of individual components, but also possess unique synergistic effects to accelerate catalytic processes.^[158] According to the dimension of extrinsic functional materials, the powdery 2D MOF composites can be mainly divided into three types, including 2D MOF/0D, 2D MOF/1D, and 2D MOF/2D. 0D materials, such as nanoparticles with small sizes and high surface energy, possess unique merits of stability and chemical activity.^[159] Combining the superiority of 0D nanomaterials and 2D MOF can improve the inherent functionality of hybrid materials. Integration of 2D MOF with 1D conductive materials, such as carbon nanotubes, to form multiphase composites, allows for efficient charge transfer across the interfaces due to the intimate contact, which is conducive to the enhancement of OER/HER activity.^[160] 2D materials, such as LDHs and transition metal carbides and nitrides (MXenes) have been investigated to build 2D MOF composites, owing to their large

specific surface areas, electrical conductivity, and confinement effects. The prominent properties of 2D MOF/2D composites, such as favorable mass transport and more exposed active sites, enable them to exhibit remarkable electrocatalytic performance.^[136] The performance of representative 2D MOF composites for water splitting are summarized in **Table 3**.

7.1. 2D MOF/0D Composites

Noble metal nanomaterials are generally believed to possess outstanding catalytic activities for many reactions.^[161] In order to precisely control over their sizes and shapes, conventional wet chemistry methods usually rely on the use of surface capping agents, whose removal requires subsequent heat treatments to expose the active sites of metal nanomaterials.^[162,163] Motivated by the unique characteristics of 2D MOFs, it is highly

Table 3. Electrocatalytic OER and HER performance of 2D MOF-based composites.

Ligand structure	Catalysts	Electrolyte	OER		HER		Active sites	Refs.
			Overpotential [mV]	Tafel slope [mV dec ⁻¹]	Overpotential [mV]	Tafel slope [mV dec ⁻¹]		
	Ni-MOF@Pt	0.5 M H ₂ SO ₄ 1.0 M KOH	–	–	η_{10} : 43 η_{10} : 102	30 88	Pt–O species	[166]
	Pt-NC/Ni-MOF	1.0 M KOH	η_{10} : 292	N/A	η_{10} : 25	42.1	Ni–O–Pt interfacial	[130]
	Ag@Co-MOF	1.0 M KOH	η_{10} : 344	N/A	–	–	Co sites	[167]
	Fe ₃ O ₄ /Ni-BDC	1.0 M KOH	η_{10} : 295	47.8	–	–	Fe species	[169]
	FeNi ₃ -Fe ₃ O ₄ /MOF-CNT	1.0 M KOH	η_{10} : 234	37	η_{10} : 108	96.75	Ni centers, FeNi ₃ , and Fe ₃ O ₄	[171]
	Ti ₃ C ₂ T _x -CoBDC	0.1 M KOH	η_{10} : 410	48.2	–	–	Co-based species	[179]
	GMOF	0.5 M H ₂ SO ₄	–	–	η_{10} : 530	68	MOF and GO	[176]
	Co-BDC/MoS ₂	1.0 M KOH	–	–	η_{10} : 248	86	Co sites, 1T-MoS ₂	[184]
	Ni-BDC/Ni(OH) ₂	1.0 M KOH	η_{10} : 320	41	–	–	High valence Ni	[186]
	NiFe-LDHs/CLs	1.0 M KOH	$\eta_{0.2}$: 364	89	–	–	High valence Ni species	[193]
	CoFeO _x -Co-MOF	1.0 M KOH	η_{10} : 232	32	–	–	High-valent Co sites	[168]
	ZIF-9(III)/Co LDH	1.0 M KOH	η_{10} : 297	65	–	–	Co sites	[192]
	CoCu-ZIF@GDY	1.0 M KOH	η_{10} : 250	57	η_{10} : 446.5	88	Co and Cu species	[170]
	MCCF/ NiMn-MOFs	1.0 M KOH	η_{10} : 280	86	–	–	Ni centers	[172]
	NiFe-BTC-GNPs	1.0 M KOH	η_{10} : 220	51	–	–	Fe and Ni sites	[175]
	Fe(OH) ₃ @ Co-MOF-74	1.0 M KOH	η_{10} : 292	44	–	–	Fe and Ni centers	[187]

CNT: carbon nanotube; GDY: graphdiyne; MCCF: multichannel carbon fibers; GO: graphene oxide ZIF: zeolitic imidazolate frameworks; GNPs: graphene-nanoplatelets; LDH: layered double hydroxide; BTC: 1,3,5-benzenetricarboxylic acid; BDC: 1,4-benzenedicarboxylic acid.

desired to hybridize noble metals and 2D MOFs into heterostructures to optimize the coordination environment and electronic structures for improved electrocatalysts. In addition, high dispersion of noble metals in MOFs would improve their utilization efficiency.

Pt is a benchmark electrocatalyst for HER under both acidic and base conditions. However, Pt has a sluggish kinetic of water dissociation in alkaline media due to its inherent weak OH* adsorption ability, thereby leading to relatively poor HER performance.^[164,165] Recently, Sun's group reported an efficient

in situ reduction strategy to boost HER activity by constructing noble metal/2D MOF heterostructures (**Figure 17a**).^[166] The abundant O atoms on the surface of Ni-MOF (ligand: H₂BDC) provide uniformly distributed anchoring sites. As exhibited in **Figure 17b**, Pt nanoparticles with a diameter of 3 nm are evenly embedded on the surface of Ni-MOF nanosheets via in situ reduction of chloroplatinic acid in ethanol. According to XPS and XAFS characterizations, the coordination environment of Pt was regulated by neighboring O atoms, sequentially optimizing hydrogen adsorption energy. When Ni-MOF@Pt hybrid

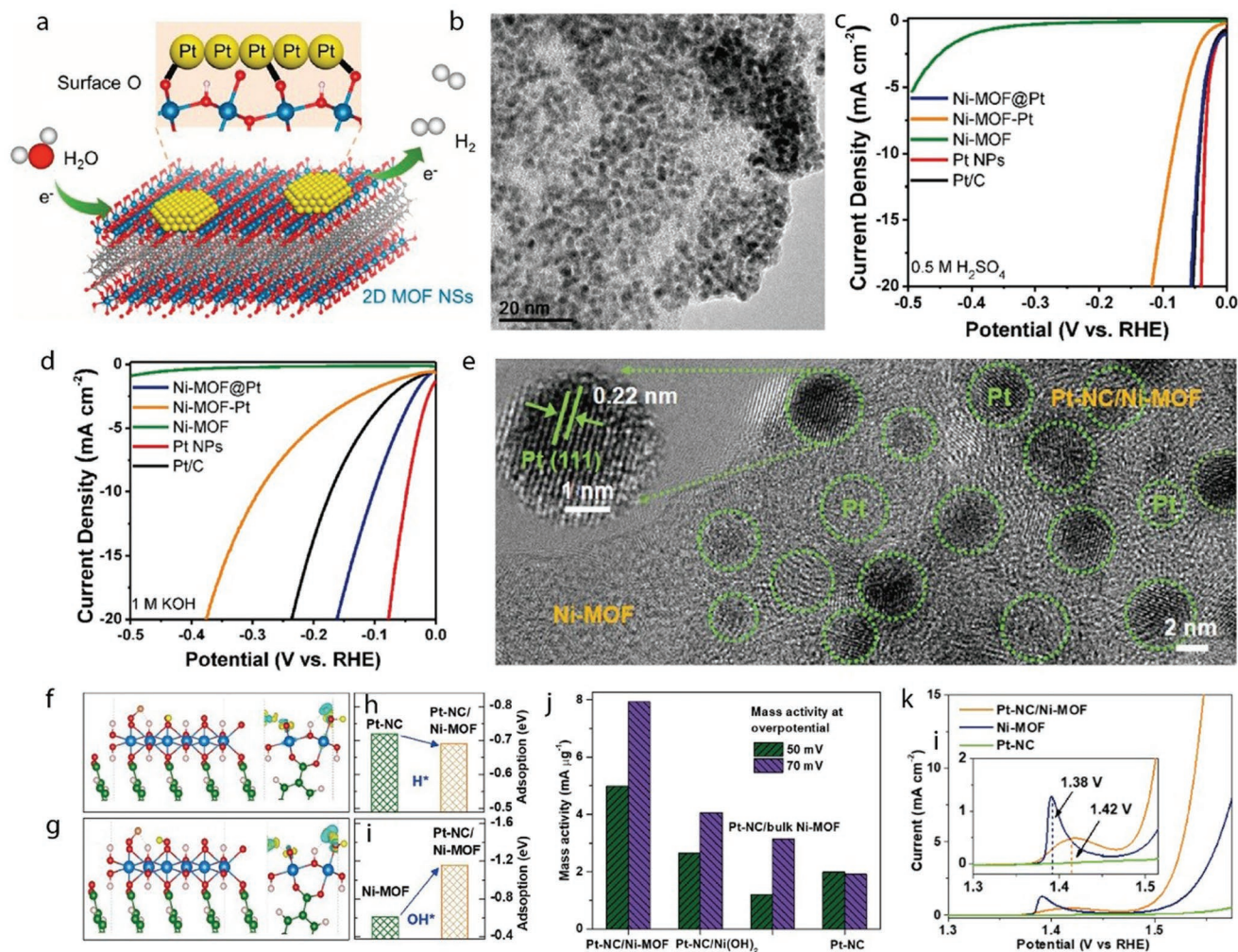


Figure 17. a) Schematic illustration of 2D MOF@Pt heterostructure for HER. b) TEM image of 2D MOF@Pt hybrid. Polarization curves of Ni-MOF@Pt, Ni-MOF-Pt, Ni-MOF nanosheets, Pt nanoparticles, and commercial 10% Pt/C for HER c) in 0.5 M H₂SO₄, and d) in 1.0 M KOH. a–d) Reproduced with permission.^[166] Copyright 2019, American Chemical Society. e) TEM image of Pt-NC/Ni-MOF. The OH* adsorption and charge-difference on f) the individual Ni-MOF structure, and g) the Ni-MOF side of the heterostructure structure. h) H* adsorption energy, and i) OH* adsorption energy comparison of Ni-MOF and Pt-NC/Ni-MOF. j) Mass activity of the as-prepared materials for HER in 1.0 M KOH. k) LSV curves of Pt-NC/Ni-MOF, Ni-MOF, and Pt-NC toward OER in 1.0 M KOH. Inset: a local enlargement of OER curve. e–k) Reproduced with permission.^[130] Copyright 2019, Elsevier.

materials were directly used as HER electrocatalyst in 0.5 M H₂SO₄, they showed a low overpotential of 43 mV to drive a current density of 10 mA cm⁻² (Figure 17c). More importantly, Ni-MOF@Pt also possessed high catalytic activity in 1.0 M KOH, with an overpotential of 102 mV at 10 mA cm⁻² (Figure 17d), which was superior to that of commercial Pt/C (172 mV). The significantly enhanced performance was mainly attributed to the optimized electronic configuration of Pt atoms through the Pt/MOF interfaces. Meanwhile, the affluent Pt–O bonding, the improved electron density and mobility at the interfaces, and the maximal exposure of active sites also contributed to the improvement of HER activity.

Qiao and co-workers used a mechanical mixing strategy to incorporate Pt nanocrystals (Pt-NC) in Ni-MOFs (Pt-NC/Ni-MOF) (ligand: H₂BDC), which simultaneously accelerated HER and OER.^[130] After hybridization, Pt-NCs were homogeneously dispersed on the surface of Ni-MOF nanosheets

(4.3 nm) (Figure 17e). Theoretical calculations predicted that both H* and OH* adsorption strength could be regulated due to the charge relocation on the newly formed Ni–O–Pt bonds (Figure 17f,g). As shown in Figure 17h,i, H* adsorption energy on the Pt side of the heterostructure was slightly weaker than that for Pt-NC, while the adsorption interaction of OH* intermediates on the alternative Ni-MOF side at the interface was strengthened compared to standalone Ni-MOF, which was conducive to the thermodynamics of HER and OER. The formation of a unique interface could promote electron transfer from Ni to Pt through Ni–O–Pt bonds, resulting in the increased electron density for Pt and a higher oxidation state for Ni species. The underpotential deposition of hydrogen of Pt-NC/Ni-MOF indicated weaker H* interaction with Pt-NC/Ni-MOF than Pt-NC, which agreed well with DFT calculations. Meanwhile, the measurement of OH* adsorption using CO stripping suggested a stronger OH* adsorption for Pt-NC/Ni-MOF over

Pt-NC. Therefore, weaker H^{*} adsorption to Pt-NC/Ni-MOF heterostructure promoted hydrogen generation, while stronger OH^{*} adsorption accelerated water dissociation. Notably, Pt-NC/Ni-MOF delivered a significantly mass activity of 792 mA μg⁻¹ Pt at an overpotential of 70 mV (Figure 17j). In addition to the high HER activity, the hybrid also exhibited superior OER performance with an overpotential of 292 mV at 10 mA cm⁻², less than that of Ni-MOF without Pt-NC (360 mV) (Figure 17k). The rational combination of noble metals and 2D MOFs can optimize H^{*} and OH^{*} adsorption for accelerated electrocatalysis.

Nobel metals of Ag have also been composited with 2D MOFs for better catalytic performance. Ag quantum dots (QDs) embedded in the ultrathin 2D Co-MOF (ligand: H₂BDC) nanosheets with a thickness of 0.72 nm were realized through in situ reduction of Ag⁺ ions under ultraviolet radiation.^[167] As suggested by XPS, XAS, and DFT investigations, electrons were transferred from Co sites of MOF to Ag atoms. The modification of Ag QDs mediated the redox potentials of Co sites, thus decreasing the OER overpotential. Ag@Co-MOF exhibited a high TOF of 5.4 s⁻¹ at an overpotential of 0.35 V, which was ≈77 times higher than that of Co-MOF (0.07 s⁻¹). Based on Pourbaix analysis, the decorated Ag QDs would regulate the coupling process between Co sites and OH⁻ ions, which may be responsible for the enhanced OER performance. The postmortem investigations indicated that Ag@Co-MOF was converted to hexagonal structured Co(OH)₂, while the strong Ag–Co bonds were maintained throughout the OER process.

Apart from precious metals, other ultrafine oxide nanoparticles have also been embedded in 2D MOFs to attain highly active interfaces. For instance, CoFeO_x nanoparticles were dispersed on the surface of monolayered Co-MOF (ligand: benzimidazole) nanosheets (M-PCBN) through hydrothermal reactions to tune the electronic configuration of the interfacial Co catalytic sites, thereby prominently enhancing electrocatalytic OER performance.^[168] TEM and PXRD analysis demonstrated that the ultrafine nanoparticles were embedded in the lattice of the monolayered CoN₄-based MOF nanosheets (≈1 nm). XAS confirmed that the metal oxide nanoparticles included both Fe and Co elements, which were expressed as CoFeO_x containing saturated FeO₆ center, unsaturated FeO₅/CoO₅ edge and interfacial CoO₂N₂. It was worth noting that Co atoms connected metal oxide and MOF matrix to form CoFeO_x/MOF heterostructures through Co–O bonds with the metal oxide and Co–N bonds with the MOF matrix. DFT calculations verified that Co atoms in CoN₂O₂ substructure had a higher valence state than the pristine Co in CoN₄ due to the existence of interfaces, as well as the optimal adsorption energy for intermediates, thus facilitating the entire OER pathway. However, Fe moieties of the metal oxide were inactive to OER and pristine CoN₄ sites had poor catalytic activity. In 1.0 M KOH, M-PCBN exhibited a low overpotential of 232 mV at 10 mA cm⁻², better than that of other as-prepared samples. After 1000 CV cycles, the initial morphology and crystal structure were maintained, indicating the excellent stability under electrochemical test condition. Co and Fe valence states in M-PCBN kept unchanged after the reaction, further manifesting the good stability. Combining theoretical and experimental results, the high valence Co active sites and the modified 3d electronic configurations of the interfacial metal oxide, along with ultrathin MOF nanosheets

with fast reaction kinetics, resulted in the enhanced electrocatalytic activities. Recently, the similar study have been reported by Mølhav's group.^[169] They immobilized functionalized ultrasmall Fe₃O₄ nanoparticles homogeneously on 2D Ni-based MOF nanosheets (Ni-BDC) with thicknesses of 5 ± 1 nm by the sonication process to improve the catalytic robustness and modulate the electronic structure. The optimal Fe₃O₄/Ni-BDC achieved the best OER performance with an overpotential of 295 mV at 10 mA cm⁻², a Tafel slope of 47.8 mV dec⁻¹, and excellent durability. DFT calculations identified that the active sites were mainly contributed by Fe species with a higher oxidation state.

7.2. 2D MOF/1D Composites

To improve the catalytic ability of 2D MOFs, numerous MOF/carbon-based functional materials have been successfully assembled. 2D MOFs are well dispersed in the composites with enhanced electrical conductivity and stability. For instance, Fang's group reported a hierarchical 2D/1D nanostructure comprising ultrathin CoCu-ZIF nanosheets with a thickness of 2 nm and graphdiyne nanowires (CoCu-ZIF@GDY) (Figure 18a).^[170] These hybrids inherited the merits of high conductivity and large number of exposed active sites, thus the reaction kinetics were improved. The composites delivered a low overpotential of 290 mV at 10 mA cm⁻² with long-term stability for water splitting (Figure 18b). After the water electrolysis, the chemical structures of CoCu-ZIF@GDY were well retained with some pores or cracks appearing on the surface. Therefore, the intrinsically superior activity, the porous structure and the synergistic interaction between Co and Cu species endowed the composite with outstanding electrocatalytic performance.

Lately, Yang and co-workers uniformly loaded FeNi₃-Fe₃O₄ heterogeneous nanoparticles onto MOF (ligand: H₂BDC) nanosheets and carbon nanotubes matrices (FeNi₃-Fe₃O₄/MOF-CNT) via a simple hydrothermal reaction.^[171] The heterogeneous interfaces would regulate the electronic properties and avoid the aggregation of active sites. In addition, Fe₃O₄-rich CNT support could transfer electrons to metallic FeNi₃ to improve stability. The obtained FeNi₃-Fe₃O₄/MOF-CNT displayed superior performance in overall water splitting with an overpotential of 360 mV to reach 10 mA cm⁻², far surpassing counterparts without CNT matrix. After 20 h of durability test, FeNi₃-Fe₃O₄/MOF-CNT showed an almost similar nanosheet morphology to that before the electrolysis, signifying the robust structure. The remarkable HER activity was ascribed to the decoration of FeNi₃ and Fe₃O₄ heterogeneous particles on the CNT network. During OER process, Ni centers were considered as the active species, and the presence of Fe₃O₄ particles altered the electronic states of Ni metal, thereby making it more electrophilic to attract intermediates. In the same year, Lou's group synthesized hierarchical NiMn-MOF (ligand: 2,6-naphthalenedicarboxylic acid) nanosheets on multichannel carbon fiber (MCCF/NiMn-MOFs) through a simple hydrothermal and subsequent ligand exchange approach (Figure 18c).^[172] As can be seen from Figure 18d–f, NiMn-MOF nanosheets with a thickness of 40 nm densely stand on the surface of MCCF. The highly conductive MCCF support and NiMn-MOF nanosheets

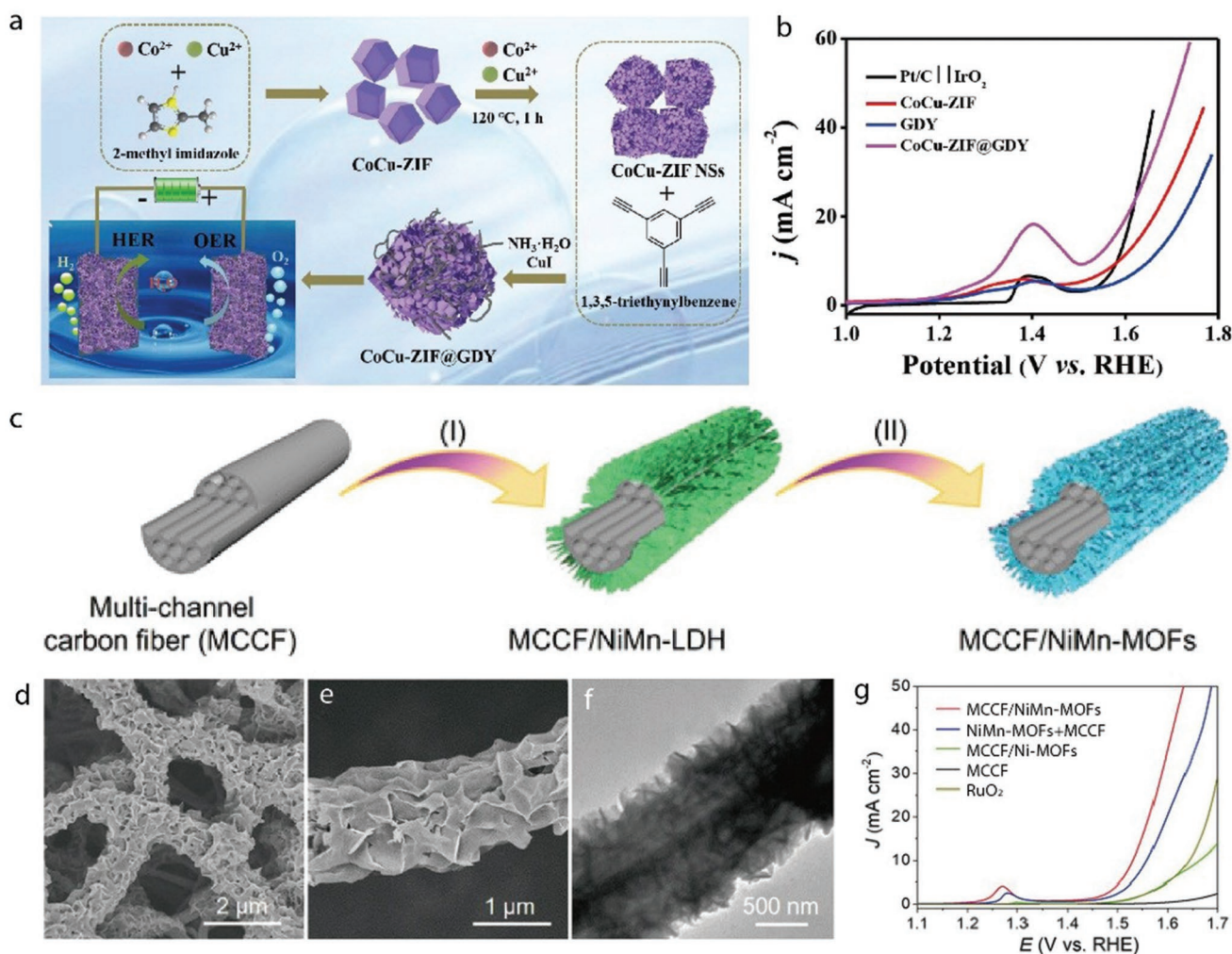


Figure 18. a) Fabrication Process of CoCu-ZIF@GDY for overall water splitting. b) Polarization curves of CoCu-ZIF, GDY, and CoCu-ZIF@GDY as both the cathode and the anode in two-electrode electrolyzers. a,b) Reproduced with permission.^[170] Copyright 2020, Elsevier. c) Schematic diagram of the preparation of MCCF/NiMnMOFs. d,e) SEM and f) TEM images of MCCF/NiMn-MOFs. g) Polarization curves of MCCF/NiMn-MOFs and other contrast catalysts. c–g) Reproduced with permission.^[172] Copyright 2020, Wiley-VCH.

ensured fast charge transport and robust stability. Meanwhile, the strong interaction between Ni and Mn nodes was identified by XAFS and XPS characterizations. As presented in Figure 18g, MCCF/NiMn-MOFs exhibited a low overpotential of 280 mV at 10 mA cm^{-2} for OER, much superior to MCCF/Ni-MOFs (430 mV), NiMn-MOFs + MCCF (320 mV), and RuO₂ (410 mV). According to DFT calculations, Ni centers served as the real active sites and the synergetic effect of neighboring Ni and Mn atoms could promote the thermodynamic generation of key *O and *OOH intermediates during OER reaction.

7.3. 2D MOF/2D Composites

Combining 2D MOF with various 2D components, such as graphene oxide (GO), LDH, and MXene, is anticipated to accelerate the electrocatalytic activities.^[173] The formation of heterostructures through interface engineering can provide the enhanced density of active centers and promote charge transfer.

Graphene is a nanosheet composed of hexagonal carbon atomic rings with good flexibility and ultrahigh intrinsic carrier mobility, and has been widely exploited in the realm of energy conversion and storage.^[174,175] Particularly, their satisfactory tolerance to harsh environment and adjustable surface physicochemical properties has by far ignited the interest to construct MOF/GO composites as high efficient electrocatalyst. As an example, Sun and co-workers developed an epitaxial growth strategy to grow an insulating 2D $\text{Cu}_6(\text{C}_8\text{H}_4\text{O}_4)_6(\text{H}_2\text{O})_6 \cdot \text{H}_3[\text{P}(\text{W}_3\text{O}_{10})_4]$ MOF (ligand: H₂BDC) on the surface of pristine GO surface (Figure 19a).^[176] The epitaxial grown 2D single-crystal MOF possessed highly oriented and large aspect ratios (≈ 1500). Importantly, this epitaxial method could also be applied to other 2D substrates. The strong electrical coupling between MOF and GO resulted in significantly enhanced HER catalytic activity with a low overpotential of 0.53 V at 30 mA cm^{-2} . After a 4 h endurance test, the MOF maintained the initial crystalline characteristics. This electrochemical performance enhancement arose from the integrated

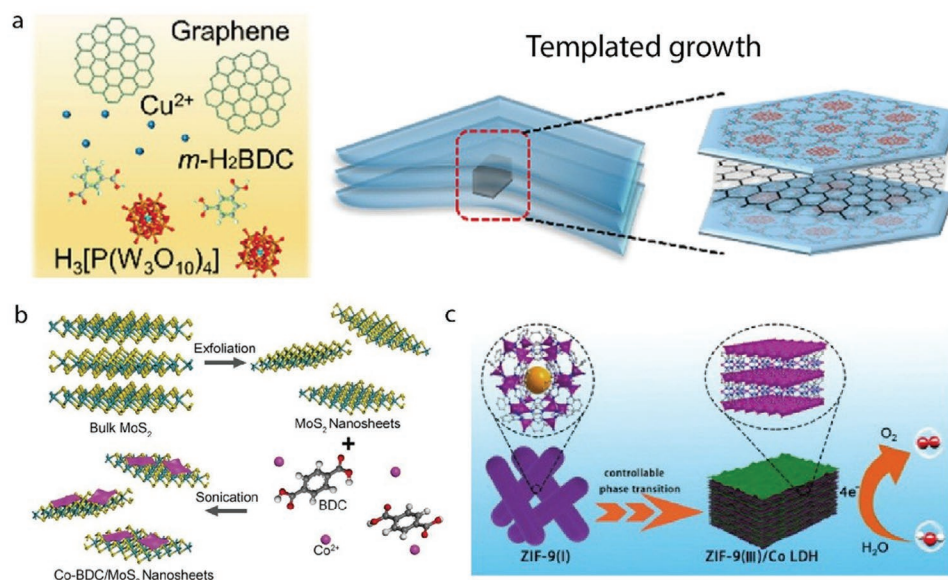


Figure 19. a) Epitaxial growth of pristine-graphene-templated MOF (GMOF). a) Reproduced with permission.^[176] Copyright 2019, American Chemical Society. b) Schematic of the synthesis process for Co-BDC/MoS₂ composite. b) Reproduced with permission.^[184] Copyright 2019, Wiley-VCH. c) The fabrication routes of ZIF-9(III)/Co LDH and used as OER catalysts. c) Reproduced with permission.^[192] Copyright 2021, Elsevier.

MOF-based architecture, rather than the molecular fragments. In 2020, NiFe bimetallic MOFs on the support of graphene-nanoplatelets (NiFe-BTC-GNPs) were prepared by Kim's group.^[175] NiFe-BTC-GNPs displayed excellent OER activity with a low overpotential of 220 mV at 10 mA cm⁻² and a high TOF of 1.22 s⁻¹ in 1.0 M KOH. Besides, it also possessed superior intrinsic activity and durability. The high electrical conductivity of GNPs and the favorable interfaces facilitated fast electron transfer and gas bubble dissipation, thus leading to the improved performance. The structural characterizations after stability test confirmed the integrity of structure and morphology. DFT calculations further indicated the theoretical overpotential of NiFe-BTC was 239 mV at Fe site, which was lower than that of Ni site.

MXenes are an emerging group of 2D materials with high electrical conductivity (6000–8000 S cm⁻¹), surface hydrophilicity, and good stability.^[177] Due to the low work function and electronegative surface, MXenes can serve as conductive supports to tune the electrophilicity of catalytic site in multicomponent electrocatalyst.^[178] In the work reported by Huang and co-workers, in situ hybridized 2D CoBDC MOF with Ti₃C₂T_x nanosheets via an interdiffusion reaction-assisted process.^[179] Through this approach, CoBDC could be seamlessly coated on the surfaces of Ti₃C₂T_x nanosheets. The composite showed superior OER catalytic activity with a potential of 1.64 V at 10 mA cm⁻² in 0.1 M KOH. Importantly, Ti₃C₂T_x-CoBDC catalyst also demonstrated more favorable reaction kinetics, which was verified by the smaller Tafel slope (48.2 mV dec⁻¹) compared with CoBDC (48.8 mV dec⁻¹) and Ti₃C₂T_x (187.1 mV dec⁻¹). This phenomenon was attributed to the synergistic coupling effects, allowing for the fast charge and ion transfer. The 2D porous CoBDC with large specific surface area provided active species, as well as the hydrophilic Ti₃C₂T_x prevents the aggregation of CoBDC layers and promoted the contact between the electrolyte and the catalyst surface.

Except for conductive materials, some electrocatalytically active materials, such as metal sulfides and transition metal hydroxide, are widely used to fabricate MOF-based composites.^[180,181] The synergistic interaction between the additional species and 2D MOF may lead to further enhancement of catalytic properties. The poor HER performances of MoS₂ in basic environment stem from the improper hydroxyl adsorption.^[182] Introducing water dissociation promoters is regarded as an efficient approach to accelerate the alkaline HER process of MoS₂.^[183] For instance, Qiao and co-workers designed a novel 2D Co-BDC/MoS₂ hybrid nanocomposite by a facile sonication-assisted solution method (Figure 19b), which was used as efficient HER electrocatalyst.^[184] The introduction of Co-BDC induced the partial transformation of MoS₂ from the semiconducting 2H phase to the metallic 1T phase. 1T-MoS₂ could activate the inert basal plane to offer more reaction sites, thereby significantly increasing HER efficiency. Importantly, the constructed Co-BDC/MoS₂ interface was vital for alkaline HER, whereby Co-BDC could facilitate the sluggish water dissociation, and the modified MoS₂ acted as catalytic centers for the generation and desorption of H₂. Co-BDC/MoS₂ delivered an overpotential of 248 mV at 10 mA cm⁻², lower than those of Co-BDC (529 mV) and MoS₂ (349 mV). The Tafel slope of Co-BDC and MoS₂ was 111 and 109 mV dec⁻¹, while that of Co-BDC/MoS₂ was decreased to 86 mV dec⁻¹. After the cycling test, nanosheet morphology and XRD pattern of Co-BDC/MoS₂ were well maintained, substantiating the stable structure.

Transition metal hydroxides have abundant octahedral MO₆ structure and high stability, which are in favor of water oxidation.^[185] Qiao's group synthesized a 2D Ni-BDC/Ni(OH)₂ hybrid system, restricting the aggregation of MOF nanosheets.^[186] Of note, the strong interfacial effect between Ni atom in Ni(OH)₂ and neighboring BDC²⁻ in Ni-BDC could reduce the electron density around the Ni atom, resulting in the formation of Ni cations with higher oxidation states. In addition, the distinct

nanosheet possessed more coordinatively unsaturated metal atoms and rapid mass transport ability, which greatly contributed to increase the intrinsic OER activity. Specifically, the current density of Ni-BDC/Ni(OH)₂ at 1.6 V is 82.5 mA cm⁻², much higher than those of Ni-BDC (5.5 times), Ni(OH)₂ (20.6 times), and Ir/C (3.0 times). The morphology of hybrid nanosheet was not destroyed after endurance test, demonstrating the excellent stability. The strategy of this work can be readily adapted for the preparation of other 2D MOF-based hybrid catalysts. Luo and co-workers reported a stable Fe(OH)₃@Co-MOF-74 (ligand: 2,5-dihydroxyterephthalic acid) heterostructure fabricated by fast “phenol-Fe” MOF surface reaction.^[187] The introduction of Fe(OH)₃ nanosheet on Co-MOF-74 surface regulated the electronic state of Co center, and thus generating strong electronic interaction between Co and Fe, which was beneficial to speed up the OER reaction. The mass activity (7894.4 A g⁻¹) and TOF value (1.209 s⁻¹) of Fe(OH)₃@Co-MOF-74 were more than 25 times higher than those of Co-MOF-74. The chronoamperometric curves measured at the constant overpotential of 331 mV displayed 9.2% current density loss during 20 h, indicating the ameliorated stability after the decoration of Fe(OH)₃. SEM, XRD, and XPS characterizations indicated that the morphology, crystalline phase, and valence state remained unchanged after a long-term test.

Layered double-metal hydroxides (LDHs) possess a flexible brucite-like layered structure, tunable compositions, and advanced physicochemical properties, which have also attracted intensive interest in the realms of electrocatalysis.^[188] Notably, the reciprocal transformation between MOF and LDH is regarded as a feasible method to fabricate MOF/hydroxide or oxyhydroxide hybrid materials. The formation of heterostructures can create a highly active surface/interface between two different phases, thereby regulating the chemical environment around the metal centers. The 3d electronic structure adjustment of metal atom can optimize the intermediate energy and enhance the intrinsic electrochemical activity.^[189–191] Therefore, the precisely controlled semitransformation between MOF and LDH is critical for the construction of MOF/LDH composites. In this regard, Cai and co-workers proposed a controllable phase transition approach to fabricate 2D ZIF-9(III)/Co LDH (ligand: benzimidazole) nanocomposites (Figure 19c).^[192] During the chemical transformation process, the volume ratio of water/ethanol played an imperative role in controlling the components of the final products. Beneficial from the rich redox reaction sites, the improved structure stability, and reaction kinetics, ZIF-9(III)/Co LDH-15 nanosheet (3.4 nm) displayed high efficiency OER performance with a low overpotential of 297 mV at 10 mA cm⁻², a low Tafel slope (65 mV dec⁻¹), and superior electrochemical stability. The contribution of the interface in composite was also explained by DFT calculations, the rate-limiting step free energy of ZIF-9 (III)/Co LDH (2.19 eV) was obviously lower than that of ZIF-9(III) (3.3 eV) and Co LDH (2.56 eV). After OER test, ZIF-9(III)/Co LDH-15 partly maintained the framework structure. Recently, Li's group elucidated the extraordinary role of surface-adsorbed H₂BDC carboxylate ligands (CLs) on LDHs/MOFs by measuring the OER catalytic performance of LDH with and without CLs.^[193] Compared with NiFe-LDHs (423 mV), NiFe-LDHs/CLs show a smaller overpotential of 364 mV at 0.2 mA cm⁻². Similarly,

other various bimetallic LDHs also exhibited obvious improvement of catalytic activity and reaction kinetics after adding CLs to the alkaline electrolyte. DFT calculations revealed that the enhanced electrocatalytic performance originated from the electron redistribution at the interface of LDH/CLs, thereby optimizing the binding strength of intermediates. The results of XPS and XAS further validated that the local coordinated CLs could regulate the electronic configuration and facilitate the formation of partially distorted structure.

In recent years, as another typical porous materials, covalent-organic frameworks (COFs) have been arousing increasing attention due to the unique π -conjugation structures and outstanding functionalities.^[194] Combining various types of MOFs and COFs can efficiently unify the advantages of each component, affording the generated MOF/COF heterostructures wide applications in diverse fields.^[195] Therefore, 2D MOF/COF hybrids with favorable structure and high active site density display great potential applications when employed as electrocatalysts in the fields of water splitting.

8. Self-Supported 2D MOF for Electrocatalytic Water Splitting

Although remarkable accomplishment has been achieved in the water electrolysis using powdery 2D MOFs, the usage of polymeric binders in the working electrodes not only impedes the charge transfer and blocks active sites, but also brings up the problem of the catalyst easily being peeled off from the substrate during long-term or large current density test.^[196] Instead of using binders, 2D MOF can be directly grown on conductive substrates, such as metal (Ni, NiFe, Cu) foams, metal (Ti/Cu) foils, and carbon fiber cloth or paper. Compared with the conventional powdered electrode, the rational design of self-supported electrode is able to enhance HER and OER performance based on the following advantages. i) The seamless catalyst–substrate interfacial contact promotes the rapid charge transport and prevents the catalyst delamination.^[197] ii) Nanoarray architectures are beneficial to the exposure of active sites and the improvement of atom utilization efficiency.^[198] iii) MOF/support composites with complex hierarchical structures can expedite the release of accumulated gas bubbles and enhance the catalytic performance and durability for practical high current density electrolysis.^[199] The summary of recent 2D MOF/support electrocatalysts from the aspects of different organic ligands, electrocatalytic performance, and active sites are listed in **Table 4**.

So far, the controlled growth of MOFs on different substrate surfaces, especially chemically inert surfaces, remains a challenge because there are limited number of nucleation sites.^[200] During the synthesis, surface defects, selected organic functional groups or metal layers on the surfaces provide accessible sites to allow the nucleation and conformal growth of MOFs. In a previous work, we have systematically investigated the growth of MOF nanoarrays on various substrates, such as Ni foam, Si or glass slides.^[106] It was found that the growth of MOF nanoarrays was successful on Ni foam, but not on Si or glass slides. When the Si or glass surface was modified with –COOH or –NH₂ functional groups using silane chemistry, MOF growth did not occur either. When a thermally evaporated metal (e.g.,

Table 4. Summary of 2D MOF nanoarrays for OER and HER.

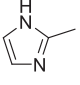
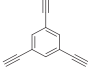
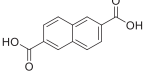
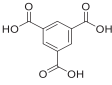
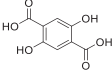
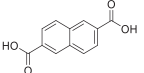
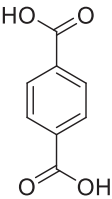
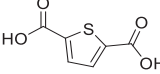
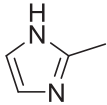
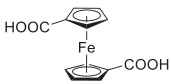
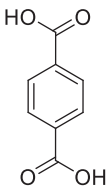
Ligand structure	Catalysts	Substrates	Electrolyte	Overpotential [mV]	Tafel slope [mV dec ⁻¹]	Active sites	Refs.
OER							
	NiFe-MOF	NF	0.1 M KOH	η_{200} : 210	68	Ni ⁴⁺ species	[206]
	MIL-53(Co-Fe)	NF	1.0 M KOH	η_{100} : 262	69	Fe cations	[207]
	MIL-53(FeNi)	NF	1.0 M KOH	η_{50} : 233	31.3	Fe and Ni centers, exposed carboxylate group	[208]
	FeCoNi-MOF	NF	1.0 M KOH	η_{100} : 225	29.5	Unsaturated Fe, Co, and Ni sites	[209]
	Co/Ni(BDC) ₂ TED	CF	1.0 M KOH	η_{50} : 287	76.24	Co and Ni atoms	[210]
	CoNi-MOF	CoNi alloy foam	1.0 M KOH	η_{10} : 215	51.6	Initial: CoO ₅ and NiO ₅ units after OER: oxyhydroxide with oxygen vacancy	[212]
	NiCo-BDC	NF	1.0 M KOH	η_{10} : 230	61	(Oxy)hydroxide	[213]
	FeNi-BDC	NF	1.0 M KOH	η_{50} : 243	69.8	(Oxy)hydroxide	[214]
	MIL-53(NiFe)	NiFe alloy foam	1.0 M KOH	η_{10} : 227	38.9	Oxides or (oxy)hydroxides	[215]
	NiFe-MOF	NF	1.0 M KOH	η_{10} : 200	51.3	Fe and Ni(OH) ₂ species	[216]
	CoBDC-Fc	NF	1.0 M KOH	η_{10} : 178	51	Unsaturated Co ²⁺ centers	[218]
	NiFeCP	NF	1.0 M KOH	η_{10} : 188	29	High valence Fe and Ni, uncoordinated carboxylate group	[219]
	NiCoFe-MOF	GP	1.0 M KOH	η_{10} : 257	41.3	Metal hydroxide and oxyhydroxide	[105]
	Ce-NiBDC	OG	1.0 M KOH	η_{10} : 265	46	Ce-NiOOH	[220]
	FeNi-MOF	NF	1.0 M KOH	η_{50} : 239	52.4	Fe and Ni sites	[102]
	Co-MOF	NF	1.0 M KOH	η_{10} : 270	75	CoOOH	[106]
	ZIF-67/CoNiAl-LDH	NF	1.0 M KOH	η_{10} : 303	88	Ni ³⁺ and Co ³⁺ active interfaces	[95]
	NiFeCo-ZIF	NF	1.0 M KOH	η_{100} : 216	23.25	Ni centers	[96]
	NiFc-MOF	NF	1.0 M KOH	η_{10} : 195	44.1	Ni sites	[100]
HER							
	NiRu-MOF	NF	1.0 M KOH	η_{100} : 156	90	Ni and Ru atoms	[90]
	NiRu _{0.13} -BDC	NF	1.0 M KOH 1.0 M PBS	η_{10} : 34 η_{10} : 36	32 32	Ni and Ru sites	[38]
Water splitting							
	NH ₂ -MIL-88B(Fe ₂ Ni)	NF	1.0 M KOH	OER: η_{10} : 240 HER: η_{10} : 87	58.8 35.2	Unsaturated Fe and Ni centers; M/MO ₆ clusters and -NH ₂ groups	[92]
	MFN-MOFs	NF	1.0 M KOH	OER: η_{50} : 235 HER: η_{10} : 79	55.4 30.1	Fe and Ni atoms; Fe and Ni atoms, -NH ₂ groups	[222]
	NiCo-9AC-AD	NF	1.0 M KOH	OER: η_{100} : 350 HER: η_{10} : 143	51.3 37.1	Co and Ni sites	[223]

Table 4. Continued.

Ligand structure	Catalysts	Substrates	Electrolyte	Overpotential [mV]	Tafel slope [mV dec ⁻¹]	Active sites	Refs.
	D-Ni-MOF	Ni foil	1.0 M KOH	OER: η_{10} : 219 HER: η_{10} : 101	48.2 50.9	O vacancies and high valence Ni	[224]
	NiFe-MS/MOF	NF	1.0 M KOH	OER: η_{50} : 230 HER: η_{50} : 156	32 82	Oxyhydroxides; metal hydroxide	[71]
	NiFe-MOF	NF	0.1 M KOH	OER: η_{10} : 240 HER: η_{10} : 134	34 N/A	NiO ₆ /NiOOH; Ni/NiO ₆ interface	[99]
	CoFe-PBA	NF	1.0 M KOH	OER: η_{10} : 256 HER: η_{10} : 48	54 66	Metal (oxy)hydroxides; Co/Fe hydroxides	[37]

NF: Ni foam; MIL: Materials Institute Lavoisier; CF: Cu foam; OG: graphite foil; GP: graphite paper.

Ni, Co, Ag) layers were deposited on Si or glass slides, MOFs could finally grow on their surfaces. These observations suggest that weak interaction is present between MOFs and bare surfaces of Si or glass slides, while the deposited metal layers provide accessible sites to nucleate and grow MOFs due to strong coordination interactions. Therefore, suitable coating on the desired substrates with enriched nucleation sites are beneficial for the uniform growth of MOFs and the enhancement of the binding forces between MOFs and substrates, which affect the mechanical stability of MOF nanoarrays.

The general method for constructing self-supported MOF materials consists of directly growing on the substrates or on an additional seeding layer on the substrates.^[106] Direct in situ growth of MOFs on conductive carrier is a simple yet efficient approach. The organic linkers or metal ions have strong interactions with the substrate surfaces, which template the growth of firmly rooted MOFs. In this case, the surface coatings derived from native substrates act as the natural seeding layer for MOF attachment. Alternatively, foreign seeding layer is employed to mediate the oriented growth if the native substrate has poor interaction with MOFs. For instance, transition metal oxides/hydroxides, alkylthiols or polyaniline coatings have promoted the growth of the respective MOF arrays with appropriate precursors-surfaces interactions.^[201–203]

The most commonly used organic ligands in recently reported 2D MOF arrays for electrocatalysis are carboxylate ligands.^[16] From the morphological and structural point of view, carboxyl functional group possesses flexible coordination modes and strong coordination ability to form metal carboxylate clusters or bridged linkages, which can increase the stability and rigidity of MOF skeleton.^[94] In addition, carboxylate-coordinated metal atoms display the favorable electronic configurations toward electrocatalytic reaction, including abundant unsaturated metal centers, oxidized octahedral MO₆ structure, as well as the enhanced hydrophilicity and the accessibility of hydroxyl ions due to the exposed carboxyl groups.^[204]

8.1. Self-Supported 2D MOFs for HER

It is important yet challenging to design and prepare effective MOF electrocatalysts toward HER. Noble metal ions substitution can regulate the electronic structure of the active sites in a certain MOF and optimize the adsorption free energy for reaction intermediates. Recently, NiRu-based binary MOF (ligand: H₂BDC) nanosheets (10 nm) were constructed on NF by direct Ru cation doping strategy.^[90] Ni-MOF retained the pristine morphology and crystal structure after the incorporation of the low content Ru, while the electron transport ability and water stability were improved. The NiRu-MOF/NF with a Ru/Ni molar ratio of 6/94 required a low overpotential of 51 mV at -10 mA cm^{-2} , which was lower than those of Ni-MOF/NF (246 mV) and NF (434 mV). Additionally, NiRu-MOF/NF composite was highly stable in 1.0 M KOH solution, as revealed by SEM, TEM, and XPS results. The authors attributed the efficient HER performance to the modified electronic interaction between Ni and Ru atoms, the increased active surface areas, the proper hydrophilic and aerophobic properties.

Due to the conspicuous activity and the maximum atom utilization rates, single-atom catalyst has intrigued new interests in electrocatalysis.^[205] Su and co-workers reported a single-atom approach to alter HER performance of MOF via introducing atomically dispersed Ru atoms (Figure 20a).^[38] Through ion-exchange strategy, Ru single-atom replaced part of Ni atoms in Ni-BDC nanosheet array growing on Ni foam. A series of MOF materials with various Ru loading were obtained by changing the amount of Ru³⁺ ions. The optimal NiRu_{0.13}-BDC displayed prominent HER activity in all pH, especially with the small overpotential of 36 and 34 mV at 10 mA cm^{-2} in 1.0 M PBS and KOH solution, respectively (Figure 20b,c). The crystal structure and chemical environment showed limited changes after the continuous 10 h operation, manifesting the good stability of NiRu_{0.13}-BDC. XPS, EXAFS, and XANES characterizations confirmed the strong electron interaction between Ni and Ru

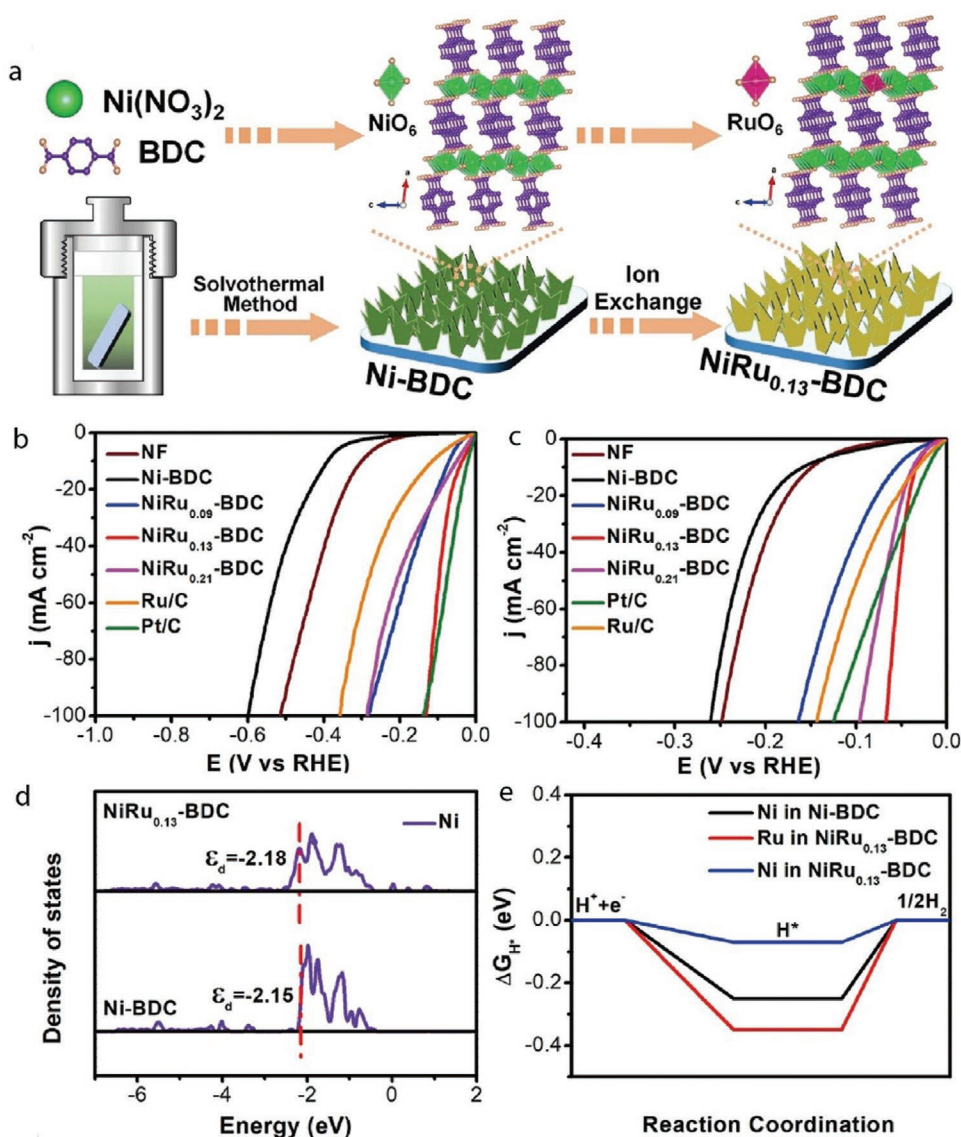


Figure 20. a) Schematic illustration for the synthesis of NiRu_{0.13}-BDC arrays. LSV curves toward HER of various catalysts in b) 1.0 M PBS and c) 1.0 M KOH. d) Simulated DOS of Ni atom in Ni-BDC and NiRu_{0.13}-BDC. e) The calculated adsorption free energy of H* on Ni-BDC and NiRu_{0.13}-BDC. a–e) Reproduced with permission.^[38] Copyright 2021, Springer Nature.

atoms. Furthermore, DFT calculations were conducted to clarify the inherent relationship between the electronic configuration and the improved performance of NiRu_{0.13}-BDC. As shown in Figure 20d,e, the introduced Ru single-atom could optimize the electronic structure and d-band center of metal sites, resulting in the appropriate adsorption strength for H₂O and H*, thus contributing to the improved activity.

8.2. Self-Supported 2D MOFs for OER

Because of the large surface area, high electrical conductivity, and mechanical strength, metal foam has been widely applied microporous support for the growth of MOF arrays.^[6,132] 2D MOF/substrate composites could be prepared via a one-pot hydrothermal/solvothermal process, during which the metal

ions and organic linkers self assemble on the surface of metal skeleton. For example, Liu and co-workers fabricated NiFe-MOF (ligand: 2,6-naphthalenedicarboxylate acid) nanosheets (≈ 20 nm) arrays on Ni foam (NF) through a hydrothermal method and then introduced the lattice strain in the nanosheets by ultraviolet-light treatment.^[206] After ultraviolet irradiation for various times, the lattice fringe spacing of NiFe-MOF was enlarged, while the nanosheet morphology was well retained (Figure 21a). Lattice-strained NiFe-MOFs showed great mass activity ($2000 \text{ A g}_{\text{metal}}^{-1}$) at an overpotential of 0.30 V for OER, which was two orders of magnitude higher than that of pristine NiFe-MOF. The operando synchrotron radiation Fourier transform infrared spectroscopy and XAS techniques demonstrated that the lattice-strained MOF underwent an ideal 4e⁻ pathway during OER process compared to the pristine MOF and the generated high-valence Ni⁴⁺ species adsorbing the

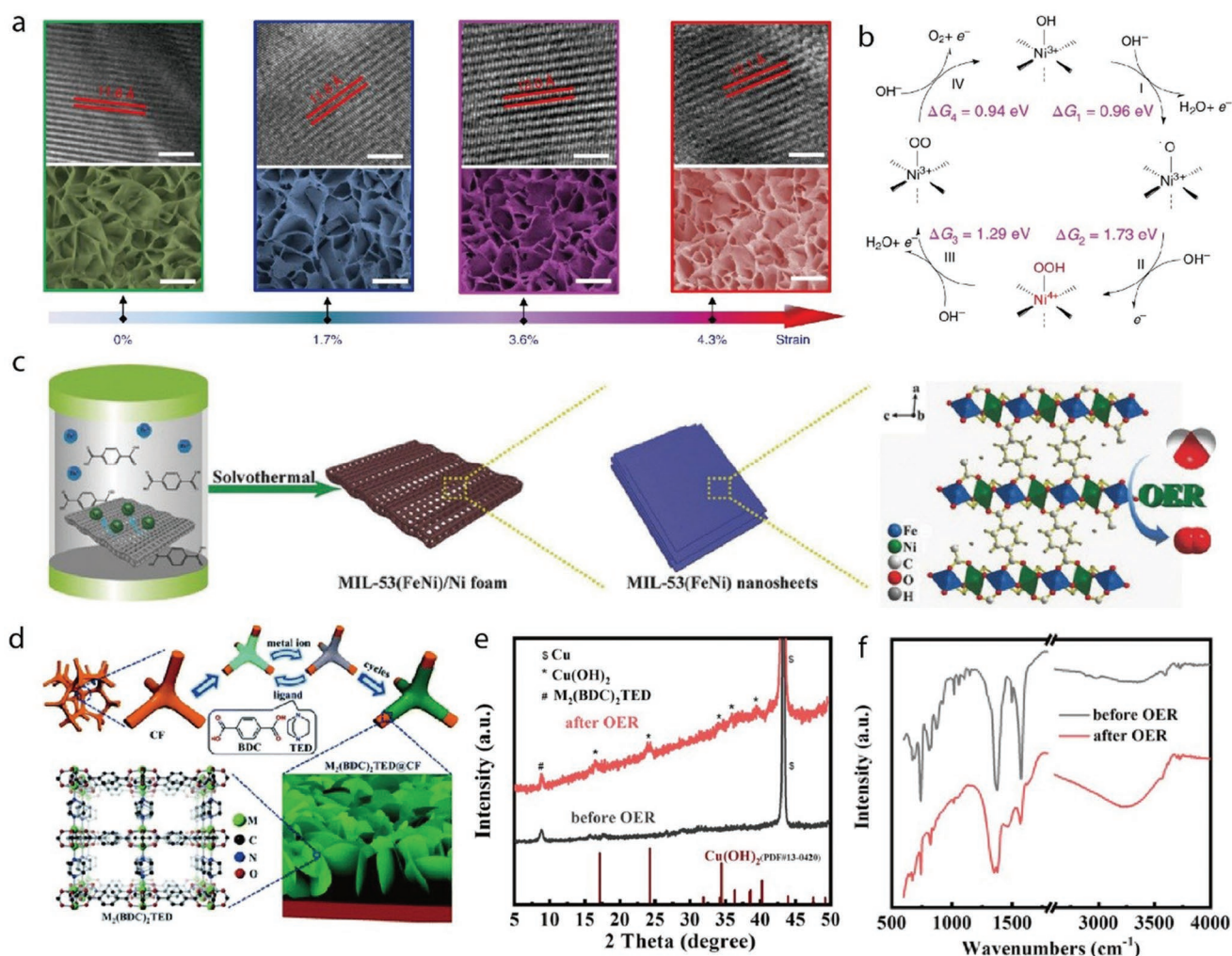


Figure 21. a) HRTEM (top) and SEM (bottom) images of NiFe-MOF after various ultraviolet-treatment times. b) OER catalytic mechanisms for the lattice-strained NiFe-MOFs. a,b) Reproduced with permission.^[206] Copyright 2019, Springer Nature. c) The formation procedure of MIL-53(FeNi)/NF by a solvothermal method. c) Reproduced with permission.^[208] Copyright 2018, Wiley-VCH. d) Illustration of the preparation for $\text{M}_2(\text{BDC})_2\text{TED}$ nanosheet arrays on Cu foam by liquid-phase epitaxial approach. e) XRD and f) IR of $\text{Co/Ni}(\text{BDC})_2\text{TED}@CF$ before and after OER testing. d–f) Reproduced with permission.^[210] Copyright 2019, Royal Society of Chemistry.

key superoxide $^*\text{OOH}$ intermediate was the actual active sites (Figure 21b). The postelectrolysis structural characterization results confirmed the integrity of lattice-strained NiFe-MOF crystal structure and morphology. This work provided a direct evidence for the key reaction intermediates and catalytic sites of NiFe-MOF during OER process. Zeng and co-workers also prepared MIL-53(Co–Fe) (ligand: H_2BDC) nanosheet arrays on NF through a facile solvothermal process.^[207] MIL-53(Co–Fe)/NF displayed remarkable OER activity with the ultralow overpotential of 262 mV to afford a current density of 100 mA cm^{-2} . The morphology and chemical state were unchanged after electrochemical test, indicating the exceptional stability of MIL-53(Co–Fe)/NF. The authors proposed that Fe cations were active sites and Co cations assisted the formation of OER active sites in bimetal Co–Fe MOFs.

Apart from serving as the only supporting materials, NF can also function as a self-sacrificing template to provide metal ions in MOF growth process. Lin and co-workers reported the

preparation of NiFe-based MOF (ligand: H_2BDC) nanosheets (32 nm) on NF (MIL-53(FeNi)/NF) via a one-step solvothermal route (Figure 21c).^[208] During this procedure, the released Ni^{2+} ions from NF together with the exogenously added Fe^{2+} coordinate with H_2BDC ligands. The as-prepared MIL-53(FeNi)/NF displayed superior OER performance compared with MIL-53(Ni)/NF. The enhanced OER activity was relevant to the introduction of Fe ions into MIL-53(Ni), which increased the reaction sites and accelerated electron transport capability. Besides, the authors suggested that the exposed carboxylate groups were beneficial to improve the hydrophilicity and availability of OH^- . According to DFT simulations, MIL-53(FeNi) was more favorable to adsorb foreign atom and increase 3d orbital electron density, thereby boosting intrinsic activity. Importantly, XRD, XPS, and SEM after OER measurement indicated that the MOFs are not transformed into other phases. Recently, Lu's group proposed a maximized-entropy concept to synthesize trimetallic MOF on the skeleton surfaces of NF.^[209]

FeCoNi-MOF/NF (ligand: H₂BDC) with an equimolar metal component possessed maximum synergistic effect toward OER, exhibiting remarkable catalytic activity with an ultralow overpotential of 196 mV at 10 mA cm⁻², as well as excellent stability at the industrially relevant large current density of 1000 mA cm⁻². It was noteworthy that the crystalline structure and the thin nanoslab shape were well-maintained after OER test. Furthermore, the maximized-entropy approach was verified through in situ Raman spectroscopy and DFT calculations. The superior intrinsic activities are ascribed to the uniformly dispersed metal centers, rich coordinatively unsaturated sites, and the close contact between MOF and NF.

Other than Ni foam, Cu foam has also been used as the platform for the growth of MOF nanoarrays by liquid-phase epitaxial layer-by-layer strategy. In the work reported by Zhang and co-workers, bimetallic MOF nanosheet (3–4 nm) arrays with preferential [001] orientation were mounted on Cu foam (Figure 21d).^[210] The OER performance of surface-mounted MOF nanosheet arrays could be optimized by adjusting the preparation cycles and metallic content. Especially, Co/Ni(BDC)₂TED@CF (TED: triethylenediamine) after 40 cycles with an equal ratio of Co/Ni exhibited the highest OER catalytic activity, possessing a small overpotential of 287 mV at 50 mA cm⁻² and long-term stability. Almost unchanged XRD pattern (Figure 21e) and FT-IR spectra (Figure 21f) further indicated the high stability of MOF arrays. However, a few (oxy)hydroxides may be formed on MOF surface, which acted as a protective layer for the interior Co/Ni(BDC)₂TED during long-term measurement. The theoretical computation results demonstrated that Ni sites were much easier to activate at the start of OER, while Co centers were more favorable to the electron transfer and the desorption process. Experiments combined with DFT simulations revealed that the high activity is attributed to the bimetallic synergistic effect and abundant metal nodes.

Despite the array structure of 2D MOFs can improve the electrochemical stability, the applied voltage bias and testing environment (e.g., pH, electrolyte ions) may also induce the partial topological changes of MOFs in terms of roughness, porosity, or components.^[211] The partial structural reconstruction is accompanied with the regulation of intrinsic electrocatalytic properties of MOFs, such as adsorption, activation, and desorption of intermediates, which in turn reflect the corresponding HER or OER performance.^[98] In 2019, Dong's group developed a universal self-dissociation-assembly strategy to prepare ultrathin bimetal CoNi-MOF nanosheet (8.2 nm) arrays on CoNi alloy foam.^[212] During the hydrothermal reaction, CoNi alloy foam was tardily oxidized and dissociated into Co²⁺ and Ni²⁺ ions, which simultaneously coordinated and assembled with BDC. Each Co/Ni atom was octahedrally coordinated by six O atoms, coming from carboxylate linkers and hydroxyls. Co₉Ni₁-MOF possessed an extremely low overpotential of 215 mV at 10 mA cm⁻², and maintained more than 300 h of continuous OER operation. With the assistance of multiple spectroscopic technologies and DFT calculations, the structural evolution of Co₉Ni₁-MOF during OER process was revealed. These characteristics demonstrated that the coordinatively unsaturated CoO₅ and NiO₅ units together with the synergistic effect endowed Co₉Ni₁-MOF with superior inherent activity at the initial stage of electrochemical OER, while Ni atoms were

more active sites (Figure 22a). After long-term cycling, the partially dissolved linkers and the potential oxidation resulted in the formation of ultrafine oxyhydroxide with oxygen vacancy, which uniformly separated and confined by the amorphous MOF nanosheets (Figure 22b,c).

Another successful strategy of constructing NiCo-MOF arrays was to utilize NiCo LDH array as sacrifice template to supply metal ions in the subsequent MOF growth.^[213] This general method was suitable to other MOFs with various organic linkers and metal ions on different substrates. The ultrathin NiCo-BDC nanosheets (5 nm) array displayed an excellent OER performance with an overpotential of only 230 mV to reach 10 mA cm⁻² in 1.0 M KOH. Ex situ XRD characterizations of durability test demonstrated that the peaks assigned to MOF gradually decreased within 2 h, and NiOOH broad peaks were formed after 12 h. Following the same method, Yao's group synthesized highly oriented FeNi-BDC nanoarray by adjusting metal centers (Figure 22d).^[214] The optimal Fe_{0.1}-Ni-MOF/NF could be maintained its remarkable activity for at least 20 h at 150 mA cm⁻², as well as possessed high TOF values of 0.018 and 0.086 O₂ s⁻¹ at overpotentials of 250 and 300 mV. SEM images indicated that the morphology still retained after OER test, whereas nearly no obvious diffraction peaks were observed in XRD pattern. Furthermore, XPS results verified that the real active species were the amorphous (oxy)hydroxide transformed from crystalline FeNi-MOF.

Zhu and co-workers used NiFe alloy foam as a semisacrificial template to realize the control over the thickness and architecture of MIL-53(NiFe) nanocomposite array at the molecular level.^[215] The ultrathin Ni-rich MOF nanosheets (1.56 nm) were decorated by ultrasmall Fe-rich MOF clusters (2–5 nm) (Figure 22e). XPS and Mössbauer spectrum measurements unraveled that the partial electron transfer from Ni²⁺ to Fe³⁺ led to the modification of the local electronic configuration of Ni sites (Figure 22f), which accelerated the reaction process. The self-supporting electrode showed the impressive OER activity with the overpotentials of 227 and 253 mV to achieve 10 and 100 mA cm⁻² (Figure 22g). When coupled with a Pt mesh, it only required 1.537 V to obtain 10 mA cm⁻² for water electrolysis. SEM and HRTEM images displayed no prominent change in morphology after stable operation, while probably in situ generating oxides or (oxy)hydroxides as the actual active species, verified by XRD and XPS characterizations. The unique nanostructure and the synergistic effect between Ni and Fe centers should also be responsible for the excellent catalytic performance. Similarly, NiFe-MOF nanoplates (200–300 nm) were fabricated on NF with iron carbonate hydroxide nanosheets (FeCH NSs) as a template.^[216] In this way, the porous FeCH NSs not only served as the iron source, but also slowed down the leaching of Ni ions from NF, thus regulating the shape of NiFe-MOF with reduced thickness and sizes. Based on SEM measurements, the pristine MOF morphology was essentially preserved after long-term electrolysis. Raman and TEM results of activated NiFe-MOF at 1.45 V for 5 min jointly pointed to the generated Ni(OH)₂ may be as the real active species for OER. Besides, the strong coupling interaction between Fe and Ni(OH)₂ confirmed by XPS also contributed to the high OER activity.

Ligand engineering has been demonstrated as effective method for improving the performance of self-supported 2D

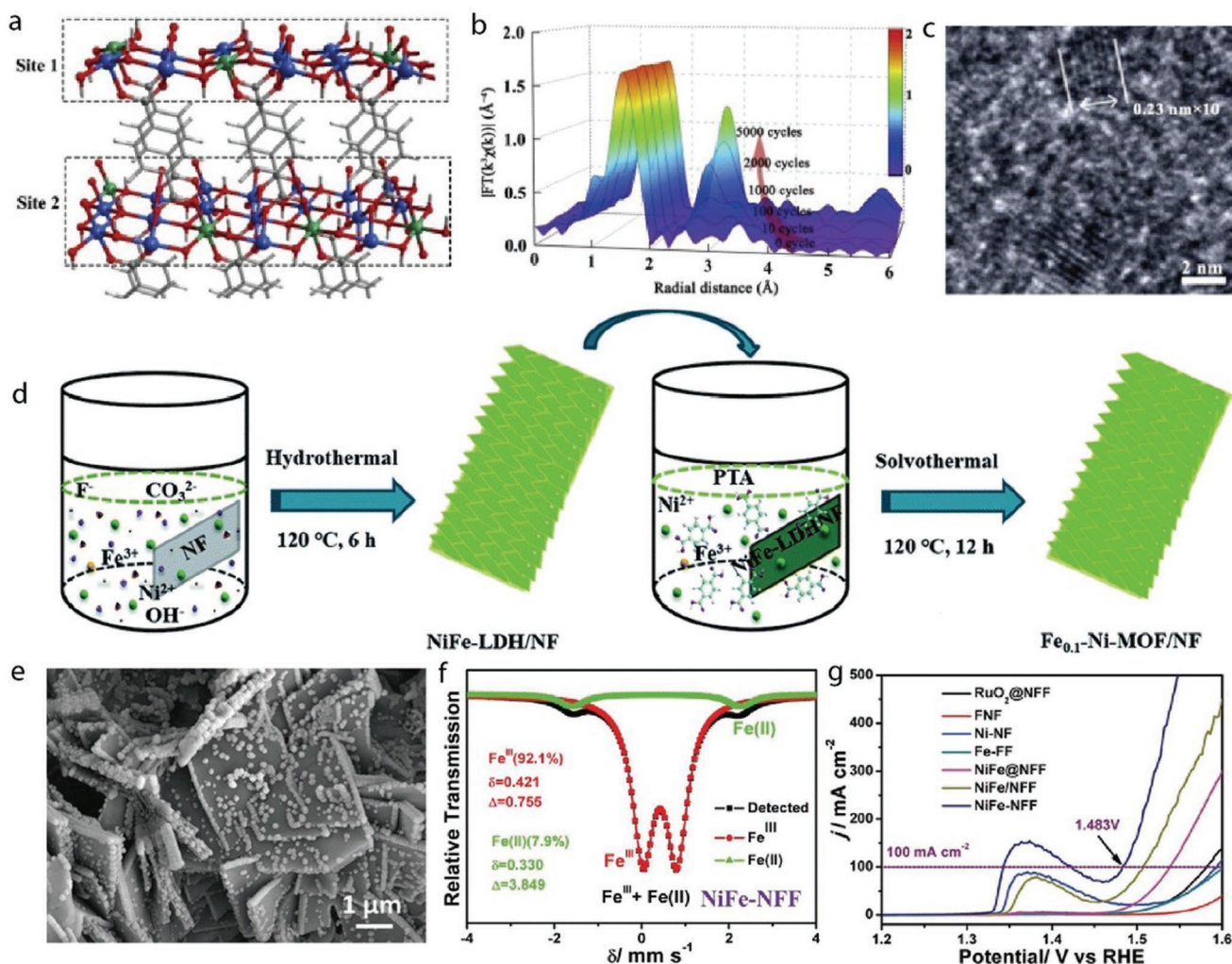


Figure 22. a) Atomic structures of coordinatively unsaturated and saturated Co or Ni sites in CoNi-MOF. b) The FT-EXAFS spectra of Ni K-edge recorded during the advance of CV cycles. c) HRTEM image of CoNi-MOF after OER stability test. a–c) Reproduced with permission.^[212] Copyright 2020, Elsevier. d) The fabrication process of $\text{Fe}_{0.1}$ -Ni-MOF arrays on 3D nickel foam. (d) Reproduced with permission.^[214] Copyright 2019, Royal Society of Chemistry. e) SEM image of NiFe-NFF. f) ^{57}Fe Mössbauer spectra of NiFe-NFF. g) OER polarization curves of the as-prepared electrocatalysts. e–g) Reproduced with permission.^[215] Copyright 2018, Wiley-VCH.

MOFs. Ferrocene (Fc) possesses excellent chemical stability as well as outstanding redox properties due to the aromaticity of two cyclopentadienyl rings.^[217] Recently, Liu and co-workers synthesized 2D MOF nanosheets with an average thickness of 30 nm on NF using Fc dicarboxylic acids as organic linkers (Figure 23a).^[100] Electrochemical measurements and DFT calculations indicated that the Fc unit served as an efficient electron transfer mediator, thereby leading to a conductor-like electronic structure of NiFc-MOF. The NiFc-MOF/NF exhibited an overpotential of 195 mV at 10 mA cm^{-2} and OER durability up to 40 h without obvious morphological changes (Figure 23b). After stability operation, partial NiFc-MOF crystalline structure was converted to $\text{Fe}_2\text{O}_2\text{CO}_3$ and $\text{Ni}(\text{OH})_2/\text{NiOOH}$ phase, which was confirmed by XRD, XPS, and in situ Raman spectroscopy. Combining with DFT results, authors considered that Ni sites were involved in the reaction and the introduction of Fc improved Ni centers catalytic ability. In addition, introducing nonbridging linkers into MOF can optimize the intrinsic activity through

modifying the electronic configuration of metal nodes. As an example, Li's group reported a missing-linker strategy to tune the coordination environment of CoBDC MOF to enhance OER properties.^[218] As illustrated in Figure 23c, nonbridging linkers of Fc were introduced into CoBDC to partially substitute multicoordinating BDC ligands, thus generating a more conductive electronic structure. After incorporating missing linkers, CoBDC-Fc exhibited the same diffraction patterns and nanosheet shapes as CoBDC. As can be seen in Figure 23d, CoBDC-Fc-NF only required a low overpotential of 178 mV to reach 10 mA cm^{-2} , far surpassing that of pristine CoBDC-NF (252 mV) and commercial RuO_2 (235 mV). Theoretical results further demonstrated that the introduced defect site optimized the adsorption capability for OER intermediates, validating the experimental data. XRD and XPS evidenced that a small amount of amorphous CoOOH was observed after 10 h stability test, while MOFs were the primary component. The unsaturated Co^{2+} centers generated by missing linkers acted as the main active sites.

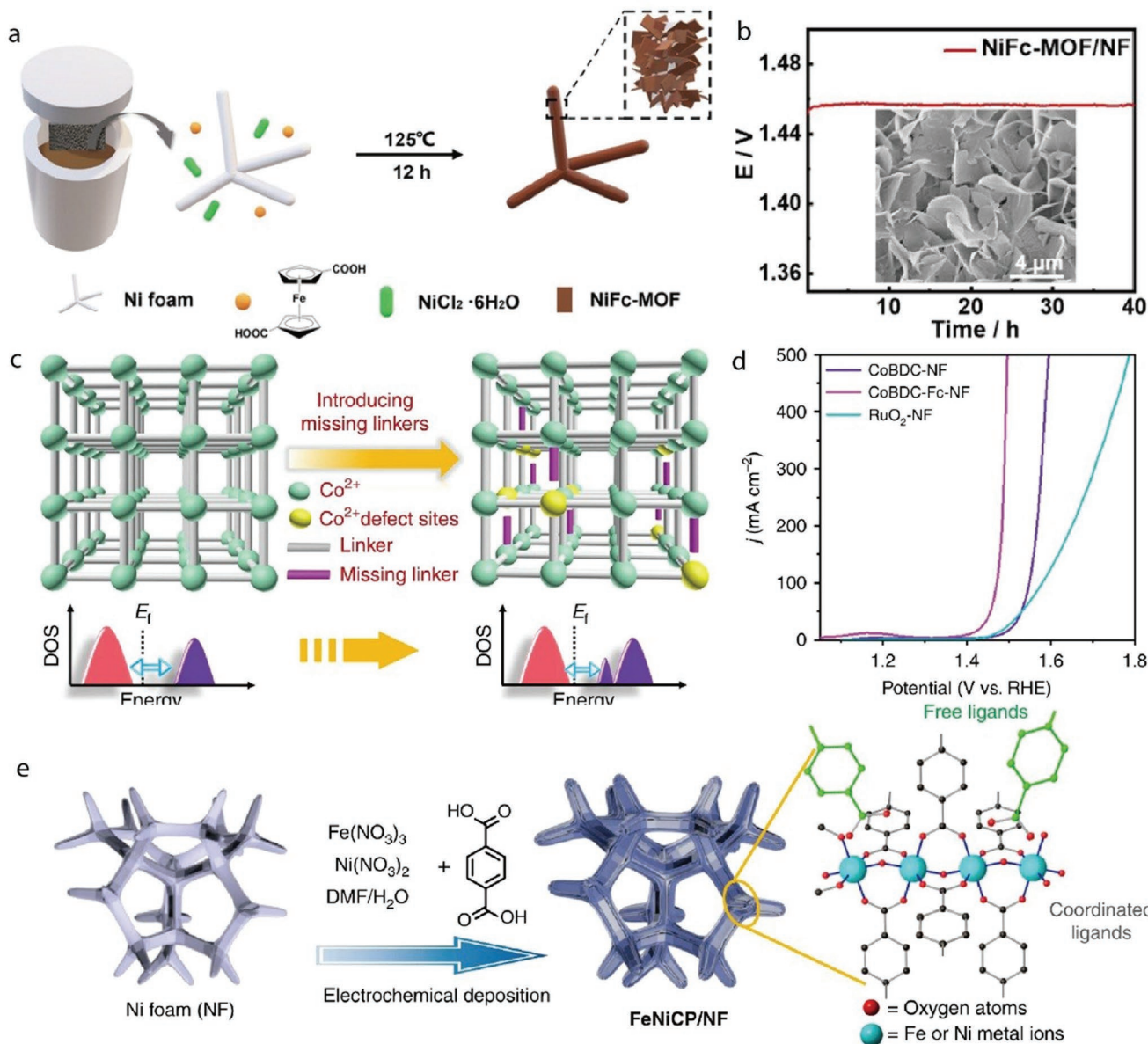


Figure 23. a) Synthetic process of NiFc-MOF nanosheet arrays on Ni foam. b) Chronopotentiometry curves of NiFc-MOF/NF at 10 mA cm^{-2} in 1.0 M KOH . Inset: SEM image of NiFc-MOF/NF after 40 h of continuous test. a,b) Reproduced with permission.^[100] Copyright 2021, Wiley-VCH. c) Framework structure and bandgap before and after missing linkers introduction in MOFs. d) Comparison of OER polarization curves for CoBDC-NF, CoBDC-Fc-NF, and $\text{RuO}_2\text{-NF}$ toward OER. c,d) Reproduced with permission.^[218] Copyright 2019, Springer Nature. e) Schematic illustration of the synthesis procedure of NiFeCP/NF. e) Reproduced with permission.^[219] Copyright 2019, Springer Nature.

Sun and co-workers prepared a Fe/Ni terephthalate coordination polymer on NF (NiFeCP/NF) via electrodeposited method (Figure 23e), and elucidated the role of coordinated and uncoordinated BDC ligands in water oxidation process.^[219] NiFeCP/NF displayed excellent OER performance with a low overpotential of 188 mV at 10 mA cm^{-2} , a small Tafel slope (29 mV dec^{-1}), and outstanding durability. XRD, XPS, FT-IR, and micro-Raman spectra suggested that the partial coordinated carboxylate groups would dissociate from metal nodes, generating additional free uncoordinated carboxylate sites and metal hydroxide species during OER. Deuterium kinetic isotope effects, proton inventory, and atom proton transfer

measurements demonstrated that the coordinated carboxylates stabilized the high metal valence states, while the uncoordinated carboxylates could participate in catalytic reaction by serving as proton transfer relays nearby the metal sites.

The dissolution of organic ligand in some MOFs can cause the completely reconstruction phenomenon, together with aggregation of metal nodes to form hydroxides or oxyhydroxides, which are responsible for the outstanding catalytic performance. Our group reported an ultralong quasi-2D Co-MOF nanoarray with the assistance of the deposited metal layer (Figure 24a).^[106] This interfacial engineering method allowed preferred chelation of linkers with the reactive metal layer,

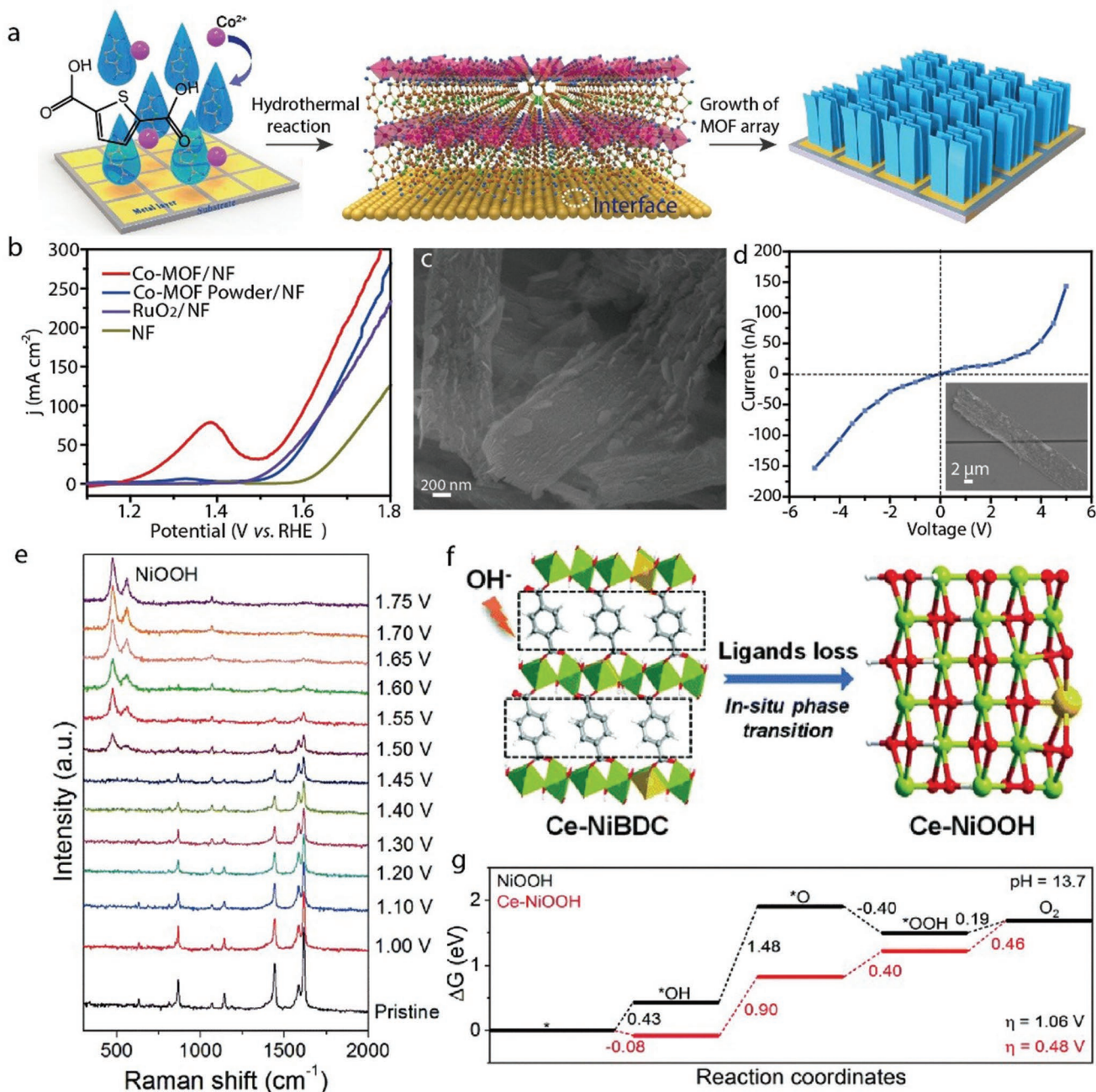


Figure 24. a) Schematic of the growth of Co-MOF nanoarrays on substrates with the evaporated metal layer. b) LSV of Co-MOF/NF, Co-MOF powder/NF, RuO₂/NF, and bare NF. c) SEM image of Co-MOF nanoarrays after OER. d) Current–voltage curves of individual Co-MOF nanobelt after OER operation. Inset: SEM image of Co-MOF nanobelt after OER test sitting across a channel separated by two gold electrodes. a–d) Reproduced with permission.^[106] Copyright 2019, Wiley-VCH. e) In situ Raman spectra of Ce-NiBDC/OG under different applied potentials. f) In situ phase transformation of Ce-NiBDC/OG to Ce-NiOOH during OER process. g) Simulated free-energy diagrams and theoretical overpotentials of NiOOH and Ce-NiOOH for OER. e–g) Reproduced with permission.^[220] Copyright 2021, Royal Society of Chemistry.

thereby fabricating MOF nanobelts (≈ 102 nm) on arbitrary substrates. The MOF nanoarrays grown on NF demonstrated high electrocatalytic capability for OER, showing a minimum overpotential of 270 mV at 10 mA cm^{-2} (Figure 24b) and superb long-term stability. The structural reorganization of Co-MOF during OER process was confirmed by XRD, XPS, and HRTEM test. As displayed in Figure 24c,d, the enhanced activity

originated from the interconnected CoOOH nanosheets, facilitating the ion and electron transport in the hierarchical porous framework. In addition, the CoOOH directly derived from Co-MOF during the fast oxidation and substitution reaction in the CV scans has a more disordered architecture, thus possessing the better activities than other reported Co-based electrocatalysts. Recently, Hou and co-workers explored the phase

transformation behavior of Ni-based MOF in electrocatalysis using in situ Raman spectroscopy and operando microscopy. They fabricated a highly aligned Ce-doped Ni-MOF nanosheet arrays with a thickness of 12 nm on oxygen-functionalized graphite foil (Ce-NiBDC/OG) by a hydrothermal method.^[220] The Ce doping resulted in a superhydrophilic and superaerophobic surface of Ce-NiBDC/OG, which facilitated the absorption of OH⁻ ions and the release of O₂ bubbles toward OER. Based on XANES, EXAFS, and XPS analyses, Ni or substituted Ce atoms were coordinated with six O stem from BDC ligands and OH⁻, as well as the existence of electron transfer from Ce to Ni atom. In 1.0 M KOH solution, Ce-NiBDC/OG exhibited a small overpotential of 265 mV at 10 mA cm⁻² and a low Tafel slope of 46 mV dec⁻¹. Postreaction XRD, XPS, and in situ Raman characterizations (Figure 24e) demonstrated that Ce-NiBDC were first dissociated to miss BDC ligands with the electric-field assisted in situ hydrolysis and further transformed into Ce-NiOOH, eventually giving the real active species (Figure 24f). Theoretical calculations further identified that the doped Ce species in NiOOH could strengthen the adsorption of *OH intermediate and decreased the energy barriers of the rate-determining step (Figure 24g).

8.3. Self-Supported 2D MOFs as Bifunctional Catalysts

Up to date, a few pristine self-supported 2D MOFs have been successfully designed for overall water splitting, which can be realized by choosing the suitable metal centers and organic ligands. Yang et al. demonstrated that the introduction of functional groups such as -OH and -NH₂ into H₂BDC could adjust the electron affinities.^[221] Low electron affinities of linkers would increase the unoccupied states density of transition metals, thus enhancing MOF intrinsic catalytic performance. For instance, Lu's group utilized NH₂-BDC as the organic linker to design a water-stable NH₂-MIL-88B(Fe₂Ni) MOF nanosheet (15 nm) arrays on the surface of 3D macroporous NF (NFN-MOF/NF) applied as the high active and durable bifunctional electrocatalyst (Figure 25a).^[92] NFN-MOF/NF displayed outstanding OER performance with an ultralow overpotential of 240 mV at 10 mA cm⁻² and extraordinary stability at high current densities of 250 and 500 mA cm⁻². For anodic OER, the coordinated water molecules in Fe₂Ni(μ₃-O) cluster could be readily released to create the coordinatively unsaturated active metal centers. In the meantime, the high utilization of catalyst, the improved mass and charge transport capacity were responsible for the distinguished OER activities. When used as HER electrode, NFN-MOF/NF also possessed the smallest overpotential of 87 mV at 10 mA cm⁻² and Tafel slope of 35.2 mV dec⁻¹, which were lower than those of the most reported transition metal based electrocatalysts. For HER, partial Fe³⁺ and Ni²⁺ ions were reduced into the corresponding metallic state to form M/MO₆ clusters. The metal centers in M/MO₆ clusters promoted the adsorption of H atom, while the MO₆ units were beneficial to attract OH⁻ ions, both accelerating the rate-limiting Volmer step. -NH₂ groups as an electron donor facilitated the water molecules reduction during Volmer process. The water electrolysis performance of NFN-MOF/NF was superior to commercial noble metals. More importantly,

the durability was also exceptional, displaying a minor chronopotentiometric decay of 7.9% at practically favorable large current density of 500 mA cm⁻² after 30 h. The similar XPS spectra, SEM images, and XRD patterns before and after test further identified the excellent stability of NFN-MOF/NF.

In another study, Lu's group prepared uniformly well-mixed and dispersed Fe- and Ni-MOF nanosheet spheres on NF based on the same ligands.^[222] They demonstrated the concept of the intermolecular synergistic interaction of direct MOF catalysts for the first time. This strong intermolecular synergistic effect between Fe- and Ni-MOF not only promoted the redox reactions but also enhanced the utilization degree of the active metal centers. MFN-MOF/NF composite exhibited remarkable overall water splitting activities with an ultralow cell voltage of 1.80 V at 500 mA cm⁻² and the ultrastability over 100 h at high current densities, as well as nearly 100% Faraday efficiency. After the continuous operation, the electronic structures and composition were well-maintained. The authors proposed that metallic Ni atom and Ni²⁺ in MFN-MOFs would facilitate the adsorption of H atom and OH⁻ ions, whereas metal cluster in Fe-MOF and -NH₂ accelerated the reduction of water molecules, thus improving the HER performances. Moreover, Ni²⁺ was much more active than Fe³⁺ site in MFN-MOFs toward OER, while the coordinatively unsaturated Fe³⁺ centers assisted to improve the activity of Ni atom.

Yan and co-workers recently developed a new cocrystallized strategy to construct Co/Ni-based 2D metal-organic nanosheet array (NiCo-9AC-AD, 9-AC = 9-anthracic acid, HAD = protonated acridine) (Figure 25b) on NF.^[223] The mixing of Co/Ni could adjust the morphology of NiCo-9AC-AD nanosheets and the electronic structure of Ni center, thereby boosting the inherent catalytic activity. The optimized Ni_{0.3}Co_{0.7}-9AC-AD/NF delivered low overpotentials of 350 mV for OER at 100 mA cm⁻² and 143 mV for HER at 10 mA cm⁻², respectively. In addition, it required merely 1.56 V to obtain 10 mA cm⁻² as an integrated overall water splitting electrocatalyst. XRD and TEM analysis disclosed no significant change in material structure and shape after durability test. The high activities were attributed to the following factors. i) Ni²⁺ ions facilitated the spin-orbit coupling and improve the charge transfer efficiency, while Ni coordinated with H₂O was conducive to the adsorption of water molecules in the solution. ii) The thin and small nanosheet arrays exposed more available active sites and reduced the ion transport distance. iii) The synergistic interaction between Co and Ni increased the intrinsic catalytic capacity. iv) The existence of π-π stacking effect in NiCo-9AC-AD accelerated the catalytic kinetics.

In the work of Li's group, the defect-rich ultrathin Ni(II)-MOF (ligand: H₂BDC) nanosheet (5.1 nm) array as an efficient electrocatalyst toward water splitting was fabricated by a simply alkali-etched strategy (Figure 25c).^[224] The original MOF topology structure was well maintained after the etching treatment. However, the intrusion of KOH resulted in the partial breaking of Ni-O bonds in Ni-MOF, accompanied with the generation of oxygen vacancies and more open Ni sites with high valence state, thereby decreasing the rate-determining energy barrier for OER and HER. Additionally, the introduced K⁺ ions acted as conduction ions were favorable for charge transfer, ultimately boosting the

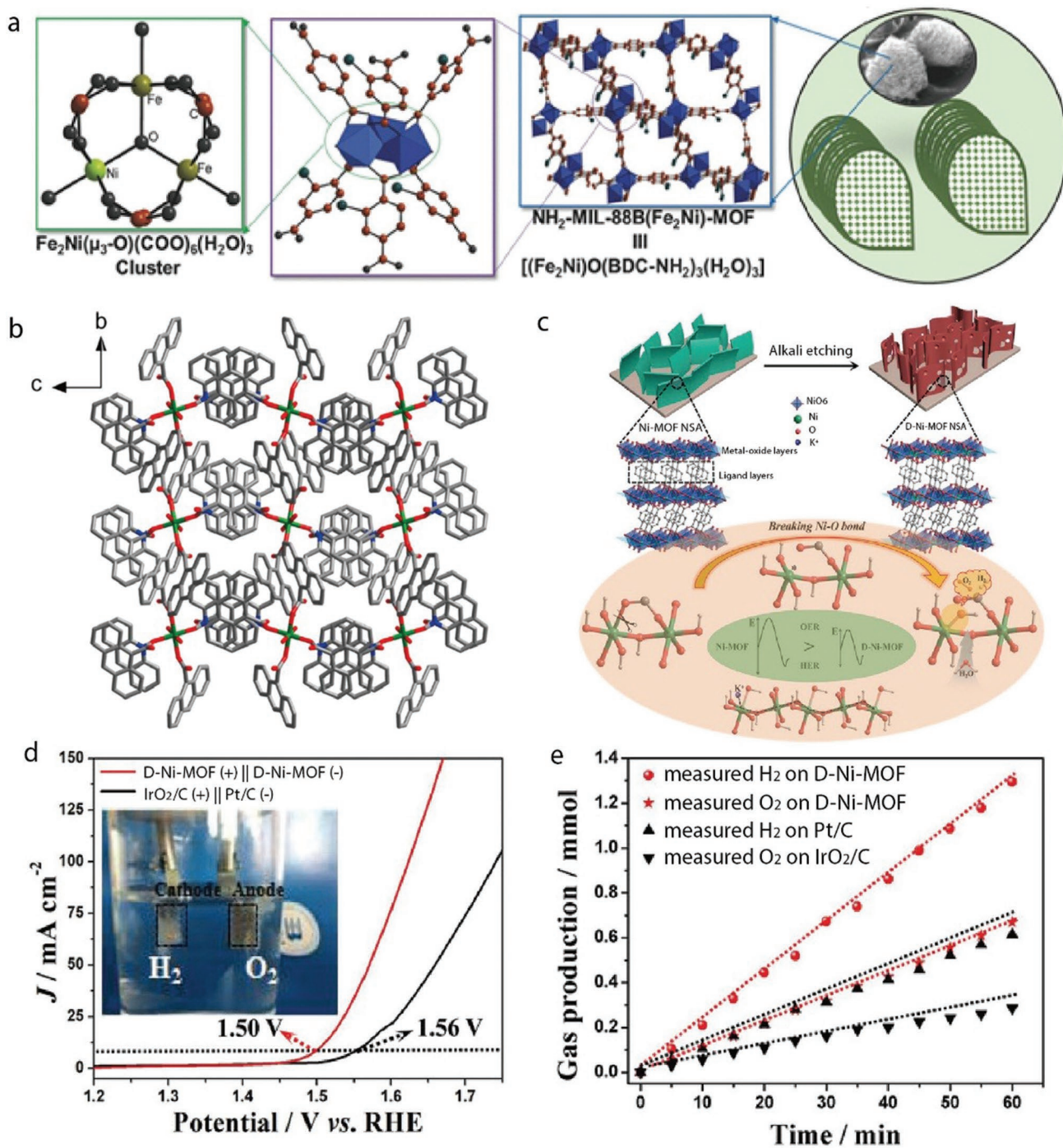


Figure 25. a) Structure and morphology of $\text{NH}_2\text{-MIL-88B}(\text{Fe}_2\text{Ni})\text{-MOF}$ nanosheets. a) Reproduced with permission.^[92] Copyright 2018, Wiley-VCH. b) The coordination mode of Ni-9AC-AD. b) Reproduced with permission.^[223] Copyright 2019, American Chemical Society. c) Schematic of preparing D-Ni-MOF for overall water splitting. d) LSV plots of different materials in the two-electrode toward overall water splitting in 1.0 M KOH. Inset: the production of H_2 and O_2 gas bubbles on the electrode surface. e) The tested and theoretical amounts of produced gas against time of D-Ni-MOF and commercial catalyst. c–e) Reproduced with permission.^[224] Copyright 2020, Wiley-VCH.

reaction kinetics. As a result, the two-electrode cell assembled by defect-Ni-MOF delivered a low voltage of 1.50 V at 10 mA cm^{-2} in 1.0 M KOH for overall water splitting, outperforming that of the benchmark precious catalysts (1.56 V) and showing a high Faradic efficiency (Figure 25d,e). HRTEM and PXRD confirmed the good chemical stability of MOF during

electrocatalytic process, although some NiOOH active species were formed.

As to the bifunctional catalysts, several 2D MOFs underwent partially or completely evolution into different active species to catalyze HER and OER. Zhao and co-workers reported the construction of 2D ultrathin NiFe-MOF

(ligand: 2,6-naphthalenedicarboxylic acid dipotassium) nanosheets (≈ 3.5 nm) on the surface of NF with a dissolution–crystallization method for overall water splitting.^[99] Metal ions coordinated to two monodentate carboxylates and four H₂O molecules, while each naphthalene dicarboxylate bridged two metal atoms. The unique hierarchical porous structure and the highly exposed metal sites were beneficial to electrocatalytic reaction. Importantly, the ultrathin NiFe-MOF nanosheets had intrinsic high electrical conductivity ($1 \pm 0.2 \times 10^{-3}$ S m⁻¹), which significantly facilitated the charge transport. Consequently, NiFe-MOF nanoarrays demonstrated the remarkable catalytic performance, the favorable kinetics and the high stability toward OER, HER, and overall water splitting. During OER process, NiO₆ units inside MOF were oxidized into NiO₆/NiOOH species as active sites, which accelerated the oxidation of OH⁻. For HER pathway, NiO₆ was partially reduced to form Ni/NiO₆ interface. At this interface, the generated OH⁻ species by H₂O splitting attached to the locally positively charged Ni²⁺ ions, while the nearby Ni site would promote H adsorption.

Recently, Li's group embedded unique MS clusters on the surface of ultrathin Fe/Ni-MOF (ligand: H₂BDC) nanosheets (20–30 nm) to boost the electrocatalytic performance.^[71] The impregnated MS clusters not only provided high electric conductivity, but also regulated the electronic configuration of active centers to an electron-rich state. The composite displayed remarkable catalytic activity, requiring the overpotentials of 230 and 156 mV to drive 50 mA cm⁻² for OER and HER, respectively. It only needed low cell voltages of 1.61 and 1.74 V to afford the electrolytic current density of 10 and 50 mA cm⁻² for water splitting. After OER testing, MOF crystalline structure transformed to disordered oxyhydroxides, which were responsible for the high catalytic performance. A similar phenomenon was observed during HER, the MO₆ units in Fe/Ni-MOF were partially reduced to disordered M/MO₆ interface and in situ formed hydroxide active material.

PBAs have often been explored as an efficient OER electrocatalyst, and have recently been studied for promoting HER process. By taking advantage of self-assembly, Wu and co-workers reported CoFe-PBA nanosheet (5 nm) arrays with ultrathin feature and open metal sites as outstanding bifunctional electrocatalysts.^[37] Remarkably, the optimized CoFe-PBA arrays only needed 256 and 48 mV overpotentials to reach 10 mA cm⁻² for OER and HER in 1.0 M KOH. Meanwhile, it required 1.545 V cell voltage to drive water electrolysis at 10 mA cm⁻², outperforming that of commercial catalysts (1.608 V). Based on XRD, TEM, and XPS characterizations after OER test, it was identified that there existed a phase transition from single structure to amorphous or low crystallinity metal (oxy)hydroxides. Furthermore, EIS spectra showed an enhanced charge transfer ability after OER cycling. Similar to the OER case, the in situ generated Co/Fe hydroxides function as the active phase to catalyze HER, while the morphology and chemical states kept unchanged. According to DFT calculations, authors illustrated that the presence of unsaturated Fe/Co centers were favorable for adsorbing OH⁻, thereby promoting the formation of high active phase.

9. Conclusions and Perspectives

High-efficiency electrocatalysts for OER and HER can greatly expedite the development of sustainable energy conversion technology. The primitive 2D MOFs are competent and cost-effective candidates, owing to their unique characteristics of high specific surface areas, abundant open active sites, improved electrical conductivity, rapid mass transfer capability, and structural tunability. This review systemically outlines the research progress in pristine 2D MOFs as electrocatalysts for efficient electrochemical water splitting. The preparation of 2D MOFs and strategies for the performance enhancement are detailly summarized, with particular focus on the elucidation of catalytic mechanism and the actual active sites.

Despite the fruitful achievements in the development of pristine 2D MOFs for efficient water splitting, some associated challenges toward the fundamental understanding and practical applications of 2D MOFs still exist.

1. Structural design and analysis. Stable 2D MOFs with strong coordination bonds and structures are still required to limit the degradation of MOFs under rigorous electrochemical conditions, therefore the unique features of 2D MOFs can be fully exploited to prepare durable and efficient water electrolysis catalysts. In order to enhance the performance, heterogeneous metal ions can be incorporated into 2D MOFs to regulate the binding strength of reaction intermediates. In these multimetallic MOFs, metal ions are randomly distributed throughout MOF matrices. Detailed characterizations with advanced methods are necessary to confirm the accurate structural and topological information of the heterogenous framework, namely, whether metal cations are mixed in the same or different secondary building units.
2. Conductivity. Suitable conductivities in MOFs benefit the charge transfer during the electrocatalysis. Conductive 2D MOFs usually possess the fully π -conjugated structures via M-X₄ (X = N, S, and O) linkages. The currently reported 2D conductive MOFs are limited to specific organic ligands with poor scalability. Considering the hard–soft acid–base theory, the hard–hard interactions between metal nodes and chelating atoms tend to form ionic bonds, whereas soft–soft combination leads to covalent interactions. Soft atoms such as N, S coordinating to soft metal ions may produce more covalent bonds, which are favorable for the optimization of conductive pathways through π -d conjugation. Introducing comparatively harder O atoms result in energy gaps and trapped valence states that restrict conductivity. Therefore, optimizing the hardness and softness of metal ions and coordination atoms will continue to improve the conductivities of 2D MOFs.
3. Practical applications. At present, most of the reported 2D-MOF based electrocatalysts are evaluated at low current densities (<100 mA cm⁻²), which are not high enough for commercial applications. Measurements of overpotential and durability at practically meaningful high current densities (e.g., 500 mA cm⁻²) can better reflect the real advantages

of electrocatalysts for practical operation. In addition, efficient bifunctional electrocatalysts are to be developed. While many 2D MOF materials have displayed comparable or even better performance than the benchmarked noble metal catalysts toward OER, relatively very few of them are employed to catalyze HER. Thus, it is necessary to find reliable ways to construct the efficient bifunctional electrocatalysts. For instance, active sites in MOFs can be tailored by doping various metal atoms with intrinsic electrocatalytic water splitting ability. Furthermore, adding other active species (e.g., metal nanoparticles, active compounds) into frameworks or modifying ligands may synergistically facilitate the catalytic reactions.

4. Identification of catalytic mechanism. During HER or OER process, phase transformation may occur on the surfaces of 2D MOFs to generate the real active sites. The methods of evaluating MOFs stability are crucial to envisage its intrinsic catalytic performance. PXRD technique is the primary means for characterizing MOFs structural features. Nonetheless, the exposure of MOFs to HER and OER operating conditions may introduce defects or new species with a thickness of a few nanometers and does not destroy the overall structure, thus making them undetectable by PXRD alone. In this regard, MOF structures after electrocatalysis need to be detailly analyzed by precise characterizations in combination with ex situ or in situ technologies. For example, the reconstructive low concentration phase may be identified by HRTEM, while the coordination environment changes of metal ions can be explored through XAS. These practices are benefiting to the illustration of the real catalytic mechanism of pristine 2D MOFs. In addition, the correlation between reconstruction degree (partial or complete reconstruction) and activity should be systematically studied, which will offer guidance for future electrocatalyst design. Although DFT calculations can provide insight into the catalytic mechanism and the reveal active species, it is imperative to verify whether the established theoretical model is based on precatalyst or reconstructed phases.

Acknowledgements

The work was supported by NSFC (51873088) and 111 Project (B18030) in China. The authors also acknowledge the financial support by Haihe Laboratory of Sustainable Chemical Transformations (No. YYJC202101).

Conflict of Interest

The authors declare no conflict of interest.

Keywords

2D materials, electrocatalytic water splitting, hydrogen evolution reaction, metal–organic frameworks, oxygen evolution reaction

Received: November 30, 2022
Published online:

- [1] D. E. H. J. Gernaat, P. W. Bogaart, D. P. v. Vuuren, H. Biemans, R. Niessink, *Nat. Energy* **2017**, 2, 821.
- [2] W. Cheng, H. Zhang, D. Luan, X. W. D. Lou, *Sci. Adv.* **2021**, 7, 2580.
- [3] Z. W. Seh, J. Kibsgaard, C. F. Dickens, I. Chorkendorff, J. K. Norskov, T. F. Jaramillo, *Science* **2017**, 355, 4998.
- [4] S. Jiao, X. Fu, S. Wang, Y. Zhao, *Energy Environ. Sci.* **2021**, 14, 1722.
- [5] Z. Y. Yu, Y. Duan, X. Y. Feng, X. Yu, M. R. Gao, S. H. Yu, *Adv. Mater.* **2021**, 33, 2007100.
- [6] X. Liu, M. Gong, S. Deng, T. Zhao, T. Shen, J. Zhang, D. Wang, *Adv. Funct. Mater.* **2020**, 31, 2009032.
- [7] Q. Wang, D. Astruc, *Chem. Rev.* **2020**, 120, 1438.
- [8] J. Zhang, T. Bai, H. Huang, M. H. Yu, X. Fan, Z. Chang, X. H. Bu, *Adv. Mater.* **2020**, 32, 2004747.
- [9] L. Kong, M. Liu, H. Huang, Y. Xu, X. H. Bu, *Adv. Energy Mater.* **2021**, 12, 2100172.
- [10] W. P. Lustig, S. Mukherjee, N. D. Rudd, A. V. Desai, J. Li, S. K. Ghosh, *Chem. Soc. Rev.* **2017**, 46, 3242.
- [11] H. Zhang, J. Nai, L. Yu, X. W. Lou, *Joule* **2017**, 1, 77.
- [12] H. Zhong, K. H. Ly, M. Wang, Y. Krupskaya, X. Han, J. Zhang, J. Zhang, V. Kataev, B. Buchner, I. M. Weidinger, S. Kaskel, P. Liu, M. Chen, R. Dong, X. Feng, *Angew. Chem., Int. Ed.* **2019**, 58, 10677.
- [13] L. Li, J. He, Y. Wang, X. Lv, X. Gu, P. Dai, D. Liu, X. Zhao, *J. Mater. Chem. A* **2019**, 7, 1964.
- [14] G. Xu, P. Nie, H. Dou, B. Ding, L. Li, X. Zhang, *Mater. Today* **2017**, 20, 191.
- [15] T. Qiu, Z. Liang, W. Guo, H. Tabassum, S. Gao, R. Zou, *ACS Energy Lett.* **2020**, 5, 520.
- [16] L. Kong, M. Zhong, W. Shuang, Y. Xu, X. H. Bu, *Chem. Soc. Rev.* **2020**, 49, 2378.
- [17] H. B. Aiyappa, J. Masa, C. Andronescu, M. Muhler, R. A. Fischer, W. Schuhmann, *Small Methods* **2019**, 3, 1800415.
- [18] L. Sun, M. G. Campbell, M. Dinca, *Angew. Chem., Int. Ed.* **2016**, 55, 3566.
- [19] H. F. Wang, L. Chen, H. Pang, S. Kaskel, Q. Xu, *Chem. Soc. Rev.* **2020**, 49, 1414.
- [20] Z. Li, M. Song, W. Zhu, W. Zhuang, X. Du, L. Tian, *Coord. Chem. Rev.* **2021**, 439, 213946.
- [21] G. Zhang, Y. Li, X. Xiao, Y. Shan, Y. Bai, H. G. Xue, H. Pang, Z. Tian, Q. Xu, *Nano Lett.* **2021**, 21, 3016.
- [22] H. Su, S. Song, S. Li, Y. Gao, L. Ge, W. Song, T. Ma, J. Liu, *Appl. Catal., B* **2021**, 293, 120225.
- [23] K. C. Kwon, J. M. Suh, R. S. Varma, M. Shokouhimehr, H. W. Jang, *Small Methods* **2019**, 3, 1800492.
- [24] H. B. Wu, X. W. D. Lou, *Sci. Adv.* **2017**, 3, 9252.
- [25] Z. Liang, T. Qiu, S. Gao, R. Zhong, R. Zou, *Adv. Energy Mater.* **2021**, 12, 2003410.
- [26] Z. Li, R. Gao, M. Feng, Y. P. Deng, D. Xiao, Y. Zheng, Z. Zhao, D. Luo, Y. Liu, Z. Zhang, D. Wang, Q. Li, H. Li, X. Wang, Z. Chen, *Adv. Energy Mater.* **2021**, 11, 2003291.
- [27] B. Zhu, R. Zou, Q. Xu, *Adv. Energy Mater.* **2018**, 8, 1801193.
- [28] C. Xie, D. Yan, W. Chen, Y. Zou, R. Chen, S. Zang, Y. Wang, X. Yao, S. Wang, *Mater. Today* **2019**, 31, 47.
- [29] N. Kornienko, Y. Zhao, C. S. Kley, C. Zhu, D. Kim, S. Lin, C. J. Chang, O. M. Yaghi, P. Yang, *J. Am. Chem. Soc.* **2015**, 137, 14129.
- [30] L. S. Xie, L. Sun, R. Wan, S. S. Park, J. A. DeGayner, C. H. Hendon, M. Dinca, *J. Am. Chem. Soc.* **2018**, 140, 7411.
- [31] Y. L. Liu, X. Y. Liu, L. Feng, L. X. Shao, S. J. Li, J. Tang, H. Cheng, Z. Chen, R. Huang, H. C. Xu, J. L. Zhuang, *ChemSusChem* **2022**, 15, 202102603.
- [32] H. An, Y. Hu, N. Song, T. Mu, S. Bai, Y. Peng, L. Liu, Y. Tang, *Chem. Sci.* **2022**, 13, 3035.
- [33] X. Ao, Y. Gu, C. Li, Y. Wu, C. Wu, S. Xun, A. Nikiforov, C. Xu, J. Jia, W. Cai, R. Ma, K. Huo, C. Wang, *Appl Catal B* **2022**, 315, 121586.

- [34] A. J. Clough, J. W. Yoo, M. H. Mecklenburg, S. C. Marinescu, *J. Am. Chem. Soc.* **2015**, *137*, 118.
- [35] R. Dong, M. Pfeffermann, H. Liang, Z. Zheng, X. Zhu, J. Zhang, a. X. Feng, *Angew. Chem., Int. Ed.* **2015**, *127*, 12226.
- [36] S. Zhao, Y. Wang, J. Dong, C.-T. He, H. Yin, P. An, K. Zhao, X. Zhang, C. Gao, L. Zhang, J. Lv, J. Wang, J. Zhang, A. M. Khatkhat, N. A. Khan, Z. Wei, J. Zhang, S. Liu, Z. Tang, H. Zhao, *Nat. Energy* **2016**, *1*, 16184.
- [37] Z. Chen, B. Fei, M. Hou, X. Yan, M. Chen, H. Qing, R. Wu, *Nano Energy* **2020**, *68*, 104371.
- [38] Y. Sun, Z. Xue, Q. Liu, Y. Jia, Y. Li, K. Liu, Y. Lin, M. Liu, G. Li, C. Y. Su, *Nat. Commun.* **2021**, *12*, 1369.
- [39] H. S. Jadhav, H. A. Bandal, S. Ramakrishna, H. Kim, *Adv. Mater.* **2022**, *34*, 2107072.
- [40] B. Zhang, Y. Zheng, T. Ma, C. Yang, Y. Peng, Z. Zhou, M. Zhou, S. Li, Y. Wang, C. Cheng, *Adv. Mater.* **2021**, *33*, 2006042.
- [41] J.-B. Tan, G.-R. Li, *J. Mater. Chem. A* **2020**, *8*, 14326.
- [42] Y. Yang, Y. Yang, Y. Liu, S. Zhao, Z. Tang, *Small Sci.* **2021**, *1*, 2100015.
- [43] H. Wu, J. Wang, W. Jin, Z. Wu, *Nanoscale* **2020**, *12*, 18497.
- [44] H. Sun, X. Xu, Y. Song, W. Zhou, Z. Shao, *Adv. Funct. Mater.* **2021**, *31*, 2009779.
- [45] Y. Zhai, X. Ren, J. Yan, S. Liu, *Small Struct.* **2020**, *2*, 2000096.
- [46] S. Anantharaj, S. Noda, *Small* **2020**, *16*, 1905779.
- [47] J. Wang, Y. Gao, H. Kong, J. Kim, S. Choi, F. Ciucci, Y. Hao, S. Yang, Z. Shao, J. Lim, *Chem. Soc. Rev.* **2020**, *49*, 9154.
- [48] Y. Li, X. Wei, L. Chen, J. Shi, *Angew. Chem., Int. Ed.* **2021**, *60*, 19550.
- [49] Q. Fu, J. Han, X. Wang, P. Xu, T. Yao, J. Zhong, W. Zhong, S. Liu, T. Gao, Z. Zhang, L. Xu, B. Song, *Adv. Mater.* **2021**, *33*, 1907818.
- [50] Z. Zhou, Z. Pei, L. Wei, S. Zhao, X. Jian, Y. Chen, *Energy Environ. Sci.* **2020**, *13*, 3185.
- [51] X. Tian, P. Zhao, W. Sheng, *Adv. Mater.* **2019**, *31*, 1808066.
- [52] J. Zhu, L. Hu, P. Zhao, L. Y. S. Lee, K. Y. Wong, *Chem. Rev.* **2020**, *120*, 851.
- [53] B. You, M. T. Tang, C. Tsai, F. Abild-Pedersen, X. Zheng, H. Li, *Adv. Mater.* **2019**, *31*, 1807001.
- [54] F. Liu, C. Shi, X. Guo, Z. He, L. Pan, Z. F. Huang, X. Zhang, J. J. Zou, *Adv. Sci.* **2022**, *9*, 2200307.
- [55] M. Yu, E. Budiyananto, H. Tuysuz, *Angew. Chem., Int. Ed.* **2021**, *60*, 2.
- [56] K. Zhang, R. Zou, *Small* **2021**, *17*, 2100129.
- [57] R. Gao, D. Yan, *Adv. Energy Mater.* **2020**, *10*, 1900954.
- [58] S. Zuo, Z. P. Wu, H. Zhang, X. W. Lou, *Adv. Energy Mater.* **2022**, *12*, 2103383.
- [59] Z. P. Wu, X. F. Lu, S. Q. Zang, X. W. Lou, *Adv. Funct. Mater.* **2020**, *30*, 1910274.
- [60] H. Dau, C. Limberg, T. Reier, M. Risch, S. Roggan, P. Strasser, *ChemCatChem* **2010**, *2*, 724.
- [61] I. C. Man, H. Y. Su, F. Calle-Vallejo, H. A. Hansen, J. I. Martínez, N. G. Inoglu, J. Kitchin, T. F. Jaramillo, J. K. Nørskov, J. Rossmeisl, *ChemCatChem* **2011**, *3*, 1159.
- [62] M. Zhou, X. W. Lou, Y. Xie, *Nano Today* **2013**, *8*, 598.
- [63] Y. Bai, C. Liu, Y. Shan, T. Chen, Y. Zhao, C. Yu, H. Pang, *Adv. Energy Mater.* **2021**, *12*, 2100346.
- [64] S. S. Sankar, K. Karthick, K. Sangeetha, A. Karmakar, S. Kundu, *ACS Appl. Nano Mater.* **2020**, *3*, 4274.
- [65] Y. Zhou, Y. Chen, M. Wei, H. Fan, X. Liu, Q. Liu, Y. Liu, J. Cao, L. Yang, *CrystEngComm* **2021**, *23*, 69.
- [66] W. Zhang, X. Zhao, Y. Zhao, J. Zhang, X. Li, L. Fang, L. Li, *ACS Appl. Mater. Interfaces* **2020**, *12*, 10280.
- [67] H. Xu, H. Shang, C. Wang, Y. Du, *Adv. Funct. Mater.* **2020**, *30*, 2006317.
- [68] B. Jiang, Y. Guo, J. Kim, A. E. Whitten, K. Wood, K. Kani, A. E. Rowan, J. Henzie, Y. Yamauchi, *J. Am. Chem. Soc.* **2018**, *140*, 12434.
- [69] Q. Wang, F. Wei, D. Manoj, Z. Zhang, J. Xiao, X. Zhao, F. Xiao, H. Wang, S. Wang, *Chem. Commun.* **2019**, *55*, 11307.
- [70] Y.-C. Zhang, C. Han, J. Gao, L. Pan, J. Wu, X.-D. Zhu, J.-J. Zou, *ACS Catal.* **2021**, *11*, 12485.
- [71] M. Zhao, W. Li, J. Li, W. Hu, C. M. Li, *Adv. Sci.* **2020**, *7*, 2001965.
- [72] R. Du, Y. Wu, Y. Yang, T. Zhai, T. Zhou, Q. Shang, L. Zhu, C. Shang, Z. Guo, *Adv. Energy Mater.* **2021**, *11*, 2100154.
- [73] M. Eddaoudi, J. Kim, N. Rosi, D. Vodak, J. Wachter, M. O'Keeffe, O. M. Yaghi, *Science* **2002**, *295*, 469.
- [74] J. L. C. Rowsell, O. M. Yaghi, *Microporous Mesoporous Mater.* **2004**, *73*, 3.
- [75] S. Natarajan, P. Mahata, *Chem. Soc. Rev.* **2009**, *38*, 2304.
- [76] W. Zheng, C.-S. Tsang, L. Y. S. Lee, K.-Y. Wong, *Mater Today Chem* **2019**, *12*, 34.
- [77] A. Dhakshinamoorthy, A. M. Asiri, H. Garcia, *Adv. Mater.* **2019**, *31*, 1900617.
- [78] G. Chang, H. Zhang, X.-Y. Yu, *J. Alloys Compd.* **2022**, *919*, 165823.
- [79] D. Zhu, M. Qiao, J. Liu, T. Tao, C. Guo, *J. Mater. Chem. A* **2020**, *8*, 8143.
- [80] B. D. McCarthy, A. M. Beiler, B. A. Johnson, T. Liseev, A. T. Castner, S. Ott, *Coord. Chem. Rev.* **2020**, *406*, 213137.
- [81] S. Yuan, L. Feng, K. Wang, J. Pang, M. Bosch, C. Lollar, Y. Sun, J. Qin, X. Yang, P. Zhang, Q. Wang, L. Zou, Y. Zhang, L. Zhang, Y. Fang, J. Li, H. C. Zhou, *Adv. Mater.* **2018**, *30*, 1704303.
- [82] T. He, X.-J. Kong, J.-R. Li, *Acc. Chem. Res.* **2021**, *54*, 3083.
- [83] F. Zheng, D. Xiang, P. Li, Z. Zhang, C. Du, Z. Zhuang, X. Li, W. Chen, *ACS Sustainable Chem. Eng.* **2019**, *7*, 9743.
- [84] F. L. Li, Q. Shao, X. Huang, J. P. Lang, *Angew. Chem., Int. Ed.* **2018**, *57*, 1888.
- [85] T. Wen, Y. Zheng, J. Zhang, K. Davey, S. Z. Qiao, *Adv. Sci.* **2019**, *6*, 1801920.
- [86] X. L. Wang, L. Z. Dong, M. Qiao, Y. J. Tang, J. Liu, Y. Li, S. L. Li, J. X. Su, Y. Q. Lan, *Angew. Chem., Int. Ed.* **2018**, *57*, 9660.
- [87] X. F. Lu, P. Q. Liao, J. W. Wang, J. X. Wu, X. W. Chen, C. T. He, J. P. Zhang, G. R. Li, X. M. Chen, *J. Am. Chem. Soc.* **2016**, *138*, 8336.
- [88] J. S. Qin, D. Y. Du, W. Guan, X. J. Bo, Y. F. Li, L. P. Guo, Z. M. Su, Y. Y. Wang, Y. Q. Lan, H. C. Zhou, *J. Am. Chem. Soc.* **2015**, *137*, 7169.
- [89] W. Zheng, L. Y. S. Lee, *ACS Energy Lett.* **2021**, *6*, 2838.
- [90] Y. Xu, S. Yu, T. Ren, S. Liu, Z. Wang, X. Li, L. Wang, H. Wang, *ACS Appl. Mater. Interfaces* **2020**, *12*, 34728.
- [91] L. Zhuang, L. Ge, H. Liu, Z. Jiang, Y. Jia, Z. Li, D. Yang, R. K. Hocking, M. Li, L. Zhang, X. Wang, X. Yao, Z. Zhu, *Angew. Chem., Int. Ed.* **2019**, *58*, 13565.
- [92] D. Senthil Raja, X.-F. Chuah, S.-Y. Lu, *Adv. Energy Mater.* **2018**, *8*, 1801065.
- [93] J. Cravillon, S. Münzer, S.-J. Lohmeier, A. Feldhoff, K. Huber, M. Wiebecke, *Chem. Mater.* **2009**, *21*, 1410.
- [94] Q. Qi, J. Hu, Y. Zhang, W. Li, B. Huang, C. Zhang, *Adv. Energy Sustainability Res.* **2020**, *2*, 2000067.
- [95] J. Xu, Y. Zhao, M. Li, G. Fan, L. Yang, F. Li, *Electrochim. Acta* **2019**, *307*, 275.
- [96] M. Ding, J. Chen, M. Jiang, X. Zhang, G. Wang, *J. Mater. Chem. A* **2019**, *7*, 14163.
- [97] Y. Yang, M. Luo, W. Zhang, Y. Sun, X. Chen, S. Guo, *Chem* **2018**, *4*, 2054.
- [98] N. C. S. Selvam, L. Du, B. Y. Xia, P. J. Yoo, B. You, *Adv. Funct. Mater.* **2020**, *31*, 2008190.
- [99] J. Duan, S. Chen, C. Zhao, *Nat. Commun.* **2017**, *8*, 15341.
- [100] J. Liang, X. Gao, B. Guo, Y. Ding, J. Yan, Z. Guo, E. C. M. Tse, J. Liu, *Angew. Chem., Int. Ed.* **2021**, *60*, 12770.
- [101] S. Zhao, C. Tan, C.-T. He, P. An, F. Xie, S. Jiang, Y. Zhu, K.-H. Wu, B. Zhang, H. Li, J. Zhang, Y. Chen, S. Liu, J. Dong, Z. Tang, *Nat. Energy* **2020**, *5*, 881.

- [102] C.-P. Wang, Y. Feng, H. Sun, Y. Wang, J. Yin, Z. Yao, X.-H. Bu, J. Zhu, *ACS Catal.* **2021**, *11*, 7132.
- [103] K. Rui, G. Zhao, Y. Chen, Y. Lin, Q. Zhou, J. Chen, J. Zhu, W. Sun, W. Huang, S. X. Dou, *Adv. Funct. Mater.* **2018**, *28*, 1801554.
- [104] K. Ge, S. Sun, Y. Zhao, K. Yang, S. Wang, Z. Zhang, J. Cao, Y. Yang, Y. Zhang, M. Pan, L. Zhu, *Angew. Chem., Int. Ed.* **2021**, *60*, 12097.
- [105] Q. Qian, Y. Li, Y. Liu, L. Yu, G. Zhang, *Adv. Mater.* **2019**, *31*, 1901139.
- [106] C. P. Wang, H. Y. Liu, G. Bian, X. Gao, S. Zhao, Y. Kang, J. Zhu, X. H. Bu, *Small* **2019**, *15*, 1906086.
- [107] J. Liu, X. Song, T. Zhang, S. Liu, H. Wen, L. Chen, *Angew. Chem., Int. Ed.* **2020**, *60*, 5612.
- [108] E. M. Johnson, S. Ilic, A. J. Morris, *ACS Cent. Sci.* **2021**, *7*, 445.
- [109] L. Lin, Q. Zhang, Y. Ni, L. Shang, X. Zhang, Z. Yan, Q. Zhao, J. Chen, *Chem* **2022**, *8*, 1822.
- [110] H. Huang, Y. Zhao, Y. Bai, F. Li, Y. Zhang, Y. Chen, *Adv. Sci.* **2020**, *7*, 2000012.
- [111] X. Huang, H. Yao, Y. Cui, W. Hao, J. Zhu, W. Xu, D. Zhu, *ACS Appl. Mater. Interfaces* **2017**, *9*, 40752.
- [112] J. R. Winkler, H. B. Gray, *J. Am. Chem. Soc.* **2014**, *136*, 2930.
- [113] M. Ko, L. Mendecki, K. A. Mirica, *Chem. Commun.* **2018**, *54*, 7873.
- [114] I. Stassen, N. Burtch, A. Talin, P. Falcaro, M. Allendorf, R. Ameloot, *Chem. Soc. Rev.* **2017**, *46*, 3185.
- [115] J. Liu, X. Song, T. Zhang, S. Liu, H. Wen, L. Chen, *Angew. Chem., Int. Ed.* **2021**, *60*, 5612.
- [116] L. Sun, T. Miyakai, S. Seki, M. Dinca, *J. Am. Chem. Soc.* **2013**, *135*, 8185.
- [117] G. Zhang, L. Jin, R. Zhang, Y. Bai, R. Zhu, H. Pang, *Coord. Chem. Rev.* **2021**, *439*, 213915.
- [118] S. S. Park, E. R. Hontz, L. Sun, C. H. Hendon, A. Walsh, T. Van Voorhis, M. Dinca, *J. Am. Chem. Soc.* **2015**, *137*, 1774.
- [119] H. Zhong, M. Wang, G. Chen, R. Dong, X. Feng, *ACS Nano* **2022**, *16*, 1759.
- [120] G. Xu, C. Zhu, G. Gao, *Small* **2022**, *18*, 2203140.
- [121] H. Meng, Y. Han, C. Zhou, Q. Jiang, X. Shi, C. Zhan, R. Zhang, *Small Methods* **2020**, *4*, 2000396.
- [122] H. Yoon, S. Lee, S. Oh, H. Park, S. Choi, M. Oh, *Small* **2019**, *15*, 1805232.
- [123] Y. Liu, Y. Wei, M. Liu, Y. Bai, X. Wang, S. Shang, J. Chen, Y. Liu, *Angew. Chem., Int. Ed.* **2021**, *60*, 2887.
- [124] A. Mahmood, W. Guo, H. Tabassum, R. Zou, *Adv. Energy Mater.* **2016**, *6*, 1600423.
- [125] C. A. Downes, A. J. Clough, K. Chen, J. W. Yoo, S. C. Marinescu, *ACS Appl. Mater. Interfaces* **2018**, *10*, 1719.
- [126] R. Dong, Z. Zheng, D. C. Tranca, J. Zhang, N. Chandrasekhar, S. Liu, X. Zhuang, G. Seifert, X. Feng, *Chemistry* **2017**, *23*, 2255.
- [127] X. Sun, K. H. Wu, R. Sakamoto, T. Kusamoto, H. Maeda, X. Ni, W. Jiang, F. Liu, S. Sasaki, H. Masunaga, H. Nishihara, *Chem. Sci.* **2017**, *8*, 8078.
- [128] H. Jia, Y. Yao, J. Zhao, Y. Gao, Z. Luo, P. Du, *J. Mater. Chem. A* **2018**, *6*, 1188.
- [129] M. Zhang, B. H. Zheng, J. Xu, N. Pan, J. Yu, M. Chen, H. Cao, *Chem. Commun.* **2018**, *54*, 13579.
- [130] C. Guo, Y. Jiao, Y. Zheng, J. Luo, K. Davey, S.-Z. Qiao, *Chem* **2019**, *5*, 2429.
- [131] W. Zhao, J. Peng, W. Wang, S. Liu, Q. Zhao, W. Huang, *Coord. Chem. Rev.* **2018**, *377*, 44.
- [132] M. K. Lee, M. Shokouhimehr, S. Y. Kim, H. W. Jang, *Adv. Energy Mater.* **2022**, *12*, 2003990.
- [133] Y.-z. Li, Z.-h. Fu, G. Xu, *Coord. Chem. Rev.* **2019**, *388*, 79.
- [134] A. Pustovarenko, M. G. Goesten, S. Sachdeva, M. Shan, Z. Amghouz, Y. Belmabkhout, A. Dikhtiarenko, T. Rodenas, D. Keskin, I. K. Voets, B. M. Weckhuysen, M. Eddaoudi, L. de Smet, E. J. R. Sudholter, F. Kapteijn, B. Seoane, J. Gascon, *Adv. Mater.* **2018**, *30*, 1707234.
- [135] Y. Shen, B. Shan, H. Cai, Y. Qin, A. Agarwal, D. B. Trivedi, B. Chen, L. Liu, H. Zhuang, B. Mu, S. Tongay, *Adv. Mater.* **2018**, *30*, 1802497.
- [136] M. Zhao, Y. Huang, Y. Peng, Z. Huang, Q. Ma, H. Zhang, *Chem. Soc. Rev.* **2018**, *47*, 6267.
- [137] K. Zhao, S. Liu, G. Ye, Q. Gan, Z. Zhou, Z. He, *J. Mater. Chem. A* **2018**, *6*, 2166.
- [138] X. He, F. Yin, H. Wang, B. Chen, G. Li, *Chin. J. Catal.* **2018**, *39*, 207.
- [139] S. M. J. Rogge, A. Bavykina, J. Hajek, H. Garcia, A. I. Olivoso-Suarez, A. Sepulveda-Escribano, A. Vimont, G. Clet, P. Bazin, F. Kapteijn, M. Daturi, E. V. Ramos-Fernandez, I. X. F. X. Llambres, V. Van Speybroeck, J. Gascon, *Chem. Soc. Rev.* **2017**, *46*, 3134.
- [140] Y. Xu, B. Li, S. Zheng, P. Wu, J. Zhan, H. Xue, Q. Xu, H. Pang, *J. Mater. Chem. A* **2018**, *6*, 22070.
- [141] K. Jayaramulu, J. Masa, D. M. Morales, O. Tomanec, V. Ranc, M. Petr, P. Wilde, Y. T. Chen, R. Zboril, W. Schuhmann, R. A. Fischer, *Adv. Sci.* **2018**, *5*, 1801029.
- [142] G. Cai, P. Yan, L. Zhang, H. C. Zhou, H. L. Jiang, *Chem. Rev.* **2021**, *121*, 12278.
- [143] C. F. Li, L. J. Xie, J. W. Zhao, L. F. Gu, H. B. Tang, L. Zheng, G. R. Li, *Angew. Chem., Int. Ed.* **2022**, *61*, 202116934.
- [144] G. Hai, X. Jia, K. Zhang, X. Liu, Z. Wu, G. Wang, *Nano Energy* **2018**, *44*, 345.
- [145] F. L. Li, P. Wang, X. Huang, D. J. Young, H. F. Wang, P. Braunstein, J. P. Lang, *Angew. Chem., Int. Ed.* **2019**, *58*, 7051.
- [146] W. Zhou, D. D. Huang, Y. P. Wu, J. Zhao, T. Wu, J. Zhang, D. S. Li, C. Sun, P. Feng, X. Bu, *Angew. Chem., Int. Ed.* **2019**, *58*, 4227.
- [147] T. A. A. Batchelor, J. K. Pedersen, S. H. Winther, I. E. Castelli, K. W. Jacobsen, J. Rossmeisl, *Joule* **2019**, *3*, 834.
- [148] T. Wang, H. Chen, Z. Yang, J. Liang, S. Dai, *J. Am. Chem. Soc.* **2020**, *142*, 4550.
- [149] X. Zhao, Z. Xue, W. Chen, X. Bai, R. Shi, T. Mu, *J. Mater. Chem. A* **2019**, *7*, 26238.
- [150] Z. Li, X. Zhang, H. Cheng, J. Liu, M. Shao, M. Wei, D. G. Evans, H. Zhang, X. Duan, *Adv. Energy Mater.* **2019**, *10*, 1900486.
- [151] M. Cai, Q. Liu, Z. Xue, Y. Li, Y. Fan, A. Huang, M.-R. Li, M. Croft, T. A. Tyson, Z. Ke, G. Li, *J. Mater. Chem. A* **2020**, *8*, 190.
- [152] Y. Ding, Y. P. Chen, X. Zhang, L. Chen, Z. Dong, H. L. Jiang, H. Xu, H. C. Zhou, *J. Am. Chem. Soc.* **2017**, *139*, 9136.
- [153] Y. S. Wei, M. Zhang, R. Zou, Q. Xu, *Chem. Rev.* **2020**, *120*, 12089.
- [154] J. Huang, Y. Li, R. K. Huang, C. T. He, L. Gong, Q. Hu, L. Wang, Y. T. Xu, X. Y. Tian, S. Y. Liu, Z. M. Ye, F. Wang, D. D. Zhou, W. X. Zhang, J. P. Zhang, *Angew. Chem., Int. Ed.* **2018**, *57*, 4632.
- [155] W. Pang, B. Shao, X. Q. Tan, C. Tang, Z. Zhang, J. Huang, *Nanoscale* **2020**, *12*, 3623.
- [156] Q. Ji, Y. Kong, C. Wang, H. Tan, H. Duan, W. Hu, G. Li, Y. Lu, N. Li, Y. Wang, J. Tian, Z. Qi, Z. Sun, F. Hu, W. Yan, *ACS Catal.* **2020**, *10*, 5691.
- [157] X. Mu, H. Yuan, H. Jing, F. Xia, J. Wu, X. Gu, C. Chen, J. Bao, S. Liu, S. Mu, *Appl. Catal. B* **2021**, *296*, 120095.
- [158] Y. Xue, S. Zheng, H. Xue, H. Pang, *J. Mater. Chem. A* **2019**, *7*, 7301.
- [159] Y. Liu, Z. Tang, *Adv. Mater.* **2013**, *25*, 5819.
- [160] Q. Jiang, C. Zhou, H. Meng, Y. Han, X. Shi, C. Zhan, R. Zhang, *J. Mater. Chem. A* **2020**, *8*, 15271.
- [161] N. Yang, H. Cheng, X. Liu, Q. Yun, Y. Chen, B. Li, B. Chen, Z. Zhang, X. Chen, Q. Lu, J. Huang, Y. Huang, Y. Zong, Y. Yang, L. Gu, H. Zhang, *Adv. Mater.* **2018**, *30*, 1803234.
- [162] Z. Liu, J. Qi, M. Liu, S. Zhang, Q. Fan, H. Liu, K. Liu, H. Zheng, Y. Yin, C. Gao, *Angew. Chem., Int. Ed.* **2018**, *57*, 11678.
- [163] X. Liu, J. Iocozzia, Y. Wang, X. Cui, Y. Chen, S. Zhao, Z. Li, Z. Lin, *Energy Environ. Sci.* **2017**, *10*, 402.
- [164] R. Subbaraman, D. Tripkovic, D. Strmcnik, K.-C. Chang, M. Uchamura, A. P. Paulikas, V. Stamenkovic, N. M. Markovic, *Science* **2011**, *334*, 1256.
- [165] Y. Zheng, Y. Jiao, A. Vasileff, S. Z. Qiao, *Angew. Chem., Int. Ed.* **2018**, *57*, 7568.

- [166] K. Rui, G. Zhao, M. Lao, P. Cui, X. Zheng, X. Zheng, J. Zhu, W. Huang, S. X. Dou, W. Sun, *Nano Lett.* **2019**, *19*, 8447.
- [167] H. Yu, Y. Jing, C.-F. Du, J. Wang, *J. Energy Chem.* **2022**, *65*, 71.
- [168] W. Zhang, Y. Wang, H. Zheng, R. Li, Y. Tang, B. Li, C. Zhu, L. You, M. R. Gao, Z. Liu, S. H. Yu, K. Zhou, *ACS Nano* **2020**, *14*, 1971.
- [169] W. Huang, C. Peng, J. Tang, F. Diao, M. Nulati Yesibolati, H. Sun, C. Engelbrekt, J. Zhang, X. Xiao, K. S. Mølhave, *J Energy Chem* **2022**, *65*, 78.
- [170] J. Cui, J. Liu, C. Wang, F. Rong, L. He, Y. Song, Z. Zhang, S. Fang, *Electrochim. Acta* **2020**, *334*, 135577.
- [171] K. Srinivas, Y. Lu, Y. Chen, W. Zhang, D. Yang, *ACS Sustainable Chem. Eng.* **2020**, *8*, 3820.
- [172] W. Cheng, X. F. Lu, D. Luan, X. W. D. Lou, *Angew. Chem., Int. Ed.* **2020**, *59*, 18234.
- [173] Q. Liang, J. Chen, F. Wang, Y. Li, *Coord. Chem. Rev.* **2020**, *424*, 213488.
- [174] Z. Tian, C. Wei, J. Sun, *Nanoscale Adv.* **2020**, *2*, 2220.
- [175] P. Thangavel, M. Ha, S. Kumaraguru, A. Meena, A. N. Singh, A. M. Harzandi, K. S. Kim, *Energy Environ. Sci.* **2020**, *13*, 3447.
- [176] A. Hu, Q. Pang, C. Tang, J. Bao, H. Liu, K. Ba, S. Xie, J. Chen, J. Chen, Y. Yue, Y. Tang, Q. Li, Z. Sun, *J. Am. Chem. Soc.* **2019**, *141*, 11322.
- [177] J. Pang, R. G. Mendes, A. Bachmatiuk, L. Zhao, H. Q. Ta, T. Gemming, H. Liu, Z. Liu, M. H. Rummeli, *Chem. Soc. Rev.* **2019**, *48*, 72.
- [178] M. Khazaei, M. Arai, T. Sasaki, A. Ranjbar, Y. Liang, S. Yunoki, *Phys. Rev. B* **2015**, *92*, 075411.
- [179] L. Zhao, B. Dong, S. Li, L. Zhou, L. Lai, Z. Wang, S. Zhao, M. Han, K. Gao, M. Lu, X. Xie, B. Chen, Z. Liu, X. Wang, H. Zhang, H. Li, J. Liu, H. Zhang, X. Huang, W. Huang, *ACS Nano* **2017**, *11*, 5800.
- [180] R. Zhu, J. Ding, Y. Xu, J. Yang, Q. Xu, H. Pang, *Small* **2018**, *14*, 1803576.
- [181] J. Wang, H. C. Zeng, *ACS Appl. Mater. Interfaces* **2019**, *11*, 23180.
- [182] J. Zhang, T. Wang, P. Liu, S. Liu, R. Dong, X. Zhuang, M. Chen, X. Feng, *Energy Environ. Sci.* **2016**, *9*, 2789.
- [183] Z. Zhu, H. Yin, C. T. He, M. Al-Mamun, P. Liu, L. Jiang, Y. Zhao, Y. Wang, H. G. Yang, Z. Tang, D. Wang, X. M. Chen, H. Zhao, *Adv. Mater.* **2018**, *30*, 1801171.
- [184] D. Zhu, J. Liu, Y. Zhao, Y. Zheng, S. Z. Qiao, *Small* **2019**, *15*, 1805511.
- [185] L. Chen, H. Zhang, L. Chen, X. Wei, J. Shi, M. He, *J. Mater. Chem. A* **2017**, *5*, 22568.
- [186] D. Zhu, J. Liu, L. Wang, Y. Du, Y. Zheng, K. Davey, S. Z. Qiao, *Nanoscale* **2019**, *11*, 3599.
- [187] Z. Gao, Z. W. Yu, F. Q. Liu, C. Yang, Y. H. Yuan, Y. Yu, F. Luo, *ChemSusChem* **2019**, *12*, 4623.
- [188] C. Wu, H. Li, Z. Xia, X. Zhang, R. Deng, S. Wang, G. Sun, *ACS Catal.* **2020**, *10*, 11127.
- [189] Y. Lin, H. Wang, C. K. Peng, L. Bu, C. L. Chiang, K. Tian, Y. Zhao, J. Zhao, Y. G. Lin, J. M. Lee, L. Gao, *Small* **2020**, *16*, 2002426.
- [190] Y. Wang, L. Yan, K. Dastafkan, C. Zhao, X. Zhao, Y. Xue, J. Huo, S. Li, Q. Zhai, *Adv. Mater.* **2021**, *33*, 2006351.
- [191] F. Zheng, W. Zhang, X. Zhang, Y. Zhang, W. Chen, *Adv. Funct. Mater.* **2021**, *31*, 2103318.
- [192] W. Chen, C. Wang, S. Su, H. Wang, D. Cai, *Chem. Eng. J.* **2021**, *414*, 128784.
- [193] C. F. Li, J. W. Zhao, L. J. Xie, J. Q. Wu, Q. Ren, Y. Wang, G. R. Li, *Angew. Chem., Int. Ed.* **2021**, *60*, 18129.
- [194] J. W. Yoon, J. H. Kim, C. Kim, H. W. Jang, J. H. Lee, *Adv. Energy Mater.* **2021**, *11*, 2003052.
- [195] B. Cui, G. Fu, *Nanoscale* **2022**, *14*, 1679.
- [196] H. Sun, Z. Yan, F. Liu, W. Xu, F. Cheng, J. Chen, *Adv. Mater.* **2020**, *32*, 1806326.
- [197] J. Du, F. Li, L. Sun, *Chem. Soc. Rev.* **2021**, *50*, 2663.
- [198] J. Zhang, Q. Zhang, X. Feng, *Adv. Mater.* **2019**, *31*, 1808167.
- [199] J. Hou, Y. Wu, B. Zhang, S. Cao, Z. Li, L. Sun, *Adv. Funct. Mater.* **2019**, *29*, 1808367.
- [200] F. Li, M. Du, X. Xiao, Q. Xu, *ACS Nano* **2022**, <https://doi.org/10.1021/acsnano.2c09396>.
- [201] W. Li, S. Watzel, H. A. El-Sayed, Y. Liang, G. Kieslich, A. S. Bandarenka, K. Rodewald, B. Rieger, R. A. Fischer, *J. Am. Chem. Soc.* **2019**, *141*, 5926.
- [202] X. F. Lu, L. F. Gu, J. W. Wang, J. X. Wu, P. Q. Liao, G. R. Li, *Adv. Mater.* **2017**, *29*, 1604437.
- [203] L. Han, P. Tang, A. Reyes-Carmona, B. Rodriguez-Garcia, M. Torrens, J. R. Morante, J. Arbiol, J. R. Galan-Mascaros, *J. Am. Chem. Soc.* **2016**, *138*, 16037.
- [204] D. Yang, Y. Chen, Z. Su, X. Zhang, W. Zhang, K. Srinivas, *Coord. Chem. Rev.* **2021**, *428*, 213619.
- [205] S. Li, B. Chen, Y. Wang, M. Y. Ye, P. A. van Aken, C. Cheng, A. Thomas, *Nat. Mater.* **2021**, *20*, 1240.
- [206] W. Cheng, X. Zhao, H. Su, F. Tang, W. Che, H. Zhang, Q. Liu, *Nat. Energy* **2019**, *4*, 115.
- [207] M. Xie, Y. Ma, D. Lin, C. Xu, F. Xie, W. Zeng, *Nanoscale* **2020**, *12*, 67.
- [208] F. Sun, G. Wang, Y. Ding, C. Wang, B. Yuan, Y. Lin, *Adv. Energy Mater.* **2018**, *8*, 1800584.
- [209] D. Senthil Raja, C.-L. Huang, Y.-A. Chen, Y. Choi, S.-Y. Lu, *Appl. Catal., B* **2020**, *279*, 119375.
- [210] D.-J. Li, Q.-H. Li, Z.-G. Gu, J. Zhang, *J. Mater. Chem. A* **2019**, *7*, 18519.
- [211] X. Liu, J. Meng, J. Zhu, M. Huang, B. Wen, R. Guo, L. Mai, *Adv. Mater.* **2021**, *33*, 2007344.
- [212] L. Huang, G. Gao, H. Zhang, J. Chen, Y. Fang, S. Dong, *Nano Energy* **2020**, *68*, 104296.
- [213] B. Wang, J. Shang, C. Guo, J. Zhang, F. Zhu, A. Han, J. Liu, *Small* **2019**, *15*, 1804761.
- [214] L. Yang, G. Zhu, H. Wen, X. Guan, X. Sun, H. Feng, W. Tian, D. Zheng, X. Cheng, Y. Yao, *J. Mater. Chem. A* **2019**, *7*, 8771.
- [215] C. Cao, D. D. Ma, Q. Xu, X. T. Wu, Q. L. Zhu, *Adv. Funct. Mater.* **2018**, *29*, 1807418.
- [216] J. Du, S. Xu, L. Sun, F. Li, *Chem. Commun.* **2019**, *55*, 14773.
- [217] G. Dong, L. Yu-ting, D. Chun-ying, M. Hong, M. Qing-jin, *Inorg. Chem.* **2003**, *42*, 2519.
- [218] Z. Xue, K. Liu, Q. Liu, Y. Li, M. Li, C. Y. Su, N. Ogiwara, H. Kobayashi, H. Kitagawa, M. Liu, G. Li, *Nat. Commun.* **2019**, *10*, 5048.
- [219] W. Li, F. Li, H. Yang, X. Wu, P. Zhang, Y. Shan, L. Sun, *Nat. Commun.* **2019**, *10*, 5074.
- [220] F. Cheng, Z. Li, L. Wang, B. Yang, J. Lu, L. Lei, T. Ma, Y. Hou, *Mater. Horiz.* **2021**, *8*, 556.
- [221] C. Yang, A. Grimaud, *Catalysts* **2017**, *7*, 149.
- [222] D. Senthil Raja, H.-W. Lin, S.-Y. Lu, *Nano Energy* **2019**, *57*, 1.
- [223] W. Ye, Y. Yang, X. Fang, M. Arif, X. Chen, D. Yan, *ACS Sustainable Chem. Eng.* **2019**, *7*, 18085.
- [224] J. Zhou, Y. Dou, X. Q. Wu, A. Zhou, L. Shu, J. R. Li, *Small* **2020**, *16*, 1906564.



Chao-Peng Wang is a postdoctoral fellow in the School of Materials Science and Engineering in Nankai University. He received his bachelor's degree from Henan Polytechnic University in 2015, and he was then supervised by Prof. X.-H. Bu and Prof. J. Zhu, and obtained his Ph.D. from Nankai University in 2021. His research interests include the preparation of MOF-based nanomaterials and their applications in electrochemical energy storage and conversion.



Jian Zhu is a professor in the School of Materials Science and Engineering in Nankai University. He earned his Ph.D. in chemical engineering from University of Michigan, Ann Arbor, in 2013, and then started his postdoctoral research in the Department of Materials Science and Engineering at Northwestern University. He has been a faculty member of Nankai University since 2017. His research interest includes nanoelectronic materials, nanoadditive manufacturing, and nanocomposites.



Xian-He Bu is an Academician of the Chinese Academy of Sciences. He is a professor at Nankai University and serves as the chair of the School of Materials Science and Engineering. His research interests include functional coordination chemistry, crystal engineering, molecular magnetism, and material chemistry.